

© 2016 Yue Wang

SOFT TISSUE VISCOELASTIC PROPERTIES: MEASUREMENTS, MODELS AND  
INTERPRETATION

BY

YUE WANG

DISSERTATION

Summited in partial fulfillment of the requirements  
for the degree of Doctor of Philosophy in Bioengineering  
in the Graduate College of the  
University of Illinois at Urbana- Champaign, 2016

Urbana, Illinois

Doctoral Committee:

Professor Michael F. Insana, Chair  
Professor Stephen A. Boppart  
Associate Professor Brad P. Sutton  
Associate Professor Amy Wagoner Johnson

## ABSTRACT

The quantification of mechanical properties of soft tissues has been of great interest for more than two decades because they have the potential of being used as biomarkers for disease diagnosis. Indentation techniques, the most recognized techniques for characterizing mechanical properties, are widely used for basic science investigations in research labs. The use of elastography techniques coupled with imaging technologies has been growing rapidly in recent years, which is promising for clinical applications. Each technique produces different mechanical behaviors due to the interaction of the stimuli and the structure of the tissue. An appropriate model will parameterize these behaviors to reflect the corresponding tissue microscopic features with high fidelity. The objective of this thesis is to identify combinations of techniques and models that will yield mechanical parameters with diagnostic interpretations about tissue microenvironment.

Three techniques for characterizing tissue viscoelastic properties were developed and validated; each offers strengths in a large variety of applications. Indentation based techniques measure low-frequency force-displacement curves under different loading profiles. Ultrasound-based techniques and optical based techniques measure the dispersion behaviors of the propagating wave velocities at mid-to-high frequency ranges. When a material is linear, isotropic, and contains only elastic components, the “intrinsic” elastic modulus of the material can be obtained independently of the technique used when corrections are properly made to eliminate the bias from boundary effects. If the material includes time-dependent components, models must be included in the analysis to provide parametric estimates. Classical models for viscoelastic solids such as the Kelvin-Voigt model do not fully represent mechanical measurements in tissues because they are not material continua. Tissue properties are determined in part by fluid movement in the open- and

closed-cell compartments found within a viscoelastic collagen matrix that is actively maintained by the embedded cells to meet programmed needs. These biphasic (solid/fluid) media exhibit multifaceted deformation responses that are particularly difficult to model using a concise feature set.

The Kelvin-Voigt fractional derivative (KVFD) model introduced in this study represents the measurement data of a broad range in both time and frequency domain with a small number of parameters, and it yields stable estimates for many types of phantoms and tissues. It is superior to the integer derivative models for the materials and techniques we used in this study. Moreover, the KVFD model provides a three-dimensional feature space of mechanical properties that properly characterizes the composition and structure of a material. This was validated through measurements on gelatin-cream emulsion samples exhibiting viscoelastic behavior, as well as ex vivo liver tissue samples. For the elastic property, KVFD parameter  $E_0$  mainly represents the elasticity of the solid matrix and is approximately equal to the shear modulus no matter which technique is used. For the viscous property, when combined with different measurement techniques, KVFD model parameter  $\alpha$  and  $\tau$  represent different tissue components. The combination of these techniques and the KVFD model have the potential to be able to distinguish between healthy and pathological tissues described by the histological features.

## ACKNOWLEDGMENTS

First, I want to thank my advisor Professor Michael Insana, without whom I could not go this far. He had a profound impact on my life, to help me grow both as a researcher and as a person. He is the dream advisor one can imagine. He is intelligent, patient, good-tempered and full of positive energy. Discussing research results and papers is a pleasure for me because he not only sees the big picture and sends me to explore unknown areas that appear promising, but also understands every detail of the experiments and provides useful ideas in how to do experiments. He is always trying to help me as much as he can whenever I need his help. And he never blames me for silly mistakes. For me, he is more like a father than an advisor. During my hardest time, he gave me great encouragement and trust which cheered me up. During the time I have been working at a company, he would come at night to meet with me regularly. I deeply appreciate his mentorship from the bottom of my heart. I would also like to thank Professor Boppart for being my co-advisor in M-CNTC fellowship and support my activities in his lab. Additionally, I would like to thank the rest of my committee members Dr. Sutton, and Dr. Wagoner Johnson for their valuable inputs and recommendations. I worked with many people throughout the years. They are all very friendly and enjoyable to work and talk with, from whom I learned a lot. Great thanks to Dr. Marko Orescanin, Dr. Steven Adie, Dr. Hongmei Zhang, Dr. Nathan Shemonski, Dr. Khaldoon Altahhan, Dr. Adeel Ahmad, Jenny Huang, Dan Weisgerber for all their help and professional insights. Finally, I would like to thank my parents for their love and incredible support during my most difficult time period. Throughout my life, they have actively supported me in doing things I love to do and realize my dream, encouraged me to be a happy person and to contribute to others. This work would not have been possible without the funding from the National Cancer Institute (NIH ROI CA168575), and the Midwestern Cancer Nanotechnology Training Center (NIH-NCI R25 CA154015).

## **DEDICATION**

*This work is dedicated to my beloved parents*

# TABLE OF CONTENTS

CHAPTER 1: INTRODUCTION .....	1
1.1 Biological background and clinical significance .....	1
1.2 Review of techniques in characterizing tissue mechanical property.....	2
1.3 Quantifying tissue viscoelastic property using rheological models .....	6
1.4 Impact and objectives.....	10
CHAPTER 2: INDENTATION AND SHEAR WAVE IMAGING TECHNOLOGIES FOR QUANTIFYING MECHANICAL PROPERTIES .....	17
2.1 Indentation methods.....	17
2.1.1 Load-unload test.....	18
2.1.2 Ramp-relaxation test .....	22
2.2 Shear wave based methods .....	24
2.2.1 Complex shear modulus estimation from wave propagation - Theory .....	24
2.2.2 Wave generation and propagation.....	27
2.2.3 Rheological models.....	32
2.3 Ultrasonic shear-wave imaging using vibrating-needle stimulation .....	35
2.3.1 Validation measurement in homogeneous gelatin phantom .....	36
2.3.2 Validation measurement in inhomogeneous gelatin phantom .....	38
2.3.3 Shear modulus quantification of rodent mammary tumors.....	42
2.4 Acoustic radiation force optical coherence elastography (ARF-OCE).....	50
2.4.1 US-OCT methodology .....	53
2.4.2 Validation results of phantom and tissue .....	57
2.5 Summary.....	60
CHAPTER 3: CORRELATION OF TECHNIQUES, MODELS AND ESTIMATED MECHANICAL PROPERTY .....	62
3.1 The consistency of all techniques on elastic material .....	62
3.1.1 Measurement of gelatin samples.....	63
3.1.2 Boundary-effect simulations and solutions.....	72

3.2	The effect of rheological models on measurements.....	89
3.3	Summary.....	94
CHAPTER 4: KVFD MODELLING FOR VISCOELASTIC MATERIALS .....		97
4.1	Background.....	97
4.2	Material and method .....	98
4.2.1	Gelatin-Cream viscoelastic phantom .....	99
4.2.2	Theory of KVFD model.....	100
4.2.3	Ramp-hold relaxation solution for spherical and plate indenter .....	102
4.3	Results.....	106
4.3.1	Impact of relaxation time on the variability of estimated model parameters.....	106
4.3.2	Impact of ramp time $T_r$ on model parameter estimates .....	112
4.3.3	Quantifying samples with varying properties .....	115
4.4	Discussion and conclusion.....	118
CHAPTER 5: ASSESSING COMPOSITIONAL AND STRUCTURAL INFORMATION OF TISSUE USING KVFD MODEL.....		121
5.1	Material and method .....	122
5.2	Interpretation of KVFD model parameters in biphaic phantom .....	127
5.2.1	Low frequency indentation measurements.....	127
5.2.2	High frequency wave imaging measurements .....	137
5.3	KVFD model parameters change during liver hyperthermia and ablation .....	142
5.4	Summary.....	147
CHAPTER 6: CONCLUSIONS AND FUTURE WORK.....		150
6.1	Summary and Conclusions.....	150
6.2	Future work.....	154
REFERENCES .....		157

# CHAPTER 1: INTRODUCTION

## 1.1 Biological background and clinical significance

Palpation is one of the most common examinations used by physicians in diagnosing diseases such as liver fibrosis and various types of cancer. These mechanical property changes that physicians “feel” could facilitate their diagnosis and prognosis. In recent years, more and more studies have shown clear evidence that pathological changes in tissues are often accompanied by changes in the tissue extracellular matrix (ECM), which alter the mechanical properties of tissue [1,2,3]. For example, liver stiffness was found to predict the 5-year survival rate of patients chronically infected with hepatitis B virus [4]. Arterial stiffness was found to be positively correlated with several inflammatory markers in essential hypertension [7]. Invasive breast cancers are much stiffer compared to normal and benign tissues. Fibrocystic disease and low-grade malignant mammary tumors exhibit 3-6-fold stiffness increases, compared to the baseline elastic modulus values for normal fibro-glandular breast tissues. High-grade invasive ductal carcinomas can be 13 times stiffer on average [5, 6]. Recent studies have also confirmed the correlation of diseases and mechanical properties at cellular and molecular level, pointing out that many diseases are associated with modified expression profiles of ECM-related genes. For example, cancer is associated with a range of tissue ECM changes affecting the cellular mechano-environment that results in a disease-promoting reactive stroma. The density of the ECM collagen and the crosslinks of the collagen increase, as fluid pressure builds from lymphatic collapse in part from epithelial hyperplasia [8]. Different subclasses of tumors can have different ECM constituents in tumor micro-environment, and therefore exhibit different mechanical characteristics [9]. Since they show significant differences in tumor development, progression, and responses to therapy, imaging tumor mechanical properties can provide a sensitive indication of early pathological processes that

will improve patient diagnosis and prognosis, as well as assist with treatment plans and the evaluations of therapeutic responses. Also, accurately characterizing and interpreting the viscoelastic properties of tissue will have a profound influence on basic research of mechanobiology, an emerging field of science that focuses on understanding the role of mechanobiology in disease onset, progression, and responses to treatment [10].

## **1.2 Review of techniques in characterizing tissue mechanical property**

There are several techniques that facilitate assessing tissue mechanical properties. Indentation is a primary modality for characterizing the mechanical properties of a large variety of materials. It is often regarded as the “gold standard” for calibrating material mechanical properties, including elasticity and viscosity. Depending on the dimension and scale of loading, there are macro-indentation (can have test loads up to 1 kN), micro-indentation (allows forces of 2 N and produces displacement of about 50  $\mu\text{m}$ ) [12], and nano-indentation (typically used for very small samples or very stiff tissues) [11,13]. Three testing modes are most widely used for viscoelastic materials: force-displacement behavior during single or multiple load-unload cycle(s), creep behavior during the probes push and hold at peak load, and relaxation behavior during the probes push and hold at peak strain. The drawback of indentation techniques lies in that they are usually not fully compatible with in vivo measurements, and the contact between sample surfaces and indentation probe must be under strict controls for most indentation probes.

A new class of imaging technologies called elastography is growing very fast in the past fifteen years which enables the measurements of tissue mechanical properties in vivo. It allows the physicians to evaluate changes during disease progression and disease treatment using the standard

imaging technologies. Elastography was proved both in research labs and in clinic applications to have the potential of accurately mapping the elastic modulus and potentially viscoelastic properties. It usually applies a mechanical loading, either by compressions or oscillatory forces, and then track the motions or deformation responses of the tissue using imaging modalities such as MRI, Ultrasound and Optical Coherence Tomography (OCT). By modeling this tissue motion, a map of the mechanical property can be provided.

Depending on the way that the excitation force is applied and the inversion technique that is used to derive the mechanical parameters, elastography has three main categories. The first class is based on the static strain. The quasi-static strain responses are recorded before and after the force application, and a strain/stiffness contrast image will be displayed [14]. The second class is to apply a dynamic force and analyze the frequency responses or amplitude responses at the location where the perturbation is applied [15,16]. The third class is based on the propagating waves generated by an excitation source [17-20]. This category provides the most quantitative measurements among all three categories because the theory of mechanical waves can be applied.

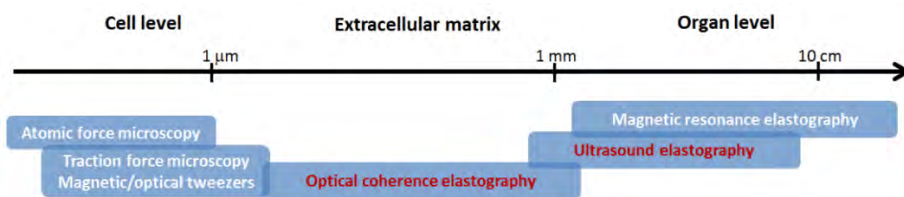


**Figure 1.1.** Elastographic modalities characterized by their range of spatial coverage.

The major technologies for imaging tissue deformations in response to mechanical forces are listed in Figure 1.1. They are different in spatial resolution, displacement sensitivity, and field-of-view capability. For different application scopes, different imaging modalities are used. MRE has the advantage of being able to image much larger volumes, and to assess the full three-

dimensional displacement vector, allowing a more precise analysis of viscoelastic parameters [21]. Ultrasound elastography is an inexpensive and widely assessable technology so far. Various excitation and inversion methods were developed, and some have been commercialized. OCE is newly recognized as a promising complementary modality. It is most sensitive to nanometer-scaled displacements with a spatial resolution as low as 1  $\mu\text{m}$  [22], therefore can measure the mechanical perturbations at high frequencies. It has the potential to interrogate tissue at micro-scale (ECM scale), which largely broadens the application scope for elastography to include those small heterogeneous samples.

In the following, several common elastographic methods involving ultrasonic and optical modalities will be listed. Each method has distinguishing features that influence the diagnostic information provided: the source, spatial extent, and frequency content of tissue force excitation; the dimensionality of the motion tracking; and the type of data reconstruction that yields strain or modulus images. Despite differences, the goal of all elasticity imaging techniques is to describe some vital aspects of the cellular mechano-environment that enhance the clinical diagnosis or improve our understanding of the role mechanobiology plays in disease progression and treatment. Methods are classified based on whether they measure the instantaneous deformations or time-dependent deformations.

- **Quasi-static imaging methods**: When the position of tissue anatomy is recorded immediately before and after a slowly applied force, one can map the instantaneous stiffness using strain images. Strain images are computed from local gradients of tissue displacements [23]. If the force is broadly applied to the tissue, as in compression elastography where a roughly uniform stress is assumed, then the estimated strain can approximate stiffness of the material [24,25,26]. Additionally, if the force is applied for a

longer time to record a creep or time relaxation behavior, time-dependent properties such as viscosity can be estimated as well [27]. This would be an enhanced version of indentation using imaging techniques, with the strain measured at every pixel in the image. Because small forces ( $<10$  N) are applied slowly ( $>1$  s), there is enough time for the deformation to propagate throughout the tissue, and therefore the strain at each point in the image is influenced to some degree by the properties mechanically coupled throughout the tissue, which influences the spatial resolution in unpredictable ways. Alternatively, an acoustic radiation force can be applied locally and quickly so that the localized deformation describes local tissue stiffness [28]. In either case, stiffness contrast described by a strain image is capable of differentiating benign from malignant tumors in the breast [29,30], prostate [31] and thyroid [32, 33], and can be used for guiding interventional procedures near nerve bundles [28].

- **Dynamic imaging methods**: When the force applied to tissues is varied harmonically as deformations are sequentially recorded, one can form images of the viscoelastic (time-dependent) tissue properties either from oscillatory amplitudes and frequencies [34, 35] or from the propagation patterns of perturbations inside the tissue which is known as shear wave imaging. One advantage of dynamic elasticity imaging over other approaches is the ability to provide information necessary to quantitatively estimate the complex modulus. From the time-series of reflected acoustical or optical waves, complex modulus is often estimated [36], where the real part represents the elastic modulus that can be closely related to tissue stiffness, as described above. The complex modulus also describes tissue viscosity, which is related to the rate of the deformation. Viscoelastic properties measured over a

broad range of the applied forces reveal detailed information about the role of mechanobiology in disease progression [37, 38, 39]. They also convey important diagnostic information about breast [30, 40, 41, 42, 43], liver [44, 45, 46], thyroid [47], and arterial [48] disease conditions.

Each technology has its own advantages and limitations in real applications. The choice of elastographic methods depends on the available experimental conditions, as well as the goal of the measurements. Moreover, different techniques might interrogate different components or phenomena of the tissue depending on the way of stimulating the mechanical behavior. Preliminary success which shows the mechanical contrast in tissues has been achieved in elastography applications as presented in the above reference papers. However, much has to be accomplished to make the mechanical images or estimated parameters more quantitative and more representative of relevant features.

### **1.3 Quantifying tissue viscoelastic property using rheological models**

Since tissues exhibit non-linear viscoelastic behaviors, most elastic models would fail to describe the behaviors of most tissue types. In order to quantify tissue viscoelastic behavior using a few number of parameters, the rheological constitutive equation is often used. The biggest challenge in seeking the right model comes from the fact that tissue is “too complex”. First, tissues can be highly heterogeneous, nonlinear and anisotropic with unpredictable behaviors under different loading profiles, which makes it difficult for one model to accurately describe the comprehensive mechanical responses. Second, the geometry of the tissue is often irregular. As

most mechanical testing methods are sensitive to boundary conditions, it is difficult to rule out the geometric effect when performing tissue testing. Last but not the least, tissue is not a material but a structure with multi-phasic components. At the microscopic level, tissues are composed of ECM proteins, polysaccharides (sugars), cells, freely flowing open body fluids in between ECM, and closed body fluids which are tightly bound to protein molecules that do not flow frequently. At the macroscopic level, they are heterogeneous solids (ECM) with closed (cells) and open (vasculature) fluid compartments. As a result of this complexity, tissues exhibit really complicated time-varying behaviors under mechanical testing, which results in tissues being modeled as viscoelastic solids or poroelastic media. Some research studies chose to ignore the time-dependent response of tissue and only focused on the elastic portion of the mechanical property. This simple elastic model behaves robustly and generates parameter that correlates well with tissue stiffness [49, 50]. However, the drawback of adopting purely elastic model is that it fails to capture the information about the time-varying property of the tissue which is crucial to the understanding of the microenvironment and contains huge potential in promoting diagnosis. Also, if the time-varying responses are significant, biases will be introduced to the estimation of the elasticity if no time-dependent parameter is in the model. For example, shear wave speed propagating in an elastic material is a constant for any driving frequency. However, in viscoelastic materials, shear wave speed is dispersive; i.e., the wave speed changes substantially with frequency. Dispersive behavior is determined by the constituents of the materials and their mechanical couplings.

Therefore, adopting a rheological model with only a few parameters is necessary to reliably capture the comprehensive properties of tissue. The model characterization is often torn between accurately representing the spatial distribution of mechanical properties of tissues, which could lead to rational diagnostic design, and identifying robust features that correlated well with disease

condition but may not represent the intrinsic property. In general, a perfect rheological model should have the following properties:

1. The assumptions of the model must not be violated by the technique used. And the model must describe the time-varying behavior very well with as few parameters as possible.
2. The model should be flexible enough to incorporate the mechanical behaviors under most if not all of the loading conditions.
3. The model parameters should have some physical meaning, either related to some known physics quantities (i.e., Young's modulus, loss of energy) or be sensitive to tissue properties that indicate the state of health.
4. The model is preferred to have modality/method independent parameters for the purposes of method validation and comparison.

One common element of all these modeling approaches is to find a good balance between model simplicity and experimental fitting accuracy. Increasing the parametric dimension generally renders better fits, but increases the difficulty of translating model parameters into a concise set of intrinsic mechanical properties. Although some mathematical models such as Prony series are sometimes considered in polymer characterizations to model stress or strain behavior [51], the mechanics community prefers classical constitutive models. In standard rheological models, stress and strain are related by springs and dash-pots, which represent tissue components and structures. Examples of models with two or three parameters (each corresponding to a spring or a dashpot) are the Maxwell model [52, 53, 54], the Kelvin–Voigt model [55, 56, 57] and standard linear solid models [58, 59, 60]. Combinations of these elementary models have also been applied to form a more complicated model to improve model fits when estimating viscoelastic parameters [61, 62,

63]. However, the performance of these models is material specific, meaning that each model is suitable for only a fraction of the tissue types or certain loading conditions due to its limitations. The Fractional Derivative (FD) concept was introduced into the models by Sloninsky to account for the complicated time-dependent behavior of biological materials. It has been reported to fit very well to the time-varying responses of the tissue despite there being a small number of fit parameters [64].

The time-varying response comes from a complex tissue composition and ECM network that tends to exhibit a coupled elastic and viscous behavior. The composition and ultrastructural arrangement of tissue as well as the interactions among tissue components will cause changes in mechanical responses, and a good rheological model should also be able to yield parameters that are descriptive of these changes, which will eventually benefit diagnosis [65]. By selecting the excitation frequencies and spatial distributions of the applied force, different components of the tissue structures are interrogated. Methods for characterizing mechanical properties can apply force frequencies as low as 0.1 Hz and as high as 10 kHz. In quasi-static imaging methods, the contrast of stiffness arises primarily from the elastic compliance of the ECM. If the time-dependent behavior is also recorded during the experiment, additional information on the fluid part of the tissue may also be acquired. For dynamic imaging methods, the effect from the slow motion of the free fluid will be weakened compared to quasi-static methods, as perfusion or fluid flow happens at a much lower frequency. In contrast, some frequency-dependent viscous components and structures such as intramolecular crosslinks will appear [65]. Traditional rheological models are usually restricted to a narrow frequency bandwidth, which makes it difficult to fairly compare the results measured under different frequency ranges. The goal is to find a model that can describe mechanical responses of a large frequency bandwidth while has the ability to extract properties of

tissue ECM (i.e. the solid matrix stiffness and viscosity, body fluid content), which can then be connected with tissue healthiness.

In summary, tissue is a multiphasic “structure” and not a classic “material” that exhibits time-varying responses under mechanical loading. A proper model will depict the multiphasic tissue properties using a few parameters, which should provide consistent parametric estimates corresponding to the intrinsic tissue features and properties. It is desired to have some consistency in the frequency-independent measurements when various quantification methods are used, and for the frequency-dependent components, it may or may not vary with measurement techniques and models. A good model will further extend the capability of using tissue mechanical property to understand tissue status, and thus reinforce diagnosis.

#### **1.4 Impact and objectives**

Although a collection of techniques including mechanical characterization and imaging techniques, and several rheological models are proposed for measuring tissue mechanical properties, it is still ambiguous on how to choose among different techniques and models that are available in order to extract disease-oriented tissue information. Figure 1.2 summarizes the relation of basic elements in the process of tissue mechanical characterization. If the mechanical parameters yielded by certain technique-model combination can be correlated with tissue compositions, then these parameters can be used to identify disease features with higher sensitivity and specificity. These additional characterizations can enhance conventional diagnoses. However, the complex nature of tissue brings difficulties to every element of this process, especially the

“interpretation” part where the measured tissue mechanical parameters are translated into the corresponding biological sources to facilitate diagnosis.

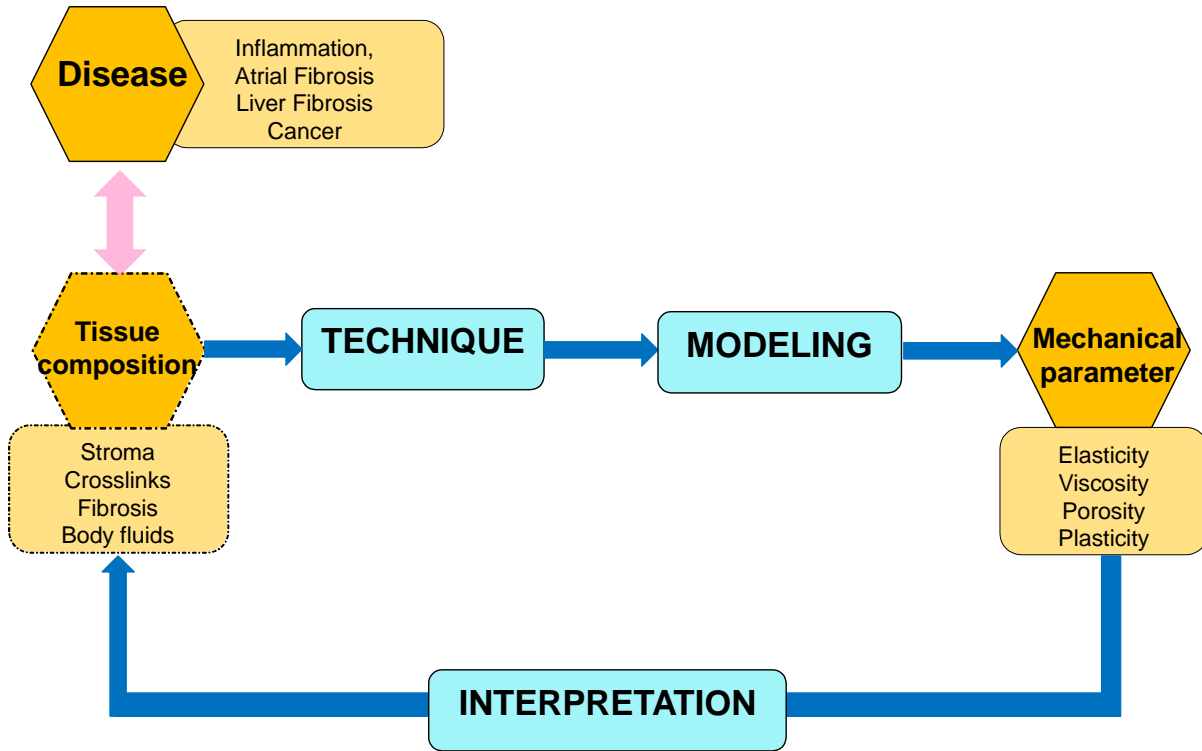


**Figure 1.2.** Diagram of the relationship between pathological conditions, tissue ECM and measured parameters.

Figure 1.3 illustrates in detail the importance of choosing the right technique and model combination for retrieving certain information about tissue. Tissue can be viewed as a multi-dimensional feature space with each dimension to be a compositional or structural feature. Different mechanical characterization techniques will be sensitive to a subset of these dimensions, depending on the excitation methodology, scale, amplitude, and frequency. For example, Technique A applies the force in low-frequency range, thus the mechanical responses of this

technique might be sensitive to the number of collagen crosslinks, the amount of fluid that can flow freely, and the amount of proteins (e.g. resilin and elastin). When two rheological models A and B are applied to the mechanical responses from the same technique, they could yield a significantly different parameter space. The imitated example given on the right-hand side shows that Model A generates a parameter that has high sensitivity to the amount of open fluid inside the tissue, thus can separate two different tissue status. Model B is not suitable for extracting the information of fluid from the mechanical response when Technique A is used. In this case, the parameter estimated from Technique A and Model A is preferred for representing the open fluid in tissue. It is almost impossible for one combination of technique and model to be sensitive to all other features of tissue. It is ideal that a certain combination of technique and model can be found to produce high contrast for each feature of the tissue. The main goal of this thesis is to discuss how to identify the appropriate measurement technique and rheological model that can be used for targeting certain aspects of tissue properties.

The specific aims of this thesis are to 1) establish a platform for easy and reproducible measurements of the same material using three different modalities; 2) examine the relationship between technique and mechanical parameters by comparing the estimated mechanical properties measured from the three different techniques in elastic materials where the influence of rheological modeling is minimized; 3) examine the performance of different rheological models, and find a suitable model that can describe viscoelastic behaviors from different techniques; 4) find the relationship between the estimated parameters and the compositional and structural features of tissues and other viscoelastic materials. (also see Figure 1.4)

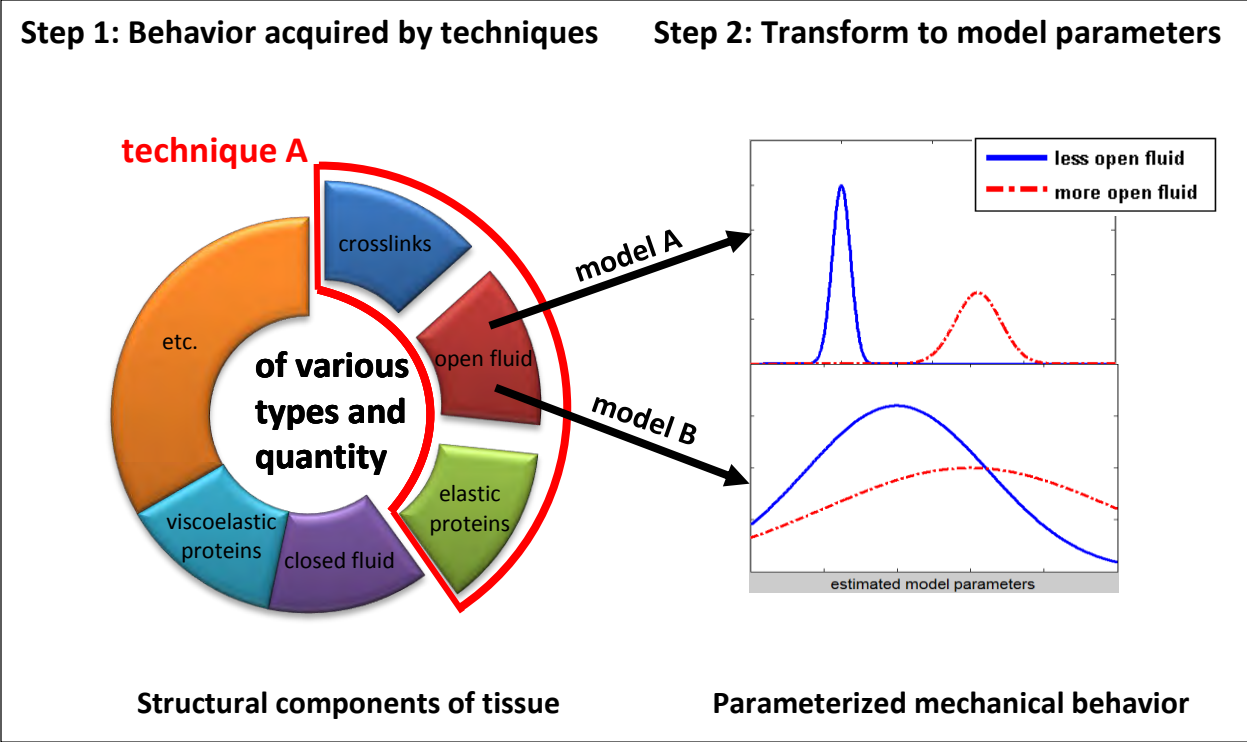


**Figure 1.3.** The role technique and model play in translating tissue compositions into model parameters.

<b>Measurement</b>	Developed two imaging techniques for reliably measuring the mechanical behavior of soft tissues, and validated the consistency of these techniques with indentation.
<b>Modeling</b>	For tissue and viscous materials, study the properties of different rheological models, especially KV fractional derivative model.
<b>Interpretation</b>	Relationship of KV fractional derivative model parameters to compositional and structural features of the viscoelastic material.

**Figure 1.4.** Specific aim for discovering the connections between measurement techniques, estimated model parameters and tissue feature space, in order to reveal diagnostic information.

Once the connections between the estimated model parameters, measurement techniques, and tissue feature space are understood, we will have a better interpretation of model parameters in terms of tissue compositions and conditions. The evolution of this field has the potential to bridge molecular, cellular, and tissue biology, and lead to new approaches in the treatment of patients, linking these pathological changes to the exact mechanical behavior at a mesoscale tissue level larger than the cell but smaller than the organ.

The outline for the remainder of this thesis is shown in Figure 1.5. Chapter 2 focuses on designing and advancing the indentation and shear wave imaging techniques, which facilitate quantitative estimations of mechanical material properties, both elastic and viscous. Three main techniques are presented, macro spherical indentation, ultrasonic shear wave imaging, and ARF-OCE imaging. Details on the measurement steps and basic theories are discussed for each technique. Several studies conducted on tissue-mimicking phantoms and rodent breast tumors are included to show the ability of these techniques in reliably acquiring the mechanical behaviors and estimating model parameters. In Chapter 3, the influence of techniques and models on the estimated mechanical property parameters is examined. The three aforementioned techniques are applied first to pure gelatin samples. Elastic modulus is estimated under the assumption that the gelatin is purely elastic with no time-varying elements. Given that the elastic modulus of an elastic material is not affected by the force frequency, the estimated elastic modulus should only be related to gelatin concentration, and not dependent on techniques used when there is no violation of geometric assumptions. Different techniques have different geometric limitations, and correction methods are proposed and implemented for samples with limited size. With the correction, the estimated elastic modulus is consistent with the geometry-independent estimation. This corresponds to Aim 1.

Then, I attempt to cross-validate the three techniques in viscoelastic materials such as tissues. However, there is no single model available for describing the mechanical responses for all three techniques in order for us to make a fair comparison. Instead, tissue measurement results showed that both technique and model will have influence on the measurement results to some extent. This motivates the identification of a model that can represent all three measurement techniques and also generate parameters that have diagnostic potentials.

Chapter 4 and Chapter 5 focus on finding one fractional derivative model that can interpret the elastic and time-varying properties for tissue. A gelatin-cream mixture phantom is used to mimic the time-varying properties in soft biological tissues. Chapter 4 focuses on introducing the Kelvin-Voigt fractional derivative (KVFD) model for mechanical indentation, which has proved to have enough flexibility and accuracy in various phantoms. This corresponds to Aim 3. Chapter 5 compares the KVFD model parameters yielded from both indentation and shear-wave imaging techniques, and explores the correlation of these parameters with compositions and structures of the materials. This part corresponds to Aim 4. Table 1.1 summarizes all the techniques and models mentioned throughout this dissertation.

**Table 1.1.** Summary of Techniques and Models

<b>modality</b>		<b>Indentation</b>	<b>Ultrasound</b>	<b>Optical</b>
On elastic material	Technique	Load-unload test (Chapter 3)	Shear wave imaging (Chapter 3)	Acoustic force (Chapter 3)
	Model	Hertzian model	Elastic tensor + Wave equation	Elastic tensor + Wave equation
On viscoelastic material	Technique	Force-relaxation test (Chapter 4, 5)	Shear-wave dispersion (Chapter 2, 3, 5)	KVFD model (Chapter 2, 3, 5)
	Model	Prony Series, absorbed energy, KVFD model	KV, Maxwell, Zener, KVFD model	KV, KVFD model

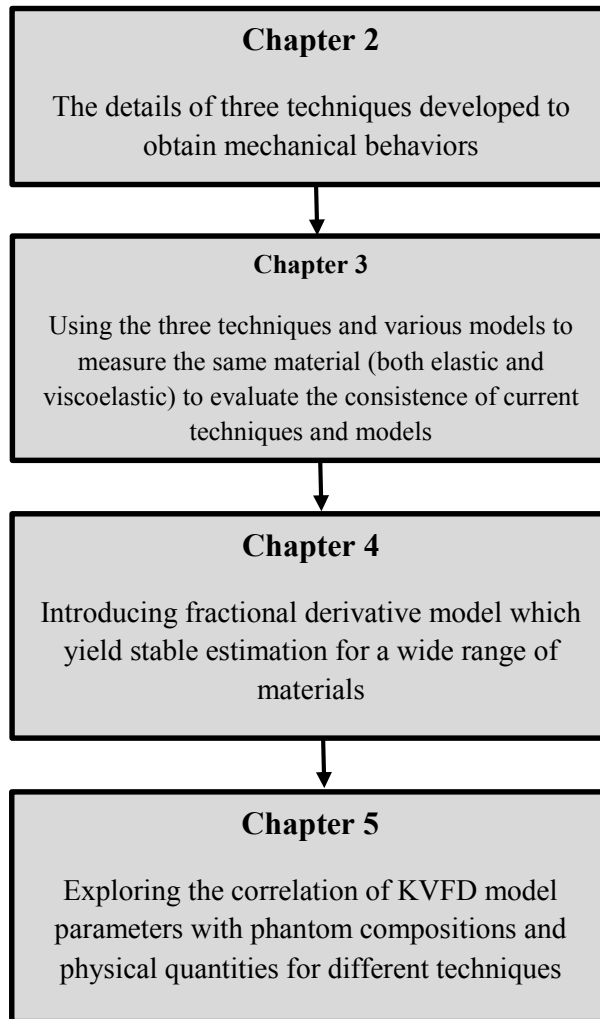


**Figure 1.5.** Flow chart for the content of each chapter

## CHAPTER 2: INDENTATION AND SHEAR WAVE IMAGING TECHNOLOGIES FOR QUANTIFYING MECHANICAL PROPERTIES

In this chapter, three techniques representative of low, median, and high frequency force ranges were developed to measure the mechanical property of tissue. They were calibrated using both numerical simulations and lab measurements on tissue-like phantoms. For the low frequency technique (up to 1 Hz), commercial indentation equipment with a spherical probe was used to record force behavior during compression and relaxation. Metrics such as Young's modulus, relaxation time, and hysteresis loss were estimated from low-frequency indentation tests. The mechanical properties at higher frequencies can be obtained from the propagation of mechanical waves. Median frequency shear waves were generated inside the material by an oscillating needle. Ultrasound Doppler imaging was used to measure the amplitude and phase of the shear waves. The generation of high frequency perturbation was facilitated by acoustic radiation force (ARF), and the motions at the material surface were monitored by optical coherence tomography technology. The goal of this chapter is to 1) develop the experimental process of the three techniques that can independently characterize properties of a viscoelastic material; 2) to validate dynamic wave imaging methods using tissue and tissue-mimic phantoms.

### **2.1 Indentation methods**

Indentation techniques are widely used for characterizing the mechanical properties of different kinds of materials. Mechanical characterization using indentation have received considerable attention during the last 20 years because of their simplicity and low cost. Some of the most used tests include load-unload test, relaxation, and creep test. From the stress-strain or

force-displacement curves measured by the indentation machine, information on elasticity, viscosity and other mechanical properties are obtained directly without mathematical modeling assumptions.

However, when implementing indentation techniques to measure soft tissues and tissue-like materials, many factors can cause substantial variations and biases to the stress and strain measurements. One possible influence comes from the adhesive force between the indentation probe and the sample surface, which will generate errors in the force measurement. Other factors such as roughness of the sample surface, the biphasic nature of tissue, and non-uniform geometries of samples are concerns in that they might violate the basic assumptions required by the analysis. Therefore, these challenges will need to be addressed before indentation techniques can be used reliably to study soft tissues. Because indentation techniques will be used throughout the thesis to compare with mechanical parameters estimated from dynamic imaging techniques, it is a necessary step to establish accurate and reproducible testing and analysis procedures for the application of indentation techniques in soft materials.

### **2.1.1 Load-unload test**

#### **a) Young's modulus measurements from load-unload experiments**

Load-unload test is a common indentation test for calibrating Young's modulus. The indenter travels slowly to deform the sample surface at a constant speed, and if the applied displacement  $\delta$  is within the linear region of the material, the measured force  $P$  can be expressed as [68]:

$$P = \frac{16E}{3} R^{0.5} \delta^{1.5} \quad (2.1)$$

where  $E$  is the Young's modulus of the material, and  $R$  is the radius of the spherical indenter which is known precisely. A power-law fit of the initial loading portion of the force-displacement curve to Equation 2.1 will yield the solution for  $E$ . The experimental process of load-unload test is illustrated in Figure 2.1 [68]. This Hertzian contact model has assumed the following:

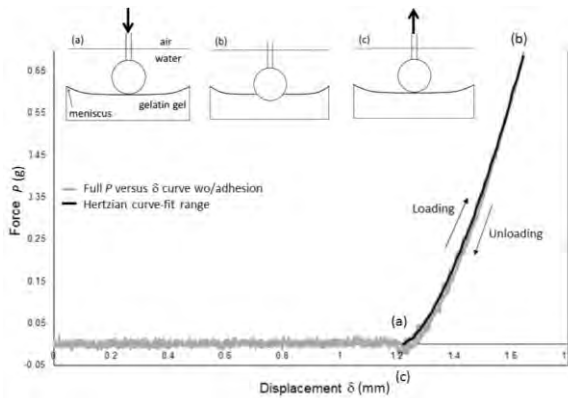
- i. The strains are small compared to the indenter size and the displacements are within the elastic limit. Also it is assumed that the sample surfaces are continuous.
- ii. The sample should be semi-infinite in size so that boundaries do not modify the force or displacement generated through the indentation. The material must behave as an elastic solid.
- iii. The indentation probe and the sample surface are in frictionless contact. There is no adhesion between the probe and the sample surface.

In order to satisfy these three assumptions for the experimental conditions, some additional steps must be included. For example, when using spherical indentation technique to measure soft materials, adhesion between the surface of the sample and the probe will significantly affect the correctness of initial contact force. Samples were tested under conditions where indenter-sample adhesions were minimized by adding a layer of water to the gel sample. To exclude the minor effect from indenter-water interaction, water was added to fully submerge the spherical tip of the indenter. Also, the probe surface was coated with a lubricant to further reduce the adhesion effect. Additionally, the shaft of the indenter probe was machined down to 1.5 mm diameter to reduce force-measurement bias from the water meniscus. It is verified that during the indentation process, the added water layer was not absorbed by our samples as the weight of the samples stayed

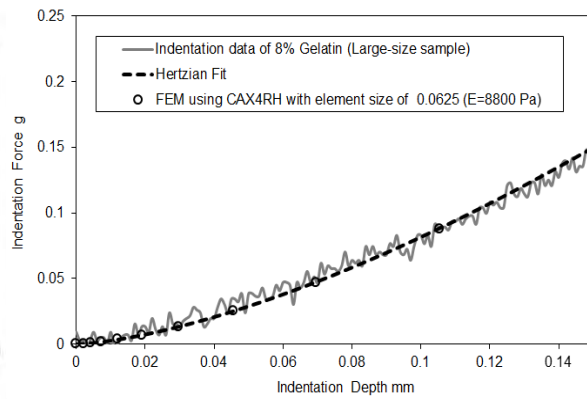
unchanged before water was added to the surface and after the water was totally removed after the measurement.



(2.1.a)



(2.1.b)



(2.1.c)

**Figure 2.1.** (2.1.a) Photo of indentation machine (TAXTplus, Texture Technologies Corp) used for all indentation tests. (2.1.b) The full loading and unloading portions of a force-displacement curve (gray line) when indenter-sample adhesions are eliminated by placing the contact surface under water. The sample for the data shown is 8% gelatin. The inserts diagram the experiments at three time points: (a) initial contact, (b) deepest indentation, and (c) as the indenter leaves the sample surface. Arrows indicate direction of the applied force. The solid black line segment is the section of curve fit to the Hertzian equation, Equation 2.1. (2.1.c) Indentation force-displacement curve is shown for the large-size 8% gelatin (solid gray) along with the Hertzian-curve fit (dashed black). Circles indicate force-displacement points generated from FE simulation using the modulus value  $E$  obtained from the Hertzian curve fit. [68]

Apart from these special treatments to satisfy Hertzian model assumptions, others have relaxed these restrictions via introducing new physical models or adding terms into the model, such as JKR theory (samples with adhesions) and Dimetriatis correction (samples with finite depth) [68]. It will be useful in the applications of tissue characterization.

**b) Loss-energy measurements from load-unload experiments**

When energy dissipation happens inside of the material due to internal friction and fluid flow, the force during the unloading phase is smaller than that applied during the loading phase, forming a hysteresis loop [69]. Hysteresis is a manifestation of time-dependent material properties, and is often used to characterize viscosity of the material. Figure 2.2 shows the hysteresis behavior of a typical viscoelastic material. The loss energy  $E_A$  can be measured from the area between the loading and unloading force-displacement curves,

$$E_A = \int_0^{T_z} ds (P_1(s) - P_2(s)) \quad , \quad (2.2)$$

where  $P_1(s)$  is the force on the probe measured during the loading phase of ramp indentation at constant speed and  $P_2(s)$  is that during the unloading phase at the same speed. When adhesions between the probe and sample surfaces are negligible with the probe being lubricated and submerged in water, viscous losses may be assumed to be responsible for generating the curve hysteresis.  $E_A$  can be used as a metric for time-dependent property of the material.

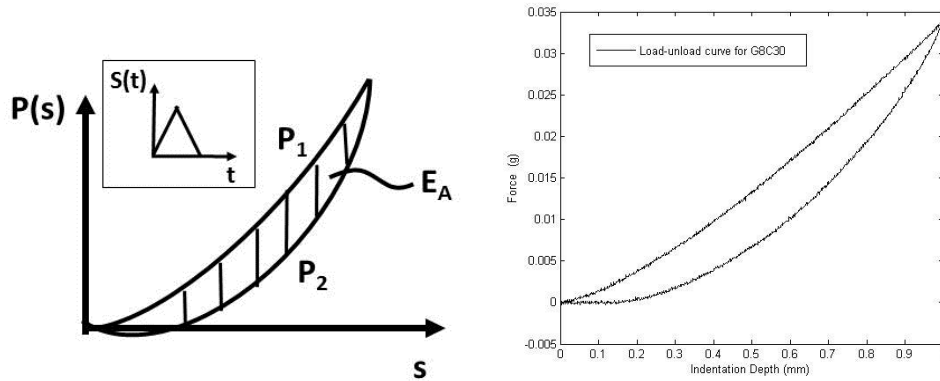


**Figure 2.2.** Diagram for load-unload experiments. Hysteresis behavior in viscoelastic material.  $P$  is the measured force,  $s$  is the indentation depth,  $T_r$  is the ramp time over which the probe tip is displaced into the sample surface to reach a 1 mm depth, and  $E_A$  is the loss-energy estimate found from the area between the load-unload curves once probe-sample adhesions are eliminated.

### 2.1.2 Ramp-relaxation test

The value of energy loss  $E_A$  depends heavily on many factors such as loading speed, load distance, and probe size. Therefore, creep tests or stress-relaxation tests are most commonly used in quantifying time-dependent behavior. The creep test is conducted by applying a constant force onto the material and observing displacement changes. Stress relaxation, on the other hand, is conducted by applying a constant displacement onto the material and observing the time-varying force. The creep curve and stress-relaxation curve are then fitted to a mathematical model to reveal the intrinsic properties of a viscoelastic material [70, 71].

A majority of stress-relaxation tests apply step compressions mainly for the analytical convenience of deriving a step-hold relaxation response solution. However, it is difficult to apply a near-step strain without creating oscillating transients that are more representative of the measurement device than the material. Unless the transients are accurately modeled, significant

errors in model parameters are generated. In contrast, the ramp-hold relaxation experiment dramatically improves model-fit stability by not generating measurement artifacts [72-75]. Figure 2.3 shows the force relaxation behavior in a lossy material. Given a ramp-hold displacement function with ramp duration  $T_r$  and constant probe velocity  $v$  (Equation 2.3),

$$s(t) = \begin{cases} vt, & 0 \leq t \leq T_r \\ s_{\max} = vT_r, & t \geq T_r \end{cases} \quad (2.3)$$

the relaxation force  $P(t)$  can be predicted through the use of models.

Analytical solutions for the ramp-hold experiment can be derived by combining the Boltzmann integral with the constitutive equation of a given model if a closed-form integral formula can be found. In cases where an analytical solution was not available for spherical-indentation testing for a specific model, a correction factor was applied analogous to that of the ramp-hold applied stress solution for a creep experiment to correct fitted parameters from a step solution [74]. The analysis demonstrated the feasibility and advantages of using ramp-hold applied strains to perform stress-relaxation tests.

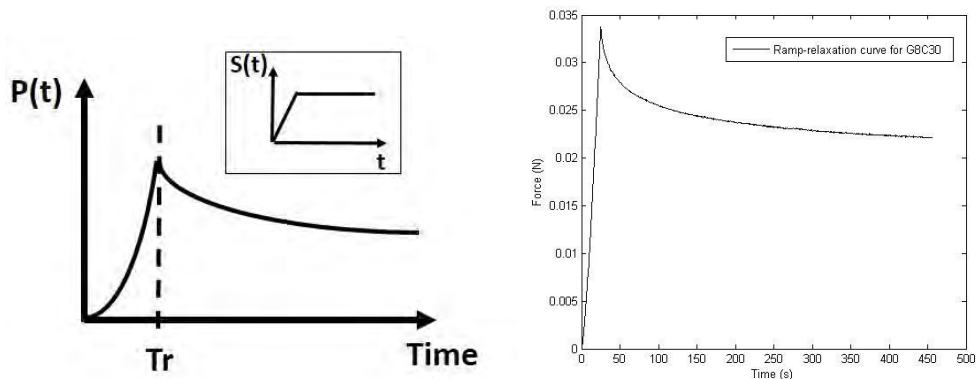


**Figure 2.3.** Diagram for ramp-hold relaxation.  $P$  is the measured force,  $s$  is the downward indentation depth,  $T_r$  is the ramp time over which the probe tip is displaced into the sample surface to reach a 1 mm depth.

## 2.2 Shear wave based methods

Compared to static compression or relaxation methods, in wave-based dynamic techniques, stress or strain is applied locally with adjustable frequency. Thus, the concerns of estimation bias from unknown stress distributions and boundary conditions outside of the ROI are reduced. Ultrasound and other phase-sensitive imaging modalities (MRI, optical coherence tomography) have been available for capturing the complex wave motion thanks to their high sensitivity to sub-millimeter-scale movements. Therefore, wave-based elastography techniques might have the potential to offer more accurate mechanical property information with high diagnostic value.

### 2.2.1 Complex shear modulus estimation from wave propagation - Theory

The theory of shear-wave propagation in viscoelastic media is well established [76, 77]. This section briefly summarizes the equations that describe local displacements associated with shear waves as a function of the spatially-varying complex shear modulus.

The relationship between strain  $\varepsilon$  and stress  $\sigma$  tensors can be expressed by the expression when displacements in the medium are small

$$\sigma_{ij} = C_{ijkl}\varepsilon_{kl}, \quad \text{where } i, j, k, l = 1, 2, 3, \quad (2.4)$$

where  $C$  is a fourth-rank tensor. For isotropic materials,  $C$  reduces to just two independent variables, the Lamé constants  $\lambda$  and  $\mu$ , where  $\mu$  is the shear modulus,

$$\sigma_{ij} = 2\mu\varepsilon_{ij} + \lambda\varepsilon_{nn}\delta_{ij}. \quad (2.5)$$

For external source (applied force)  $f$ , the equation of wave motion is

$$\rho \frac{\partial^2 u_i}{\partial t^2} = \nabla_j \cdot \sigma_{ij} + f_i , \quad (2.6)$$

which describes how stress influences the displacement-field vector  $\mathbf{u}$ . Usually stress is difficult to measure experimentally. Therefore, it is eliminated by substituting Equation 2.5 into Equation 2.6, using the definition<sup>1</sup>  $\varepsilon_{ij} = (\mathbf{u}_{i,j} + \mathbf{u}_{j,i})/2$  as well as the assumption that the analysis wave field does not include an active source. The result is

$$\rho \frac{\partial^2 \mathbf{u}}{\partial t^2} = \mu \nabla^2 \mathbf{u} + (\lambda + \mu) \nabla(\nabla \cdot \mathbf{u}) . \quad (2.7)$$

If we further assume that the contribution from longitudinal waves can be ignored, Equation 2.7 simplifies to

$$\rho \frac{\partial^2 \mathbf{u}}{\partial t^2} = \mu \nabla^2 \mathbf{u} \quad (2.8)$$

because the divergence of the shear-wave component and the curl of the longitudinal-wave component are both zero. If longitudinal-wave energy is significant, Equation 2.8 can remain valid by applying the curl operation to the displacement vector ( $\nabla \times \mathbf{u}$ ) to remove its effects.

Knowing the density of the medium  $\rho$  and estimating field  $\mathbf{u}$ , shear modulus  $\mu$  can be directly computed as a function of position from Equation 2.8. This is the Helmholtz inversion technique. Normally, the Helmholtz inversion is performed in the frequency domain, combined with heavy filtering of the displacement vector to avoid amplifying errors from the Laplacian in Equation 2.8. Finite element-based techniques have been developed to iteratively solve for  $\mu$  in a

---

<sup>1</sup> The partial derivative notation  $\mathbf{u}_{i,j} = \partial u_i / \partial x_j$ .

way that minimizes the error between simulated and experimentally acquired wave fields [78, 79]. The drawback of such techniques is a long computational time.

Alternatively,  $\mu$  may be estimated using a phase-gradient technique. For harmonic-wave motion, and assuming local homogeneity, Equation 2.8 reduces to

$$\rho\omega^2 = \mu k_s^2 . \quad (2.9)$$

In linear-elastic media, both  $\mu$  and  $k_s$  are real numbers representing, respectively, the shear modulus and the wave number at each location. In viscoelastic media, like most biological tissues,  $k_s = k_r - i\alpha$  is complex with real part  $k_r = \omega/c_s$  and imaginary part  $\alpha(\omega)$ , the frequency dependent attenuation coefficient for shear waves. Consequently, the shear modulus  $\mu(\omega) = \mu_r(\omega) + i\mu_i(\omega)$  is complex for viscoelastic media.

To measure  $\mu_r$  and  $\mu_i$  independently, both wave speed and attenuation must be estimated. It is very challenging to estimate shear-wave attenuation unless the wave-front geometry is well known. However, attenuation estimation is not necessary if a mathematical model is adopted to describe the behavior of  $\mu_r$  and  $\mu_i$  as a function of frequency. With the appropriate model, the shear-wave speeds dispersion curve is a function of model parameters (Equation 2.10) that are determined through least square fitting of Equation 2.10 to the dispersion curve.

$$c_s(\omega) = \sqrt{\frac{2(\mu_r^2 + \mu_i^2)}{\rho(\mu_r + \sqrt{\mu_r^2 + \mu_i^2})}} . \quad (2.10)$$

Shear-wave speed  $c_s$  is estimated from the shear-wave phase gradient along the direction of wave propagation, where rheological model parameters are obtained as a function of position. The range over which phase gradients yield accurate wave-speed estimates depends on the

homogeneity of the medium. There is an inherent tradeoff between spatial resolution and phase-estimation accuracy with this approach.

### **2.2.2 Wave generation and propagation**

Mechanical-wave stimulation/excitation is usually the key aspect that determines the quality of elasticity imaging. Except for passive elastography, which utilizes waves generated by physiological motion such as breathing and cardiac activities, most wave-based elastography techniques introduce exogenous waves with a controllable geometry, amplitude, and frequency bandwidth. Bulk and surface waves may be generated when pulsed or harmonic sources are applied. An impulse stimulus or a single-cycle sinusoid induces a broadband pulse wave with a group velocity that is predictive of tissue elasticity. Harmonic-force stimulus, on the other hand, generates a narrowband force-wave burst that improves the SNR for estimating wave speed and attenuation at each excitation frequency. In this dissertation, discussion is restricted to exogenous harmonic-wave stimulation and its applications for imaging mechanical properties of elastic and viscoelastic media.

Most readily accessible ultrasound machines only support two-dimensional echo acquisition. This restricts the direction of shear-wave propagation to be along the lateral direction of a 1-D array. Cylindrical waves and surface waves are widely used to mechanically excite tissues [80-85]. Other wave geometries, such as plane and Lamb waves, are used in some circumstance; for example, when imaging a vessel wall [84]. However, they are difficult to apply in media with amorphous structures like biological tissues. There are several advantages to use cylindrical or surface waves. Both wave geometries are easy to generate experimentally, for example, by vibrating a needle inserted into the medium [81], acoustic radiation force (ARF) [83], dual-focus

ultrasound transducer [85], or through a sequence of ARF pulses over a range of depths that generate a shock wave [22].

Cylindrical waves provide radially-symmetric excitation fields about the vibrating needle, making it possible to image tissues at any depth. Figure 2.4 gives an example of a cylindrical wave propagating in homogeneous gelatin gels (an elastic medium at these frequencies). A biopsy needle vibrating at 200Hz along the  $z$ -axis generates harmonic shear waves that are imaged by a Doppler probe (7 MHz, PRF 12.5 kHz). In the direction of shear-wave propagation, the phase of the wave shifts linearly while its amplitude decreases exponentially. Even if  $\theta \neq 0$ , the phase remains linear near the source at depths as much as 40mm in the gelatin gel. Ultrasonically-guided breast needle biopsy is an opportunity to excite tissues with harmonic cylindrical waves for shear-wave imaging without adding to patient risk.

There are several non-invasive techniques for generating approximately cylindrical waves in tissues, e.g., ARF impulses are commonly applied. Fink et al. [22] transmitted a sequence of ARF push pulses that excited a Mach-cone-shaped shear wave, which was approximately cylindrical for large Mach numbers. This method takes advantage of the fact that the speed of the compressional-wave ARF pulses in tissues is about 1000 times faster than that of the shear waves they generate.

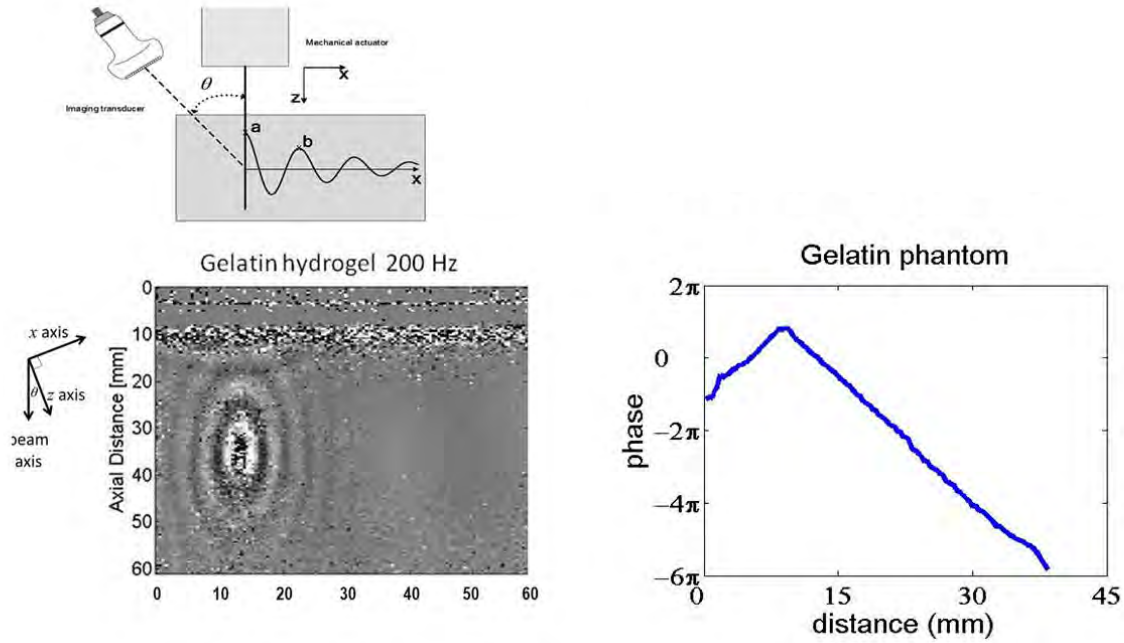


**Figure 2.4.** A vibrating needle generates patterns of 200 Hz cylindrical shear waves inside a gelatin block that are imaged using standard ultrasonic Doppler techniques at angle  $\theta$ . [81]. The elliptical shape of the wave field (lower left) is a consequence of  $\theta = 30^\circ$ . Horizontal bars of white noise near the top of the displacement image are from sample surface interactions. Measurements of a linear phase shift with lateral position about the needle are shown (lower right).

Rayleigh-type surface waves are generated when a forcing source is applied at or near a free surface of a solid sample [84], e.g., see Figure 2.5. Rayleigh waves are a mixture of shear and longitudinal particle motions, and yet its phase velocity can be directly related to shear-wave velocity by a constant between 0.92 and 0.96 depending on Poisson's ratio for the medium [87]. Although the speeds of surface and bulk waves are about 5% different, the amplitudes of both waves decay according to the geometric factor  $1/\sqrt{r}$  with distance  $r$  from a point source in elastic media. In more viscous media, the frequency-dependent shear-wave attenuation reduces the amplitude more rapidly. Thus, similar estimation algorithms are able to be applied for imaging surface and bulk transverse waves.

Surface waves are easier to excite from noninvasive sources than cylindrical shear waves, because the impedance discontinuity at the surface acts to strongly couple the transfer of pulse momentum to the medium surface. Surface waves travel with some depth in the medium. They propagate about one to two wavelengths in depth, so both optical and ultrasonic Doppler techniques can image this motion. Ultrasound is sensitive to transverse-wave particle motion over many centimeters of depth, while optical coherence tomography (OCT) is more sensitive to the small displacement amplitudes of high-frequency transverse waves only near the surface, approximately 1-2 mm deep [88]. High-frequency surface waves enable measurement of mechanical properties at higher spatial frequencies and with higher spatial resolution, which is particularly beneficial for imaging heterogeneous tissues.

One characteristic of surface waves is depth related velocity dispersion. The velocity of surface waves is a function of material property at each depth location that the wave penetrates. The wavelength of a surface wave and its penetration depth each decrease inversely proportionally to frequency. If the mechanical property of the material varies with depth, it will be reflected in the dispersion curve of surface wave velocity. This curve can be used to resolve spatially varying mechanical information in layered media if the material is not too strongly dispersive [89, 90].

Figure 2.5 illustrates images of surface waves in a homogeneous 8%-concentration gelatin gel using an ARF source applied from below. A compressional wave pulse traveling upward is totally reflected at the sample-air surface, thus generating a transverse surface wave. That surface wave travels horizontally with a cone-shaped geometry in the image plane near the source. In this example, 800 Hz waves are imaged using OCT to measure particle motion along the top surface of the sample [91]. The wave amplitude map for a 3 kHz source is also shown on the bottom left

of Fig 2.5. The top of the sample is located at depth  $z = 0$ , and the brightest spot at the center is the excitation source.

Cylindrical shear waves and radial surface waves have each been successfully applied in elasticity imaging. The choice of wave excitation methods depends on specific experimental conditions, as well as sample size, shape, and degree of inhomogeneity. In practice, transverse wave propagation is distorted by sample heterogeneities and boundaries that can bias shear modulus estimates. For example, distortion of the phase front will bias the shear-wave speed estimated using phase-gradient methods [92]. Most of these effects are minimized when the sample size is larger than two shear wavelengths. Internal wave reflections pose a significant challenge for 2-D ultrasonic phase measurements near tissue interfaces. In some cases, directional filters can help reduce the influence of reflected shear waves [93]. In highly attenuating media, reflections are less of a factor; instead, displacement SNR is the limiting factor for modulus estimation.

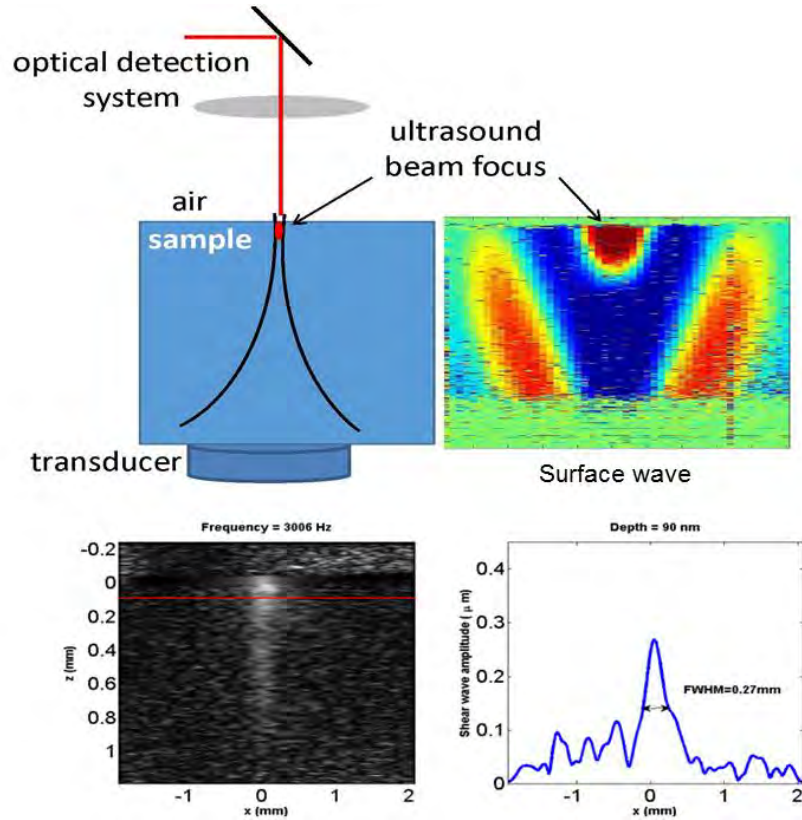


**Figure 2.5.** Acoustic radiation force geometry (upper left) generates surface waves inside a gelatin block (upper right) over a region approximately 1 mm x 4 mm. Lower left grayscale image shows optical coherence tomographic (OCT)-detected displacement amplitude for a 3 kHz ARF excitation. A plot of displacement amplitude at the depth indicated by the red horizontal line is shown on the lower right. [91]

### 2.2.3 Rheological models

The complex shear modulus  $\mu = \mu_r + i\mu_i$  as a function of frequency provides a model-independent metric that characterizes the viscoelastic behavior of a material under dynamic loading. Rheological constitutive models are proposed as a way to connect physical and experimental parameters to the real and imaginary parts of the property  $\mu$ ; for example, the Kelvin-Voigt (KV) model implies  $\mu_r$  is the elastic shear modulus  $E$  and  $\mu_i$  is the viscous coefficient times the radial frequency,  $-\eta\omega$ . That is, for  $\sigma = \mu\varepsilon$  the KV model gives  $\mu = E - i\omega\eta$ . Other models

have been proposed in attempts to summarize in just one or two imaging parameters values representing  $\mu$  for very complicated materials. The basic problem with these simple models is that tissues are not the material continua assumed. Tissues are better described as multiphase composites or sometimes as structures depending on the measurement scale. No model fully captures the constitutive complexity of soft tissues, which prompts some investigators to avoid them altogether by adopting methods that estimate  $\mu$  directly.

When models are assumed, the simplest and most-often applied are the Kelvin-Voigt (KV) and Maxwell models summarized in Table 2.1. The K-V model describes solid materials while the Maxwell model describes viscoelastic fluids, and both offer two parameters that are frequently mapped into elasticity images. Since soft tissue is neither solid nor fluid, a combination – the Zener model – is somewhat more realistic. Other models proposed include the Jeffrey model, generalized Maxwell model, generalized KV model, most of which are higher order combinations of KV and Maxwell elements [94]. Figure 2.6 shows the dispersion behaviors predicted by the different models.

**Table 2.1.** Comparison between Kelvin-Voigt model and Maxwell model

	<b>Kelvin-Voigt</b>	<b>Maxwell</b>
description	$\sigma = E\varepsilon + \eta \frac{d\varepsilon}{dt}$	$\frac{1}{E} \frac{d\sigma}{dt} + \frac{\sigma}{\eta} = \frac{d\varepsilon}{dt}$
$\mu$	$A \cos \varphi + iA \sin \varphi = E - i\omega\eta$	$\frac{i\omega\eta E}{E - i\omega\eta} = \frac{\omega^2 \eta^2 E}{E^2 + \omega^2 \eta^2} - i \frac{\omega\eta E^2}{E^2 + \omega^2 \eta^2}$

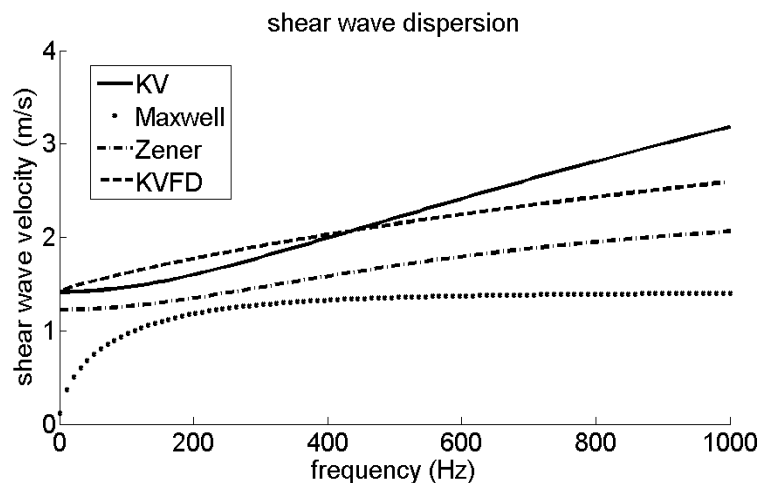


**Figure 2.6.** Dispersion curves as predicted by four rheological models over the same frequency range.

Among all these rheological models, there is no single model that is suitable for all types of materials. Figure 2.7 shows different dispersive behaviors in two types of materials. On the left is the dispersion curve of a viscous gel that is fitted to a Maxwell model, implying this gel has fluid-like properties. The model parameters are  $E = 5.58$  kPa,  $\eta = 2.9$  Pa·s. On the right is the dispersion curve of ex vivo porcine liver fitted to a KV model, implying solid material behavior. The model parameters are  $E = 1.75$  kPa,  $\eta = 0.4$  Pa·s. It is difficult to directly compare these modeling results of the materials because neither are a continuum. The viscous gel is an oil-based cream emulsified in gelatin (a composite material) and liver is a collagen polymer embedded in open- and closed-cell fluid compartments. New ways of representing complex mechanical structures are needed. Given that all models are limited in their ability to predict mechanical behaviors, we settle for those that yield physically-meaningful imaging parameters that are

sensitive to the presence of disease. The best models offer parameters that are correlated with inflammation, hyper-cellularity, fibrosis and other classic pathological biomarkers.

The solution is NOT to increase the number of parameters by adding coupled components to existing models. It is unlikely that more complicated models will enhance the diagnostic performance of elastography. Recently fractional derivative (FD) models are proving to be efficient in summarizing the dynamic behavior of viscoelastic materials over a wide frequency range with just 2-3 parameters. [64, 95] There is new hope in these recent efforts to model tissue mechanics using fractional derivative models [96]. These models may help resolve the solid-fluid duality of soft biological tissues [97] by offering a compact feature space that is sensitive to disease states.

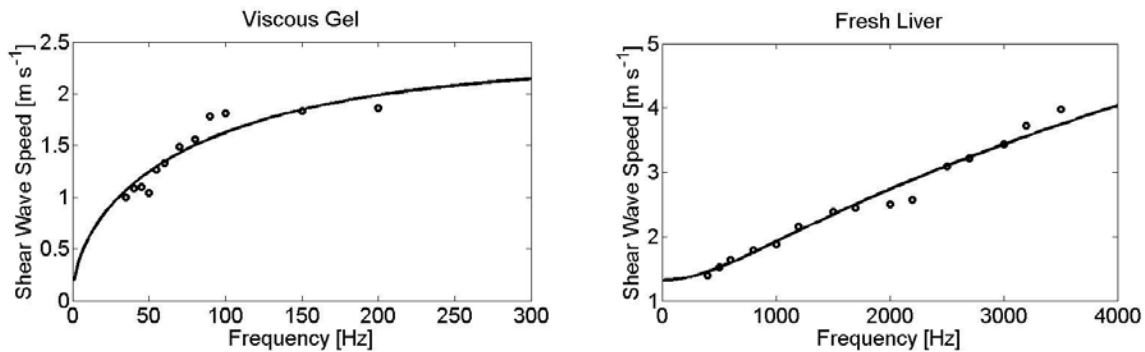


**Figure 2.7.** (left) Dispersion curve of viscous gel measured by ultrasonic shear wave imaging technique, with Maxwell model fit. (Right) Dispersion curve of an ex vivo fresh porcine liver measured by optical surface wave imaging, with Kelvin Voigt mode fit.

### 2.3 Ultrasonic shear-wave imaging using vibrating-needle stimulation

Ultrasonically-guided breast needle biopsy is commonly used. Needle insertion provides an opportunity to vibrate the needle and excite harmonic cylindrical waves for shear-wave imaging with a well-known shear-wave-field geometry (Figure 2.4). This section summarizes the implementation, validation and in vivo application of the biopsy needle based ultrasonic shear wave imaging technique. Phantom measurements demonstrate the feasibility and reproducibility of the measurement. Rodent mammary tumor studies examine the potential of this technique as a diagnostic test in clinical applications. In the end of this section, the influence from reflecting waves is studied using both simulations and experiments, and the directional filter is applied to minimize this effect in order to improve the accuracy of the measurements.

Experiments are conducted on the SonixRP ultrasonic system (Ultrasonix Medical Corporation, Richmond, BC) using a BW-14/60 linear array probe. Pulsed Doppler techniques are applied to record the particle velocity field. Local shear wave speeds are then estimated from spatial-phase gradients. Spatially averaged estimates of shear-wave speed at different oscillatory frequencies form a dispersion curve, which can be fitted to prediction rheological models to estimate model parameters. Details of the acquisition, modeling, and signal processing are described in [81, 92].

### **2.3.1 Validation measurement in homogeneous gelatin phantom**

Six homogenous gelatin gel phantoms were prepared with gelatin concentrations of 4% and 8% (three samples per concentration for mean and standard deviation estimates). The phantom size was  $125 \times 95 \times 95$  mm<sup>3</sup> in volume. A needle was inserted near the center of the gel block and vibrated axially with a mechanical actuator driven by a single-frequency sinusoid. Narrow-band

shear waves at frequencies between 50 and 450 Hz were generated and imaged using a Doppler probe. The angle between the vibrating needle and the beam axis was set to  $30^\circ$  to allow imaging of the needle and surrounding regions. Figure 2.8 illustrates the experimental setup for the validation studies of biopsy needle based ultrasonic shear wave imaging technique.

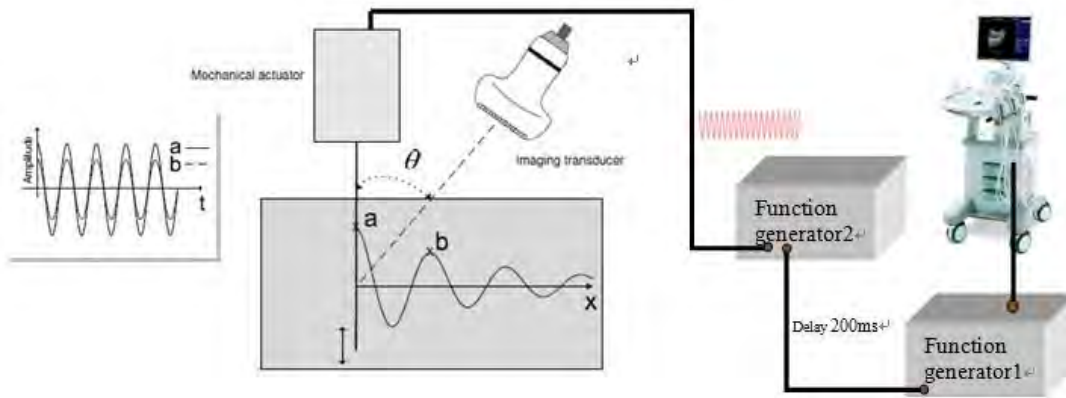


**Figure 2.8.** Diagram of hardware for ultrasonic shear wave imaging experiment to measure viscoelastic properties of gelatin samples. The mechanical actuator is driving a stainless steel needle oscillating at a single frequency. Momentum of the needle displacement is transferred to the medium as attenuated cylindrical shear waves. A linear array Doppler probe tracks the induced transverse motion of scatterers as shear waves propagate.

Shear wave speeds as a function of frequency were measured for each concentration and fitted to Kelvin-Voigt model (shown in Figure 2.9). The results from shear wave imaging are listed in Table 2.2, compared with rheometer results measured independently. Good agreement exists between the rheometer-estimated elastic shear modulus and the one estimated by the ultrasonic shear wave imaging. Therefore, it is feasible to obtain the shear modulus of a homogeneous material through cylindrical shear wave propagation.

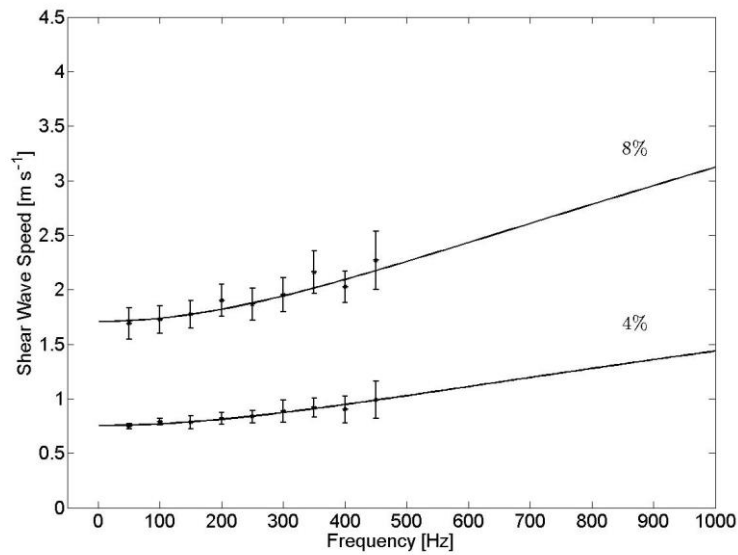


**Figure 2.9.** Dispersion curves for two homogeneous gelatin phantoms of 4% and 8% concentration. Solid lines represent least-square fit to Kelvin-Voigt model.

**Table 2.2.** Measurement results of homogeneous gelatin phantoms

Gelatin concentration	RHEOMETER [PA]	$\mu$ [Pa]	$\eta$ [Pa·s]
4%	571±67	571±105	0.21±0.06
8%	2286±315	3068±321	0.84±0.45

### 2.3.2 Validation measurement in inhomogeneous gelatin phantom

Biopsy needle based ultrasonic imaging technique is further validated through an inhomogeneous gelatin phantom. In this study, 3D shear wave field was captured using 2D

ultrasound transducer. Inhomogeneous gelatin gel phantoms were prepared as follows. First, an 8% gelatin gel was formed in the acrylic phantom mold that contained a 15mm-diameter cylinder. After congealing 24 hours, the cylinder was removed and the hole was refilled with 4% gelatin and allowed to congeal for another 24 hours. To image shear waves in the 3D volume surrounding the vibrating needle, pulsed Doppler velocity data were acquired by scanning parallel scan planes separated in elevation by 1 mm increments. In these experiments, the angle between the needle and beam axis was  $0^\circ$ . Meanwhile, a numerical simulation developed by our group to simulate shear wave propagation in viscoelastic media [98] has been used for two purposes: First, simulations provide the 3D velocity data comparable to the phantom measurements that enabled the verification of the accuracy of the solver. Second, this activity helped understand how wave reflections and refractions in inhomogeneous media affect the estimation of viscoelastic properties.

In the simulation, FDTD (Finite-Difference Time-domain) method is used to solve the wave equation in solid media. It is known to be more robust and less computationally expensive when compared with FEM (Finite Element Methods). To minimize computation time, only shear wave propagation is simulated. Longitudinal waves travel much faster and thus require smaller time steps. Since they do not interfere with shear waves, they can be ignored with little effect. An absorption layer was added to boundaries. Values of complex shear modulus set in the simulation were compared to those measured in gel samples. The soft inclusion, which has a 4% gelatin concentration, was assigned an elastic shear modulus of 1100 Pa and a viscous constant of 0.1 Pa·s. The 8% gel background was assigned an elastic shear modulus of 4000 kPa and a viscous constant of 0.5 Pa·s.

In both experiments, a needle was vibrated axially with pure sinusoid at 100Hz frequency. 3D estimates of the z-axis (parallel to the axis of needle vibration) velocity component,  $\mathbf{u}_z$ , were

obtained in time sequence (Figure 2.10). I matched the spatial region in the simulation to that recorded experimentally. In Figure 2.11, the comparison of shear wave particle velocity field between simulated and experimental data is illustrated for simulation time  $t_{\text{sim}} = 78\text{ms}$ . Similar wave patterns are observed in both the experimental and simulation examples. The lateral line cut through the center of inclusion for both simulated and experimental data was also plotted. The change in wavelength of the shear wave as it propagates through the soft inclusion can be observed in the region from 4mm to 19 mm which corresponds to the 15 mm diameter of the inclusion in both the simulation and the experiment. Small differences between simulated and experimental data are explained by the variability of the mechanical properties of gelatin samples of up to 20 % [67, 81].

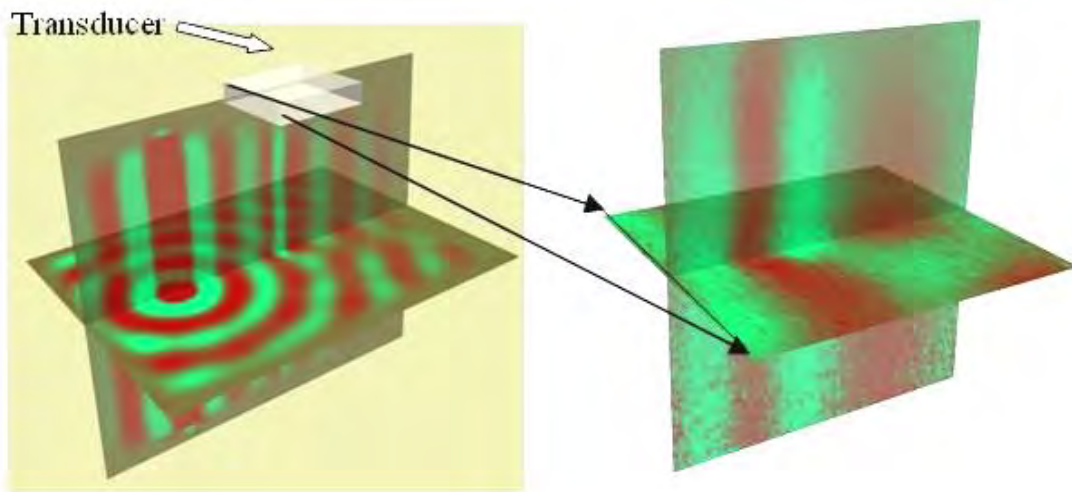


**Figure 2.10.** (a) Crosscut and vertical cut of 3D FTDT simulated velocity field (left). Experimental data collected by linear array transducer (right).

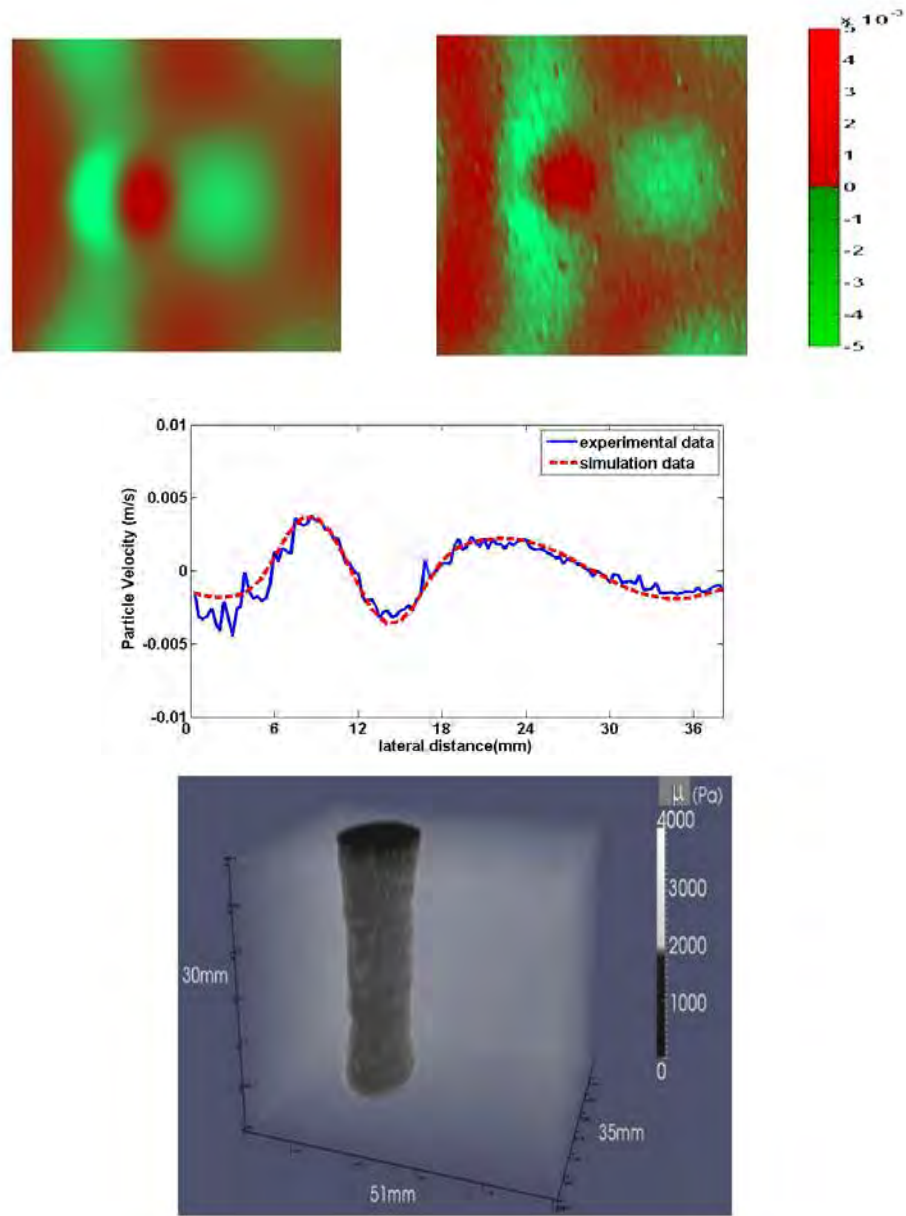


**Figure 2.11.** (Upper) Comparison between simulated and experimental data over lateral space. (Middle) Comparison of the spatial wave patterns for the lateral cut through the center of inclusion for the same time cut. Two are in good agreement in terms of the spatial wavelengths and attenuation. (Lower) 3-D shear modulus reconstruction of the cylindrical inclusion.

It is demonstrated that the developed 3D FDTD solver is an accurate tool for simulating shear wave propagation through soft viscoelastic biomaterials. Furthermore, the feasibility of using

a 1D linear array to collect 3D volumetric velocity data is shown. The developed simulator is the first step in solving a 3D inverse problem for complex shear modulus reconstruction. It provides a unique opportunity to conduct experiments *in silico*, and to study the effect of realistic viscoelastic biological material properties on contrasts observed in shear wave images.

### **2.3.3 Shear modulus quantification of rodent mammary tumors**

This dynamic methodology for quantifying complex shear modulus was applied on rodent mammary tumors. The goal is to examine whether ECM properties and disease states can be translated into viscoelastic properties measured through waves propagating in tissues using the technique developed. Measurements were compared with histology and chemical analysis to determine tumor types and ECM components.

Toward this goal, the properties of two types of rodent mammary tumors are measured: rat fibroadenoma and 4T1-implanted mouse carcinoma. Fibroadenoma is a benign, spontaneously-occurring tumor characterized by a hyper-proliferation of normal type I stromal collagen. The collagen fibers in the ECM matrix are assembled with hydrogen bonds that will break and reform when stress is applied over a period of time. The concentration and architecture of collagen proteins in the ECM are responsible for many mechanical properties of mammary tissues [99]. In contrast, 4T1 cells are a metastatic late-stage mammary carcinoma line. Due to high MMP secretion and other properties, 4T1 cells generate tumors with very little ECM collagen. However, the fibers that are present are highly linearized compared to the winding shape in benign fibrous tumors [100].

## **Experimental setup and procedures**

*Animal models:* Four Sprague-Dawley female rats (Harlan, Indianapolis, IN), aged from 5 to 10 weeks, that had developed spontaneous mammary fibroadenomas of size 2 to 4 cm were used for evaluation. The tumors appeared grossly homogeneous in morphology and consisted of abundant fibrous connective tissue with a high collagen density. Manual palpation revealed a variation in stiffness among these tumors and animals. For carcinoma tumors, syngeneic orthotopic xenograft mouse tumors were induced by a late-stage metastatic mouse mammary cancer cell line 4T1 (CRL-2539, ATCC, Manassas, VA). The tumors grew a relatively uniform morphology, characterized by a high density of cells and little ECM. 4T1 cells were stored, cultured and collected as the ATCC protocol recommended. Tumors were implanted by subcutaneous injection of  $10^4$  4T1 cells suspended in 50  $\mu$ l of cell media into the 4<sup>th</sup> and 9<sup>th</sup> mammary pad of a normal 8-16 week-old BALB/c mouse. The injection site was monitored daily until the tumor reached 1 cm in size, when its mechanical properties were measured in vivo. Injected cells initiated tumor growth in 80% of the animals. The tumor size grew rapidly at the injection site during the first 2-3 weeks, then growth slowed as the tumor mass stiffened. Although larger tumors are easier to manipulate, image, and analyze, large tumors often formed a necrotic core. To minimize necrosis, tumors were scanned once they reached 1.0 cm in diameter. The experimental protocol was approved by campus Laboratory Animal Care Advisory Committee.

*Imaging procedures:* A SonixRP system (Ultrasonix Medical Corporation, Richmond, BC, Canada) was used for ultrasonic imaging. All rodents were anesthetized with a combination of ketamine hydrochloride (87 mg/kg) and xylazine hydrochloride (13 mg/kg) under a protocol approved by the Institutional Animal Care and Use Committee at the University of Illinois. The

skin of each anesthetized animal was shaved in the region around the tumor before imaging. The animal was placed on an acrylic plate in a prone position and submerged in 37 °C degassed water bath with its head above of the water surface. The water provided an acoustic window for non-contact ultrasonic scanning and thermal control during anesthesia. B-mode imaging of the tumor was performed to select a Doppler imaging plane. Then a 17-gauge stainless-steel needle was inserted vertically into the tumor under ultrasonic guidance to select the needle depth and avoid damaging large vessels. A L14/38 linear-array Doppler probe scanned the tumor in a plane at a fixed scan angle of 30° relative to the needle axis. The transmit focus of the ultrasound beam was set to the center of the measurement field of the tumor. Transmitting ultrasound center frequency is 7 MHz. A mechanical actuator vibrated the needle harmonically for 0.3s along its long axis (z-axis). The acquisition sequence of the linear-array probe was synchronized to the actuator, with the pulse repetition frequency (PRF) set to 12500 Hz in Doppler mode with Doppler packet size to be 6. The actuator vibration frequency ranged from 50 Hz to 450 Hz in increments of 50 Hz. The peak-to-peak voltage of the actuator was set to a low level (2V) to avoid needle slippage and mechanical nonlinearities, but at some cost of velocity SNR. See Figure 2.12 for setup details. The actual tissue displacement at the center of needle is several micrometers (1-9 micrometers) depending on the excitation frequency and tissue stiffness.

*Histology:* After velocity acquisition, the tumor was excised immediately after the rat was euthanized. Three cylindrical samples were cut from each tumor for shear rheometer testing. Other parts of the tumor were fixed, stained (hematoxylin and eosin) and sliced for standard histological analysis that identified tumor types. The histology results were examined by a doctor. The rat tumors were diagnosed as mammary fibroadenomas each with a different ECM content that correlated with tumor age. All mouse tumors were diagnosed with anaplastic mammary carcinoma.

Diagnostic reports from a professional pathologist showed minimal difference among these tumors. The tumors were densely cellular, infiltrative with a few interspersed ingrowing capillaries. Figure 2.13 shows histopathologic slides of two representative mammary fibroadenomas and one representative mammary carcinoma.

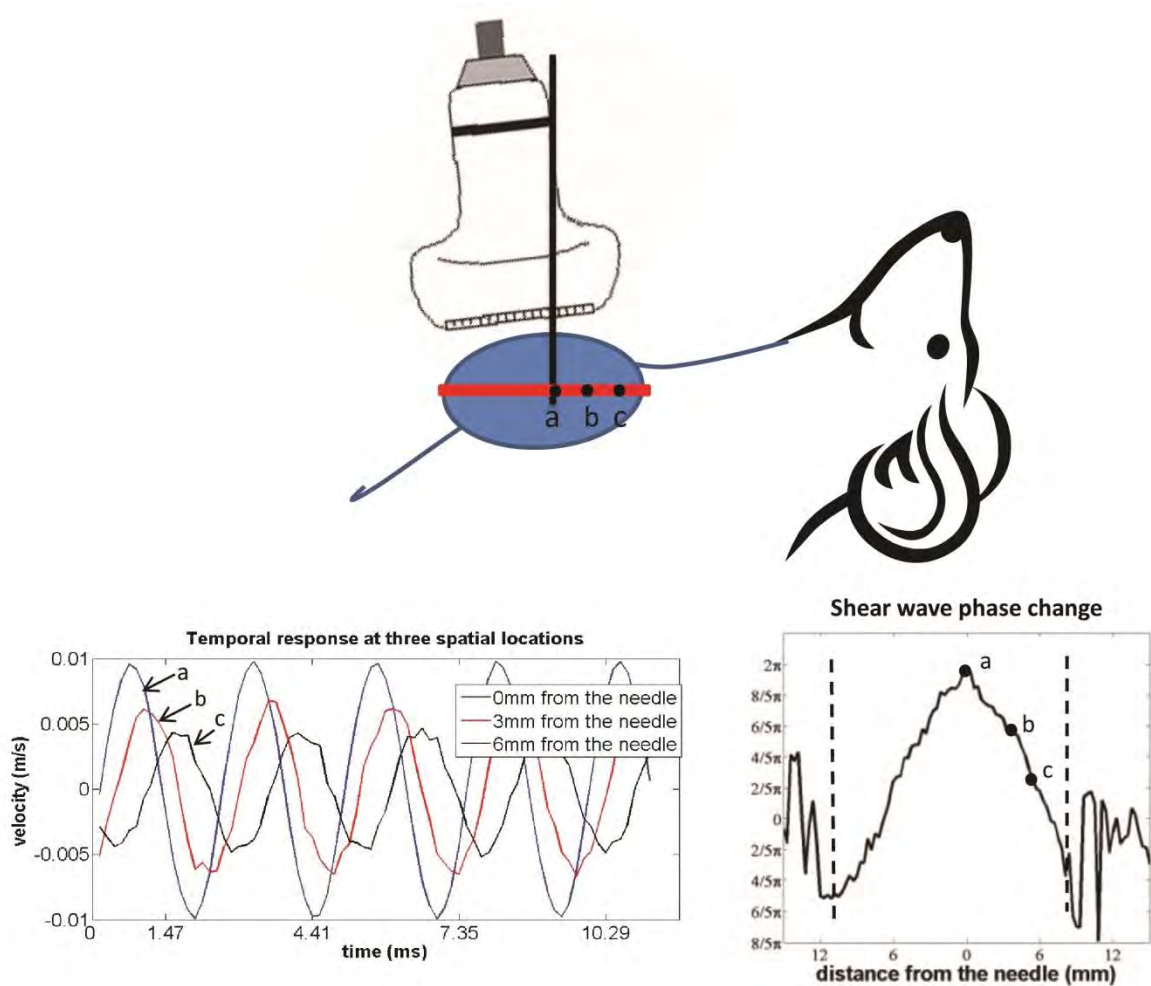


**Figure 2.12.** In vivo setup used for ultrasonic shear wave imaging experiments. The z axis is aligned along the long-axis of the needle. The x axis is normal to z and in the scan plan of the Doppler probe (red line in the top diagram). Lower left figure demonstrates the harmonic movement at three different locations on the tumor. Lower right figure shows the phase of the harmonic movement over the measured spatial locations at 400 Hz.

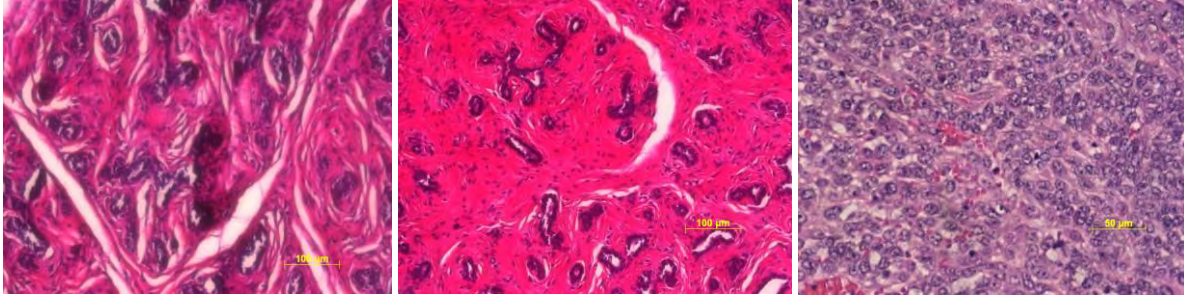


**Figure 2.13** Optical microscope images of H&E stained tumors. On the left is an early-in-development rat fibroadenoma tumor, and in the middle is a mature rat fibroadenoma tumor with densely packed collagen fibers (both images are at 40X). On the right is a sample from a mouse carcinoma (80X).

*Collagen content:* Hydroxyproline assays were performed on three samples per tumor to measure the collagen-protein content following the assay protocol of Samuel [101]. Hydroxyproline content can be used as an indicator to determine collagen content [102].

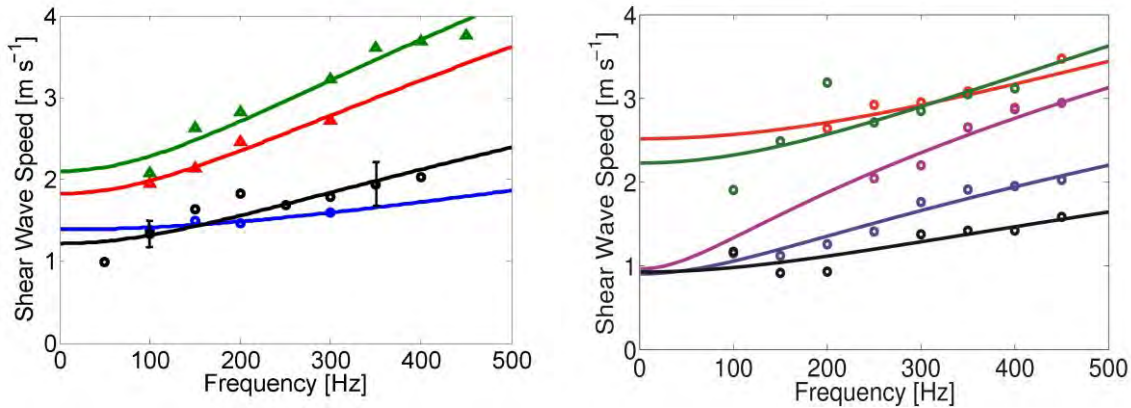
## Result

Figure 2.14 shows the shear-wave dispersion curves measured in vivo on four rat fibroadenoma tumors and five mice carcinoma tumors. The shear-wave speeds for each tumor were fit to a Kelvin-Voigt rheological model to estimate the complex modulus coefficients,  $\mu$  and  $\eta$  (see Equation 2.10 and section 2.2.3 for modeling detail). Modeled curves were fit to measured data by selecting model parameters that minimized the reduced  $\chi^2$  statistic,

$$\chi^2 = \frac{1}{N-n-1} \sum_{i=1}^N \left( \frac{\hat{c}_i(\omega) - c_i(\omega)}{\sigma_i(\omega)} \right)^2 \quad (2.11)$$

where  $N$  is the number of different frequency observations and  $n$  is the number of model parameters.  $\chi^2$  is an indicator for the goodness of fitting between model and the shear wave dispersion curve. The fitting modulus coefficients are listed in Table 2.3 and Table 2.4.

Histological analysis of these tumor tissues revealed that the fibroadenomas in rats 1 and 2 were in the early stage of development (Figure 2.13 left, where the tissue is less fibrotic and the ducts retain a normal shape). Conversely, the lesions in rats 3 and 4 were at the latter stage of fibroadenoma development (Figure 2.13 middle, where there is denser fibrosis and the ducts have collapsed). Carcinoma tumors were of different sizes and necrosis stages. Histology revealed that tumors were composed almost entirely of cancer cells with minimum fibrotic changes. (Figure 2.13 right).



**Figure 2.14.** (left) Dispersion curves measured in four different rat fibroadenomas. ‘ $\circ$ ’ denotes the measured shear-wave speed of early stage fibroadenoma tissues and ‘ $\Delta$ ’ denotes that of the more mature fibroadenomas. Solid lines represent the best-fit K-V model curves. (right) Dispersion curves measured in five different mouse carcinomas. Solid lines represent the best-fit K-V model curves.

**Table 2.3.** Estimates of shear modulus coefficients for rat fibroadenomas

fibroadenoma	$\mu$ [Pa]	$\eta$ [Pa·s]	$\chi^2$
1	1832.2	0.9	0.86
2	1485.6	1.16	4.52
3	2728.6	3.46	9.55
4	4420.4	3.54	2.71

**Table 2.4.** Estimates of shear modulus coefficients for mice carcinomas

carcinoma	$\mu$ [Pa]	$\eta$ [Pa·s]	Tumor size [mm]	Line color
1	857.0	0.56	11.0	black
2	894.4	0.95	11.4	blue
3	926.9	1.78	10.5	magenta
4	4464.6	2.5	16.5	green
5	6343.1	2.4	14.1	red

The rat and mouse mammary tumors were vastly different in structure and composition. Since collagen is a cancer biomarker and the principal component of stroma responsible for tissue viscoelastic properties, the collagen content of each tumor is measured to compare with measured mechanical properties (see Figure 2.15). It is found that rat fibroadenomas are in the range of 85-110 mg hydroxyproline/g dry tissue. This range overlaps values reported for human breast fibroadenoma [103, 104]. In contrast, the 4T1 mouse carcinoma model contains very little ECM collagen, generally in the range of 1-8 mg hydroxyproline/mg dry tissue. Note that hydroxyproline constitutes 15% of total collagen content [102], so the collagen concentrations are roughly seven times larger than the hydroxyproline concentration values reported in Figure 2.15. Hypothesis testing shows there is a good correlation between modulus parameters and collagen content in both rat fibroadenoma (correlation coefficient equals 0.95 for  $\mu$ , 0.81 for  $\eta$ ) and mouse carcinoma (correlation coefficient equals 0.93 for  $\mu$ , 0.99 for  $\eta$ ). These data yield strong evidence that the elastic shear modulus is highly correlated with collagen content.

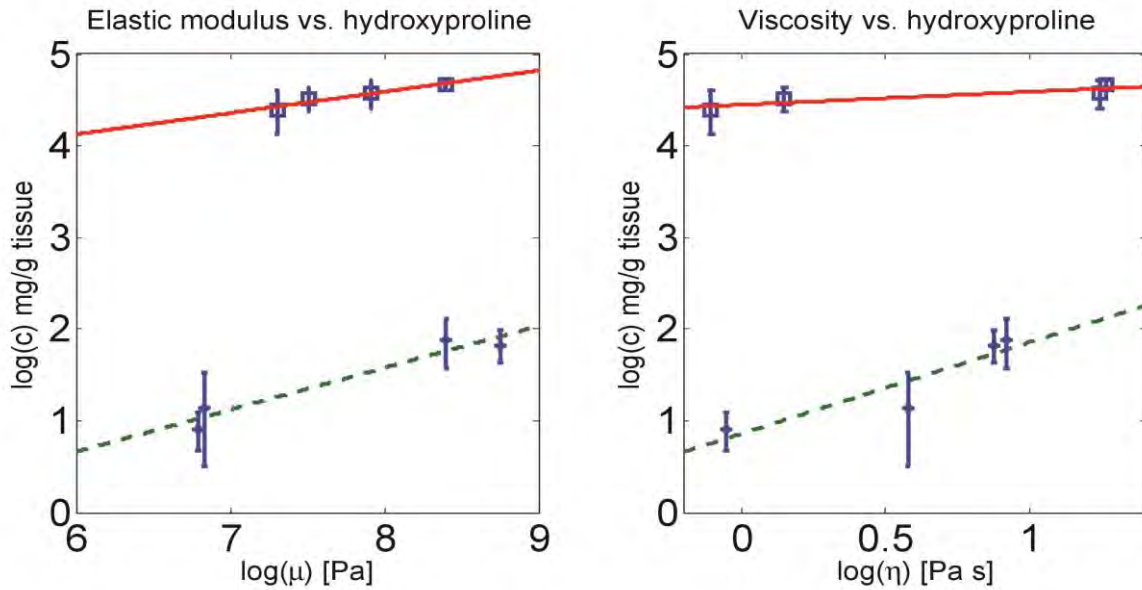


**Figure 2.15.** The hydroxyproline concentrations measured for rat fibroadenomas are plotted on a log-log scale as a function of the corresponding tissue elasticity measurements in the upper curve. The same quantities were measured for mouse carcinomas and plotted in the lower curve. Assuming there is a power-law relationship between these measurements of the form  $C = A\mu^n$ , we find  $n = 0.46$  and  $A = 0.12$  mg/g for the mouse carcinomas (lower curve) and  $n = 0.23$  and  $A = 15.3$  mg/g for the rat fibroadenomas. Error bars indicate one standard error. Also note that we can write  $\mu = BC^m$ , where  $B = (1/A)^{1/n}$  and  $m = 1/n$ .

## Summary

The measurements on two rodent tumors have provided insights into the mechanical behavior of collagen-rich fibrotic tumors (fibrosis) and cell-rich hyperplastic tumors (hyperplasia) respectively. In the frequency range of 50-450 Hz, both types of tumors display similar dispersion curves. Complex shear modulus is estimated using Kelvin-Voigt (KV) rheological model.

Preliminary results demonstrate that the elastic coefficient  $\mu$  reflects the same fibrotic stage of the tumor that observed histologically. The viscous coefficient estimated from the K-V could also reflect this change. Later collagen quantification reaffirmed the qualitative assessment from histology that the tumor stiffening was the consequence of the increase in collagen concentration. Dispersion curves and viscoelastic moduli of mouse carcinomas exhibit more variation and size

dependency mainly because it is heavily affected by boundary reflection, as Table 2.4 shows. In mouse carcinomas, shear wave speeds were underestimated to some degree due to that the tumor diameter is too small.

## **2.4 Acoustic radiation force optical coherence elastography (ARF-OCE)**

Optical imaging can in principle provide higher resolution and improved sensitivity to tissue displacements than ultrasound, owing to the much shorter wavelength of light. Laser speckle imaging has been utilized to evaluate the mechanical properties of tissue phantoms and various biological samples, including cortical bone and arteries, as well as natural and engineered normal and cancerous skin tissues [105, 106, 107]. Recently, digital holographic techniques have been developed to provide wide-field imaging (over tens of millimeters) of surface acoustic waves, with the ability to reconstruct 3D depth-resolved mechanical properties from the frequency-dependent velocities (dispersion curve) of these waves [108, 109].

In terms of wave excitation, needle excitation discussed in previous section provides cylindrical shear waves at frequencies less than 800 Hz. Acoustic radiation force can provide excitation frequencies as high as 10 kHz, which enables high-spatial-resolution imaging. The larger bandwidth results in much smaller shear-wave amplitudes that are too small for ultrasound detection, but perfectly matched to the detection and sensing capabilities of OCT.

The radiation force generated from a focused acoustic beam on the medium is proportional to the absorption coefficient of the tissue and the time-average beam intensity [110]. Thus, the applied force is the largest at the beam focus within an attenuating medium. The magnitude of the force is related to the medium and the sound intensity:

$$F = \frac{2\alpha I}{c} \quad (2.12)$$

where  $\alpha$  is the absorption coefficient,  $I$  is the intensity of ultrasound, and  $c$  is the longitudinal wave speed in the medium. The acoustic radiation force can be used as the driven force for more localized excitation. Since the penetration of OCT in scattering samples is limited to about 1-2 mm, the acoustic beam was focused on the top sample-air interface to generate shear waves that propagate near the surface of the sample. In the experiments, the high impedance discontinuity at the sample-air surface act like a drum membrane, which dominants the excited wave to be a Rayleigh wave or surface wave. The propagation speed of Rayleigh wave is 5% slower than the corresponding shear wave [113,114,115]. A circular, single-element 8 MHz, f/1 transducer is selected to deliver the acoustic radiation force. The small f-number keeps the force-excitation focused to an area about the size of the sound wavelength, in this case, 0.2 mm. The magnitude of the acoustic force was easily controlled by the transducer driving voltage. Harmonic-wave excitation was achieved by modulating the continuous-wave 8-MHz amplitude anywhere in the range of 100 to 10,000 Hz. Thanks to the high phase stability and SNR of OCT, movements as small as 10 nm can be readily measured. The low driving force of the transducer allowed forces to be applied continuously without heating. Acoustic radiation exerts forces in only one direction, thus harmonic oscillations generate a net displacement in tissue that depends on frequency and tissue properties.

The reason for introducing ARF-based optical coherence elastography (OCE) is to allow low-amplitude, broad force frequency bandwidth shear waves imaging for assessing viscoelastic properties of tissues at high spatial resolution, which is needed in basic science investigations and some clinical scenarios.

This section will demonstrate the feasibility of using ARF-OCE to map the shear-wave speeds first in polymer materials for calibration and later the mammalian liver tissue samples during fixation.

Shear wave modulation frequencies from 200 Hz to 5 kHz are easily achievable at A-scan rate of 65,000 A-lines per second. The shear waves with frequencies as high as 10 kHz have been imaged using this method. The analytic signal was computed from the raw optical data acquired in M-mode, and was used to calculate the phase difference between adjacent A-lines at each axial position as a function of time. As in ultrasound displacement detection, phase wrapping was avoided. Figure 2.16 illustrates spatial patterns of displacement when a harmonic acoustic force is applied at the top surface of the sample. The largest displacements appear at the ultrasound-beam focus. Both the magnitude and width of the displacement pattern depend on the carrier frequency of the sound waves.

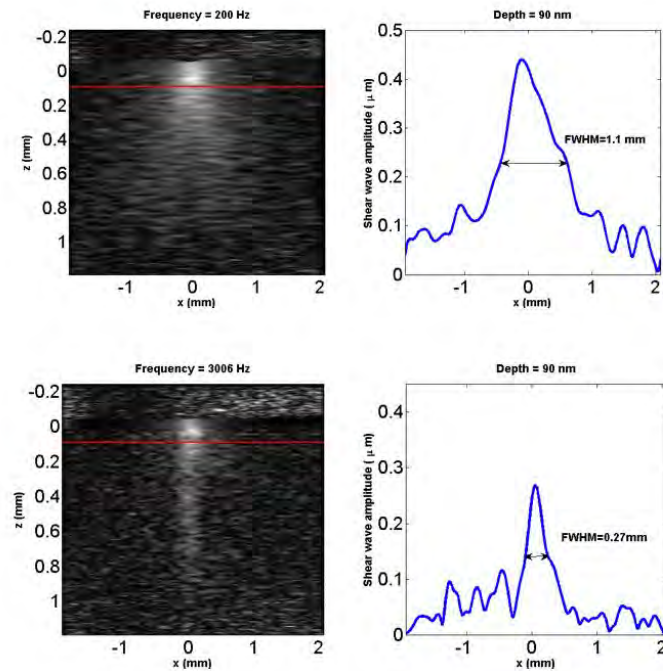


**Figure 2.16.** (left) OCE displacement maps are shown at acoustically-generated shear-wave frequencies of 200 Hz (top row) and 3000 Hz (bottom row) for an 8% (stiff, elastic) gelatin gel phantom. The top of the sample is located at depth  $z = 0$ . The brightest area (left) corresponds to the largest displacements (right) at the ultrasound focus. The mechanical interaction length, indicated by the full-width-half-maximum (FWHM) values, affects the mechanical spatial resolution.

## 2.4.1 US-OCT methodology

### US-OCT system setup

The optical source on the SD-OCT system was a 26 mW superluminescent diode (Praevium Research) with a center wavelength of 1330 nm and a bandwidth of 105 nm. The spectrometer used in our system (Bayspec, OCTS-1255-1330-1405) included a 1024-pixel InGaAs lines can camera (Goodrich, LDH2), which was connected to a PC via a NI-IMAQ board (National Instruments, NI-PCIe 1427). Optical beam steering was achieved using an x-y galvanometer (SCANLAB, SCANcube 7) controlled by the PC via a multifunctional DAQ card (National

Instruments, NI-PCIe 6353). The OCT system was operating in M-mode with the scan rate of 47 KHz. Details of the system setup can be found in Figure 2.17. This system has a low numerical aperture (NA=0.03) to image a large range of depth, resulting in a FWHM transverse resolution around 20  $\mu\text{m}$ . The axial resolution, however, was about 5  $\mu\text{m}$ .

The ultrasound transducer (ValpeyFisher, Hopkinton MA, 8 MHz, 0.75-inch diameter, F-1) was fixed from the bottom and the tissue sample was placed on a thin agarose standoff pad mounted on a 3-D movable stage. A power amplifier (3100LA, 55dB, 250 KHz – 150 MHz) drove the US transducer to transmit ultrasound amplitude-modulated bursts. Radiation force was generated at the sample-air surface where the acoustic impedance changes dramatically. This radiation force was applied along the axial ( $z$ -axis) direction where the force magnitude was proportional to the acoustic intensity over a small area at the sample surface. Real-time feedback of the tissue motion allowed us to locate the ultrasound focus precisely (see Figure 2.18(a)). This ARF was amplitude modulated at a sinusoidal frequency which generated a harmonic surface force at a specific frequency. The velocity of the surface wave was calculated by estimating the spatial-phase gradient of each shear wave over a range of transverse locations (Figure 2.18(b)). Shear-wave speed in the bulk media is approximately 1.05 times surface wave speed [111]. Dispersion (change in shear speed with frequency) measurements were fit to values predicted from rheological models to find estimate the complex modulus.

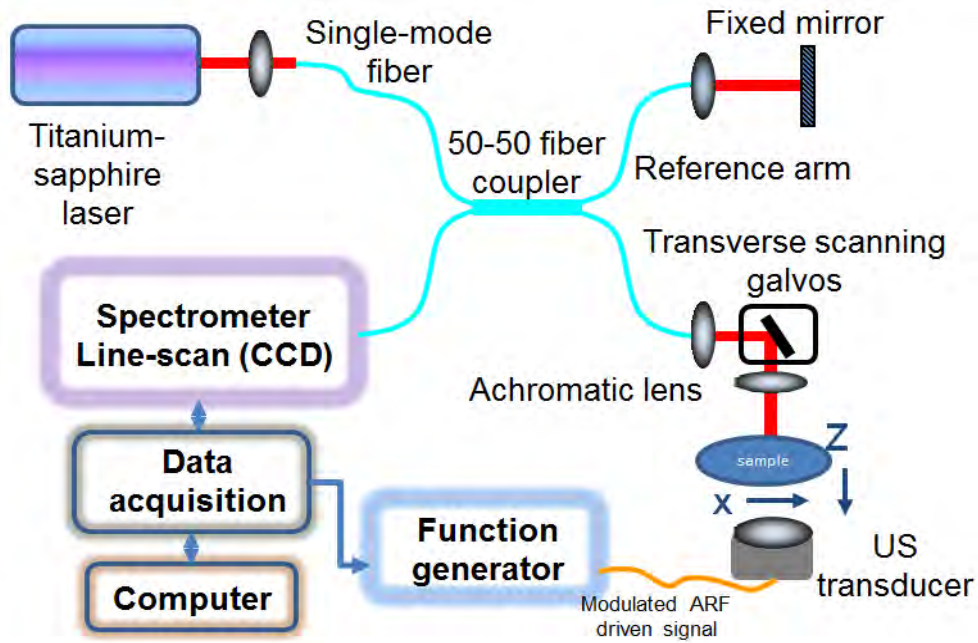


**Figure 2.17.** The schematic of the system used for mechanical testing of soft tissue samples.

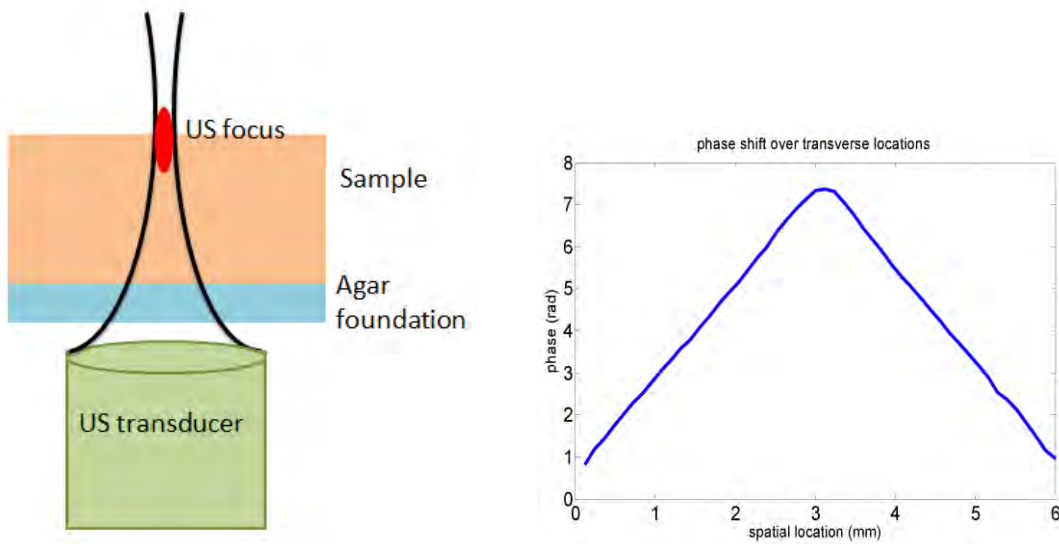


**Figure 2.18.** (left) A focused ultrasound transducer generated surface waves at the sample surface. (right) Example of the phase shift measured over transverse locations in homogeneous media. The phase gradient was calculated through linear regression applied to the phase plot.

### **Gelatin phantom tests**

Gelatin gel samples (bi-phasic hydrogels) of 4 and 8 percent concentrations were used in this study. Each cylindrical sample was 1-inch in diameter and 1 cm in thickness. Titanium dioxide particles were added to increase the optical contrast inside the gel. Details of phantom construction can be found in [5]. Three samples of each concentration were measured to test the repeatability of the technique.

The OCT scan area was 6 x 6 mm containing 50 x 50 measurement points and the drive voltage of the ultrasound transducer was 16 V and 22 V for 4% and 8% gelatin sample, respectively. Voltage accounts for different strain responses observed for the two gel concentrations. Modulation frequency ranged from 200 Hz to 4000 Hz. Above 4000 Hz, the surface wave attenuated too quickly, resulting in noisy spatial-phase-gradient measurements.

### **Porcine liver experiment**

Two liver samples were cut using a circular punch on a freshly-excised porcine liver obtained from the Meat Lab, Department of Animal Science at University of Illinois. The liver was placed in iced saline (0.9% sodium chloride) immediately after harvesting and then transported to the lab for measurement. The diameter of samples was 1-inch and the thickness was approximately 1 cm. Prepared liver samples were warmed in saline at 23 °C for one hour before mechanical testing. One liver sample was monitored during the formalin fixation process. It was measured at four time points – 0 h, 20 min, 1 h, 2 h after soaking in 10% formalin in a 50 ml tube. The sample was washed in saline before making each measurement. A control sample was kept in saline between measurements made at 0 h, 40 min, 2 h.

The OCT scan area was 4 x 4 mm containing 50 x 50 measurement points and the drive voltage of the ultrasound transducer was between 34 - 40 V, where high voltages were used as

samples stiffen during fixation. Modulation frequency ranged from 200 - 3500 Hz. Above 3500 Hz, the surface wave attenuated too quickly, resulting in noisy spatial-phase gradient measurements.

## **2.4.2 Validation results of phantom and tissue**

### **Shear modulus estimation of gelatin phantoms**

The shear-wave speeds estimated from six gelatin samples (three each at 8% and 4%) are shown in Figure 2.19. Assuming an elastic, non-dispersive medium and selecting the shear-wave speed at 300 Hz, the shear modulus was found to be  $2984.6 \pm 130.2$  Pa for 8% gelatin and  $835.8 \pm 86.5$  Pa for 4% gelatin. Acknowledging dispersion and adopting the Kelvin-Voigt viscoelastic model, the complex moduli estimated are presented in Table 2.5. Errors represent the standard deviation based on three measurements.

### **Shear modulus change of fresh liver during fixation**

Figure 2.20 and Table 2.6 present the measurements of mechanical property changes of the ex vivo liver sample during fixation in 10% formalin using ARF-OCE. Both elastic modulus and viscous modulus increased about 10 times after 2 hours fixation. Meanwhile, the control sample in saline showed little change over the 2 hour measurement time. This finding agrees with what has been found in literature [112] that the content of water, collagen, and the natural crosslinking do not change after formalin fixation, but the amount of methylene bridge (-CH<sub>2</sub>-) cross-linking increases during fixation. These crosslinks increase the elasticity of the tissue as well as the viscosity.

This study provided a new tool for studying mechanical properties of soft tissues over a broad force-frequency range. It is believed that as force frequency increases, the mechanical resolution (which is determined by the shear wavelength) also increases. Reliable measurements of shear-wave speeds up to 4000 Hz have been achieved. This could be increased further by using more focused ultrasound transducer and finer transverse sampling of the OCT scans. This technique shows great promise for investigating the force-frequency landscape of tissues and therefore providing a more complete understanding of the tissue microstructure.

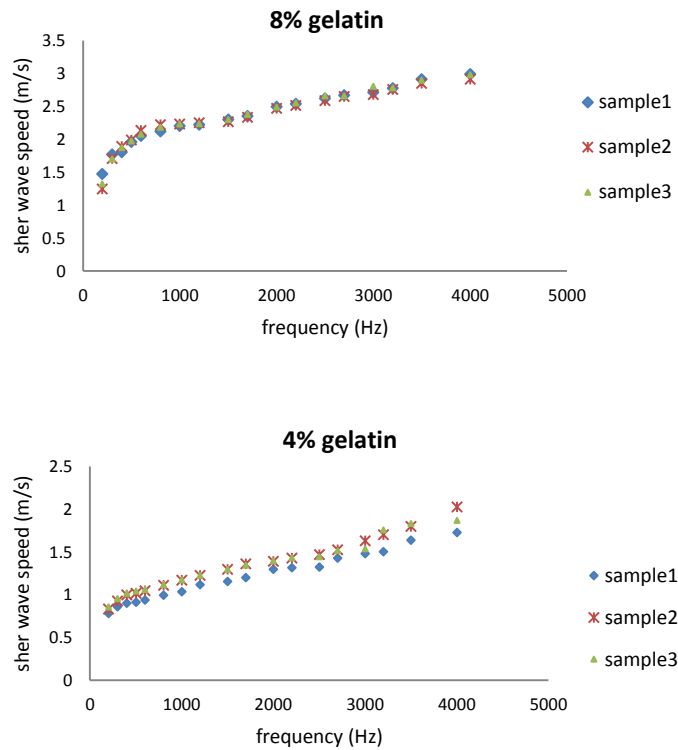


**Figure 2.19.** Shear wave dispersion curves for three 8% and 4% gelatin gel samples.

**Table 2.5.** Viscoelastic parameters estimated by Kelvin-Voigt model

Gelatin concentration	$\mu_1$ [Pa]	$\eta$ [Pa s]
4%	889.7±105	0.1±0.06
8%	3524.3±108	0.3±0.08

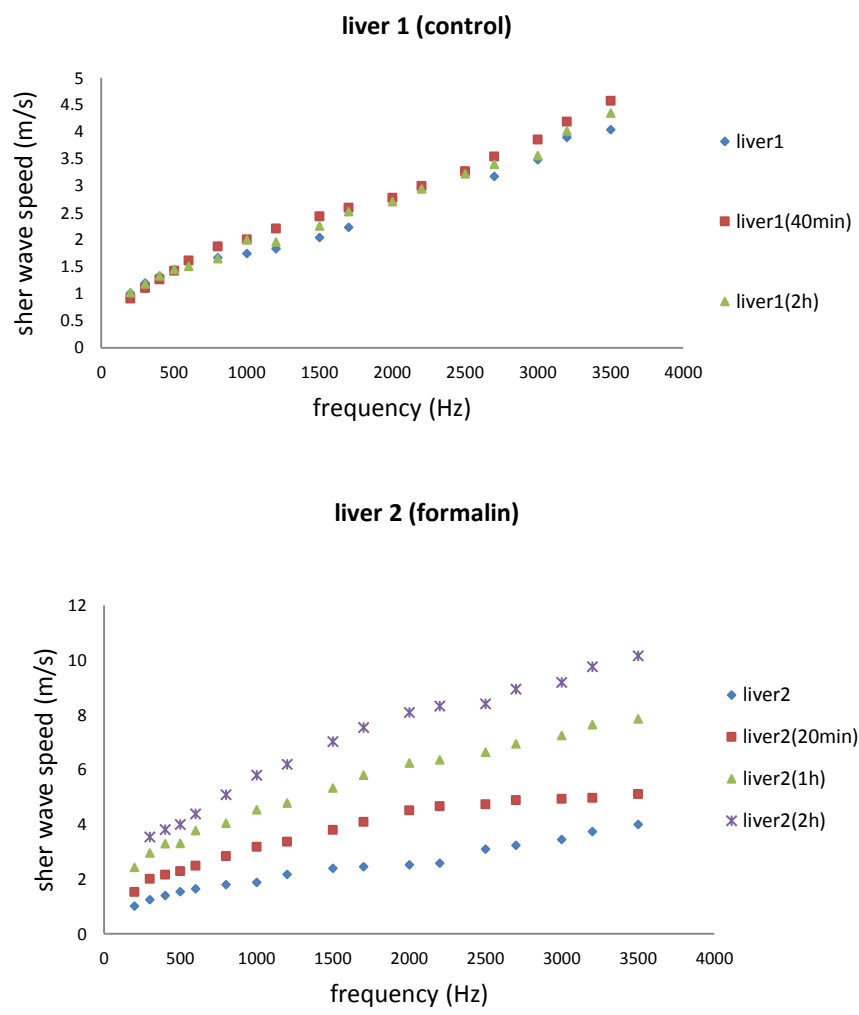


**Figure 2.20.** Shear-wave dispersion curves in a control sample at three times (top) and a liver samples in formalin at three measurement times (bottom).

**Table 2.6.** Estimation of liver viscoelastic properties during formalin fixation

Time Liver		0 min	20 min	40 min	1 h	2 h
1	$\mu_1$ [Pa]	1139.6	-	1098.2	-	1064.8
	$\eta$ [Pa s]	0.37	-	0.41	-	0.40
2	$\mu_1$ [Pa]	1150.8	3475.7	-	8214.0	12108.8
	$\eta$ [Pa s]	0.37	0.85	-	1.79	2.93

## 2.5 Summary

The quantification of viscoelastic properties is important in the understanding of the tissue microenvironment and is expected to play an important role in disease diagnosis. In this section, I summarized three techniques for measuring mechanical properties at three different scales. Indentation is widely used in mechanical characterization, and is viewed as the “gold standard”. However, indentation methods are usually not fully compatible with in vivo measurements and the contact between sample surfaces and the indent probe must be strictly controlled. Utilizing dynamic-wave elastographic techniques for estimating mechanical properties of tissue offers several advantages. Firstly, among the many methods now available for visualizing tissue viscoelastic properties, wave based techniques are valued for their ability to quantitatively map complex shear modulus  $G$ . Secondly, imaging methods can provide much higher spatial resolution than indentation, especially optical methods. The high spatial resolution would enable the study of

small biological tissues and 3D tissue cultures. Thirdly, it makes in vivo measurement of tissue material property possible during conventional imaging examinations.

The three techniques introduced in this chapter are different in mechanical excitation frequency. Indentation methods are suitable for catching mechanical behavior of less than 1 Hz. Needle excited shear waves are often within 50 and 500 Hz. The mechanical properties of tissues and polymers can be measured at force frequencies up to 4000 Hz using an ultrasonic radiation force excitation method with OCT particle motion tracking. Since different mechanical frequency ranges will render difference in the spatial resolution, field of view, displacement sensitivity, and SNR, each technique will have its own unique application areas. Moreover, measurements from different techniques are possible to emphasize different phenomena of the material which correlate with different ECM components. The combination of multiple techniques might be needed to fully understand the structure of the tissue. And applying the right model will help extract the underlining ECM properties from the measurement techniques.

## CHAPTER 3: CORRELATION OF TECHNIQUES, MODELS AND ESTIMATED MECHANICAL PROPERTY

The three techniques introduced in the previous chapter excite tissue using different mechanisms. Mechanical properties measured at different frequencies could arise from tissue structures that responding specifically to a particular force frequency. For example, fluid motion through the ECM is likely to vary with force frequency. Consequently, a description of tissue mechanical properties is more complicated than the information conveyed by modulus values. The “intrinsic” properties of tissues also depend on the measurement techniques and analysis models applied. Models that are suitable for a particular experiment could assist in converting physiological information of tissue to parametric representations. In this process, both measurement techniques and model assumptions will affect the information obtained about tissue property. This chapter will evaluate the influence of techniques and models used to the measured mechanical parameters given the same sample.

### **3.1 The consistency of all techniques on elastic material**

Among the three techniques investigated, indentation is relatively standard and widely used in material characterization field, and imaging techniques are new and promising for tissue applications. Both imaging techniques have been validated individually in Chapter 2. Each method has unique advantages and limitations. The critical questions are: which technique should be chosen, and would these techniques yield the same or different mechanical properties when testing

the same material. I attempt to answer the questions by measuring a well-understood gelatin phantom using all three techniques before applying them to tissues and viscous phantoms. For most techniques, gelatin phantom is a uniform hydrogel with incompressible linear-elastic mechanical properties when strain is less than 10% [65]. As a linear-elastic material, the elastic modulus of a gelatin gel does not significantly depend on load frequency. This material can simply be modeled as Hookean material which rules out the interference from using the inappropriate model to describe the frequency dependent responses of the material, thus allows direct comparisons of quasi-static indentation and dynamic imaging measurements.

### **3.1.1 Measurement of gelatin samples**

The general challenge is to find combinations of samples and estimation techniques that yield direct comparisons of elastic moduli from different measurement approaches. These include the effects of different sample shapes required by different techniques. My contribution is to provide a procedure for employing indentation measurements of elastic modulus that may be used to validate shear-wave imaging estimates.

#### **Phantom preparation**

The gelatin samples are constructed by mixing 250-bloom, Type-B, animal-hide gelatin powder (Rousselot Inc. Dubuque, IA) into the twice-deionized and degassed water. Gelatin powder is added to water at  $21^{\circ}\pm 1^{\circ}\text{C}$  in a glass beaker, mixed thoroughly, and placed in a heated water bath at  $70^{\circ}\pm 2^{\circ}\text{C}$  for 45 minutes. The mixture is gently stirred with a metal spoon for 1 minute after every 10 minutes of heating. The molten gelatin, now visibly clear of undissolved powder and air bubbles, is removed from the heat and allowed to cool at room temperature from  $70^{\circ}\text{C}$  to  $45^{\circ}\text{C}$ . Cornstarch (3% by weight) is added to the molten gelatin and thoroughly mixed to provide an

acoustic backscatter signal for shear-wave imaging. These particles did not significantly increase acoustic attenuation or modify the elastic modulus of the material. The gelatin suspension was then poured into one of three different-sized cylindrical containers, immediately sealed with plastic wrap, and allowed to quiescently congeal at room temperature for  $24 \pm 2$  hours. Congealing time begins when molten gelatin is poured into a container and ends at the time of mechanical testing. The molten gelatin congeals upon cooling to form denatured collagen-molecule aggregates, where half of the cross-linking that generates the elastic properties occurs in the first 24 hours [66]. However, sample preparation procedures must be precisely maintained to ensure reproducible mechanical properties. In particular, accelerated cooling of gelatin (ice bath, refrigerator) is ill advised, and chemical cross-linkers were not used. At the time of measurement, the plastic wrap was removed and samples were exposed to air or water as described below. For indentation technique and needle-based ultrasonic shear wave imaging technique, measurements were made at  $23^\circ\text{C}$  within the rigid container that surrounded all surfaces except the top. For ARF-OCE, samples were taken out of the molds and put onto the agarose standoff pad.

Three different sample sizes (big, medium, and small), each at four different concentrations of gelatin powder, were studied: 2%, 4%, 6%, and 8% gelatin by weight. Cylindrical samples labeled small, medium, and large in size based on their diameter compared to the radius of indenter. The large-size sample approached the semi-infinite geometry to serve as a baseline study, and the medium size is the size that would be used for most of the experiments. Indentation and ultrasonic technique were applied on samples of these two sizes. However, since ARF-OCE technique is not compatible with these two sizes, the small size which is often seen in tissue applications is added for optical technique. Table 3.1 lists the dimension of the three sample size used in the experiments.

**Table 3.1.** Cylindrical sample sizes in millimeters

	<b>Small</b>	<b>Medium</b>	<b>Large</b>
<b><i>D</i></b>	<b>22</b>	<b>44</b>	<b>70</b>
<b><i>H</i></b>	<b>6</b>	<b>18</b>	<b>32</b>
<b><i>D/R</i></b>	<b>8.8</b>	<b>17.6</b>	<b>28</b>
<b><i>H/R</i></b>	<b>2.4</b>	<b>7.2</b>	<b>12.6</b>

\**D* is the sample diameter, *H* is its minimum height, and  $R = 2.5$  mm is the spherical indenter radius

### **Measurement experiments**

In indentation tests, adhesions were minimized by covering the top sample surface with water and lubricating the indentation probe tip with Pol-Ease2300 (Polytek Development Corp, Easton, PA). Without adhesions, the Hertzian method for elastic modulus estimation was applicable. It was verified that minimal water absorption or sample desiccation occurs during the experiments thus did not significantly bias modulus estimates. All indentation experiments were performed using the TA.XTplus Texture Analyzer (Stable Micro Systems Ltd., Surrey, U.K.) with a 1-kg load cell (15.3 mg force resolution) and a 5-mm-diameter spherical stainless steel indenter tip (1  $\mu\text{m}$  positioning resolution). Indenter speed was set to 0.01 mm/s to implement quasi-static compressions that minimized the weak porous and viscous effects. The visual onset and cessation of sample contact corresponded with features of the force-displacement curve as described in Figure 2.1. Initial contact was used to measure the height of a sample. More details can be found in Section 2.1.

For ultrasonic shear-wave imaging tests, diagrams of the experimental setups are shown in left side of Figure 3.1. A vibrating needle positioned in the center of the sample was used to induce shear waves that were imaged using pulsed-Doppler methods. This technique was applied to medium and large-size samples. Narrow-band vibration generated radial shear waves at four different frequencies. To minimize shear wave reflections from sample boundaries and maintain sufficient wave amplitude for ultrasound detection, different vibration frequency ranges were applied to the samples having different gelatin concentrations. For 8% gelatin concentration, the applied vibration frequencies were 100, 200, 300, 400 Hz. For 4% and 6% gelatin concentrations, the frequencies were 50, 100, 200, 300 Hz, and for 2% gelatin concentration, 25, 50, 100, 150 Hz vibrations were applied. A linear-array ultrasonic transducer was set for color-Doppler acquisition with 8 MHz, 4-cycle pulses. From particle velocity estimates, shear-wave speed  $C_s$  was estimated and averaged over the sample. Detailed information about these measurements, motion detection algorithms, and modulus estimation are found in Section 2.2 and 2.3. Because gelatin is homogeneous, isotropic, incompressible, and only weakly dispersive, the shear-wave velocity  $C_s$  in the gels is approximately constant with position and needle-vibration frequency. Therefore, values of  $C_s$  at four vibration frequencies  $\omega_n$  were averaged and a single value for elastic modulus  $E$  was estimated using the equation

$$E = \frac{3}{16} \rho \left[ \sum_{n=1}^4 c_s(\omega_n) \right]^2 \quad (3.1)$$

where  $\rho$  is sample mass density assumed to be 1.02 g/cm<sup>3</sup> at 2% gelatin concentration, .04 g/cm<sup>3</sup> and 4%, 1.06 g/cm<sup>3</sup> at 6% and 1.08 g/cm<sup>3</sup> at 8%.

For optical surface-wave imaging tests, diagrams of the experimental setups are shown in the right-hand side of Figure 3.1. Optical coherence elastography (OCE) technique is applied to the small size samples. A single-element ultrasonic transducer applied a narrow-band acoustic radiation force to the top sample surface from below, while a paraxial OCT system scanned the sample from above to image shear-wave surface movements.<sup>2</sup> The large impedance difference at the air-sample interface generates an oscillating mechanical force at the sample surface. Ultrasonic and OCT-based estimates of  $C_s$  (and elastic modulus) were found to be equivalent once small differences between surface and bulk shear waves are compensated [91]. The greater motion sensitivity of OCE allowed us to reduce the applied vibration amplitude, which reduced but did not eliminate the reflected shear waves in the 8%-gelatin samples.

For OCE measurements only, small-size gelatin samples were extracted from their rigid molds and placed atop a stiff 4% agar-gel pad that coupled samples to the transducer applying the acoustic force. 10 MHz compressional-wave bursts with a sinusoidal amplitude modulation applied a 200 Hz acoustic radiation force to the sample-air top surface. As acoustic force was applied, the OCT system scanned that surface to image shear waves at a 1 mm depth.

---

<sup>2</sup> OCE measures Rayleigh waves at the sample surface that are about 5% slower than shear waves generated in the volume using needle vibration [113, 115]. Rayleigh wave speed was adjusted according to  $c_s = 1.05c_R$  to estimate elastic modulus values [91]. Also the 200 Hz radiation force used for these elastic materials minimized the bias that could have occurred from the Lamb waves generated in samples behaving as layered materials [114].

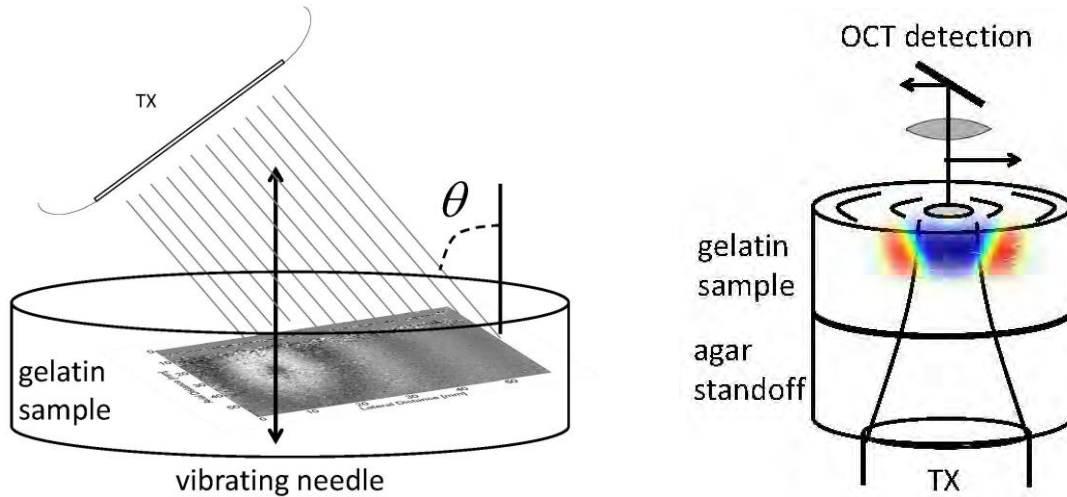


**Figure 3.1.** The ultrasonic (left) and OCT (right) shear-wave imaging experiments are illustrated. TX identifies the ultrasonic transducers for each experiment and  $\theta$  is the Doppler angle between the beam and particle motion. On the left, the central vertical axis of the sample is the location of the vibrating needle generating shear waves. On the right, the central top surface coincides with the fixed beam focus. The gray-scale and color wave patterns are from actual measurements although the sizes are not to scale.

## Results

Gelatin gels exhibit isotropic elastic properties. In principle, the Young's modulus estimated by indentation should be equal to that estimated using dynamic wave imaging techniques, although each measurement technique can bias modulus estimates differently depending on how it couples to sample boundaries. Sample boundaries that are strongly coupled to the measurement stimulus yield biased elastic modulus estimates. However, if the same estimates are obtained consistently for a sample concentration, we assumed any measurement artifacts are negligible.

Figure 3.2 shows the comparison between Young's modulus measured by indentation technique (Hertzian contact model) and needle-based ultrasonic shear wave imaging on large size samples. As shown in the figure, the measured Young's moduli are the same for both methods (p-value for one-way ANOVA test is less than 0.05). Also, no significant differences were found for

indentation measurements made on gelatin samples with and without cornstarch particles (results not shown). This result suggests that 1) Young's modulus estimates provides a measurement-independent property for gelatin material; 2) the models applied to each technique are suitable for the technique; 3) the large size is truly semi-infinite for both techniques and boundary interactions do not bias estimates within the modulus range of 300 Pa to 9000 Pa.

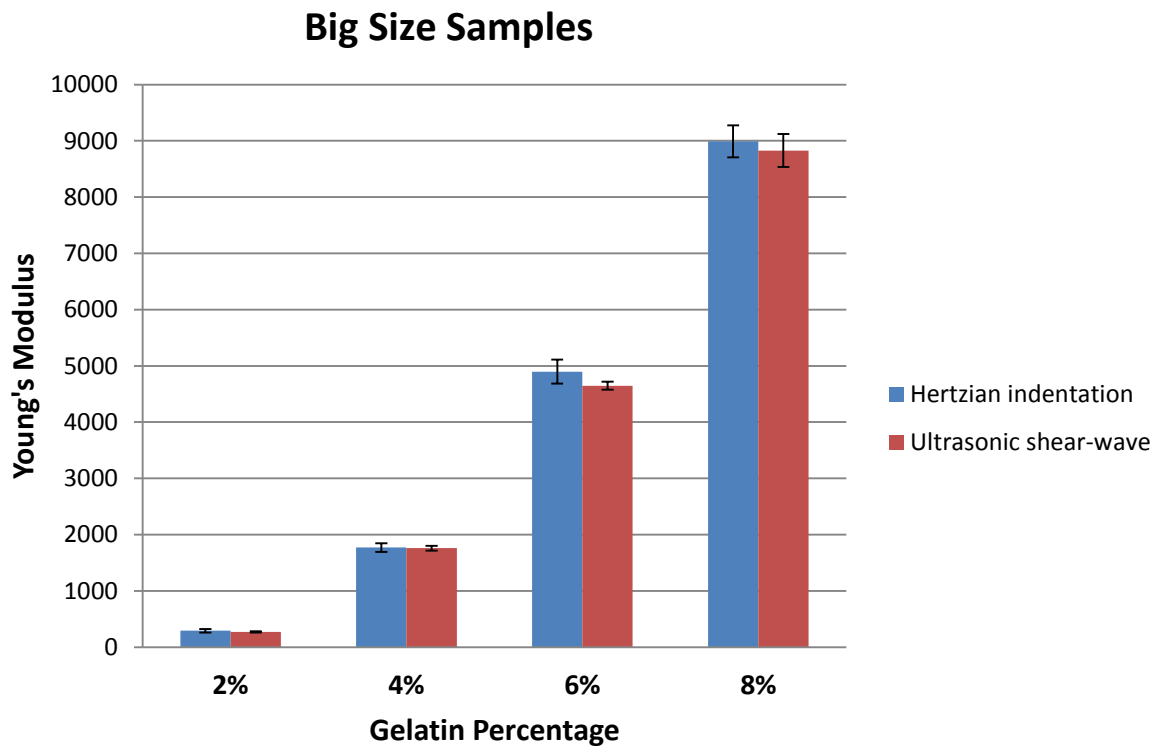


**Figure 3.2.** Comparison of the measurement results of Young's modulus between Hertzian contact model-based indentation technique and needle-based ultrasonic shear wave imaging on BIG size samples. Error bars represent the standard deviation of measurements from three samples made from the same gelatin batch.

Figure 3.3 provides results measured from the medium size samples for both indentation and ultrasonic shear wave imaging. Since the large size sample is already confirmed to have the

correct modulus measurement, it is listed as a reference in Figure 3.3. As seen in the figure, indentation tests yield the same measurement values as the reference values, which means boundary influence is negligible for medium size material whose modulus is ranged from 300 Pa to 9000 Pa. For shear wave estimates, lower percentage measurements do not deviate from the reference values. However, sample with gelatin percentages greater than 5% indicates a measurement bias for limited sample size relative to the measurements of large-sample of the same material. Modulus estimated in medium size samples with 8% gelatin is significantly different ( $\alpha=0.05$ ) from the reference values. Because the shear-wave wavelength in 8% gelatin is much larger than the other percentages, shear-wave reflections in the 8% material are much stronger, which violates the semi-infinite assumption in deriving Equation 3.1. In summary, for medium size samples, the semi-infinite assumption is still valid for the indentation technique, while the ultrasonic shear wave imaging technique begins to experience the boundary influence at the high stiffness end.

## Medium Size Samples

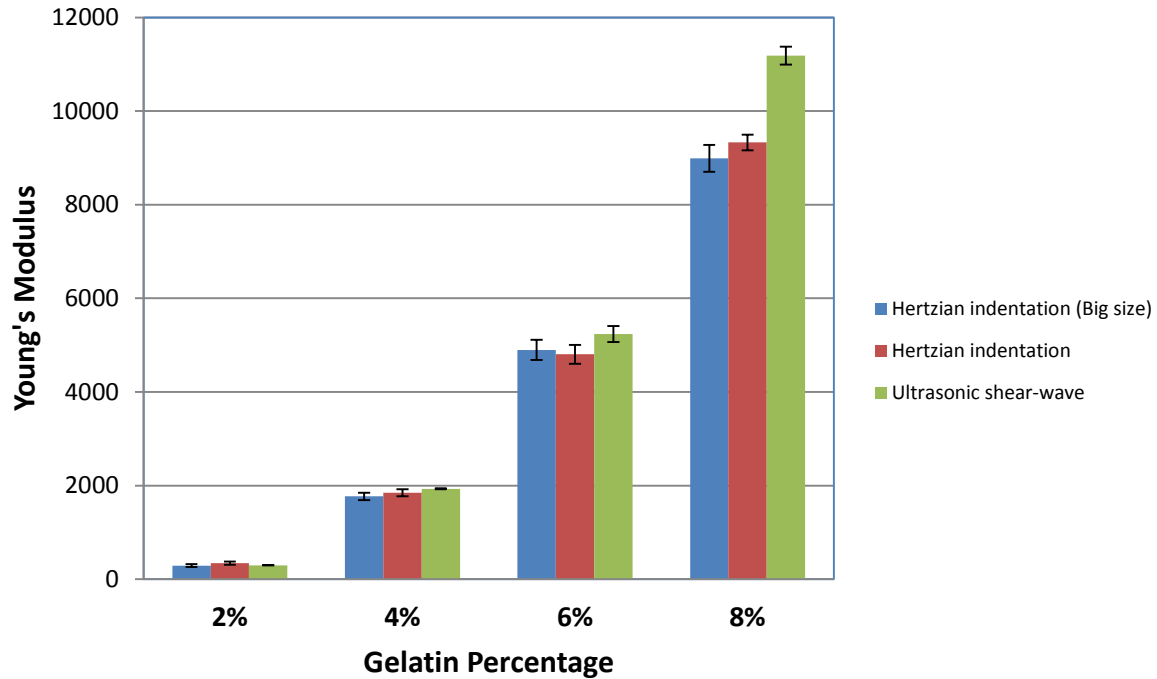


**Figure 3.3.** Comparison of the measurement results of Young's modulus measured from Hertzian contact model-based indentation technique and needle-based ultrasonic shear wave imaging on MEDIUM size samples. Blue bars are a reference value from the BIG size sample measurement. Error bars represent the standard deviation of measurements from three samples made from the same gelatin batch.

Figure 3.4 provides results measured from the small size samples for both indentation and ARF-OCE surface wave imaging. Again, the reference point is shown in the figure. The figure shows that both indentation and dynamic wave imaging techniques are biased high to some extent. This is caused by two reasons. Firstly, the side and bottom boundaries will distort the stress-strain field, and thus violating the model assumptions. Secondly, the elastic modulus of gelatin is highly dependent on its thermal history. In small size samples, the temperature cools down much faster during congealing and the de-moisturization at the surface is more severe, therefore it is possible that the phantom is indeed a little stiffer.

## Small Size Samples

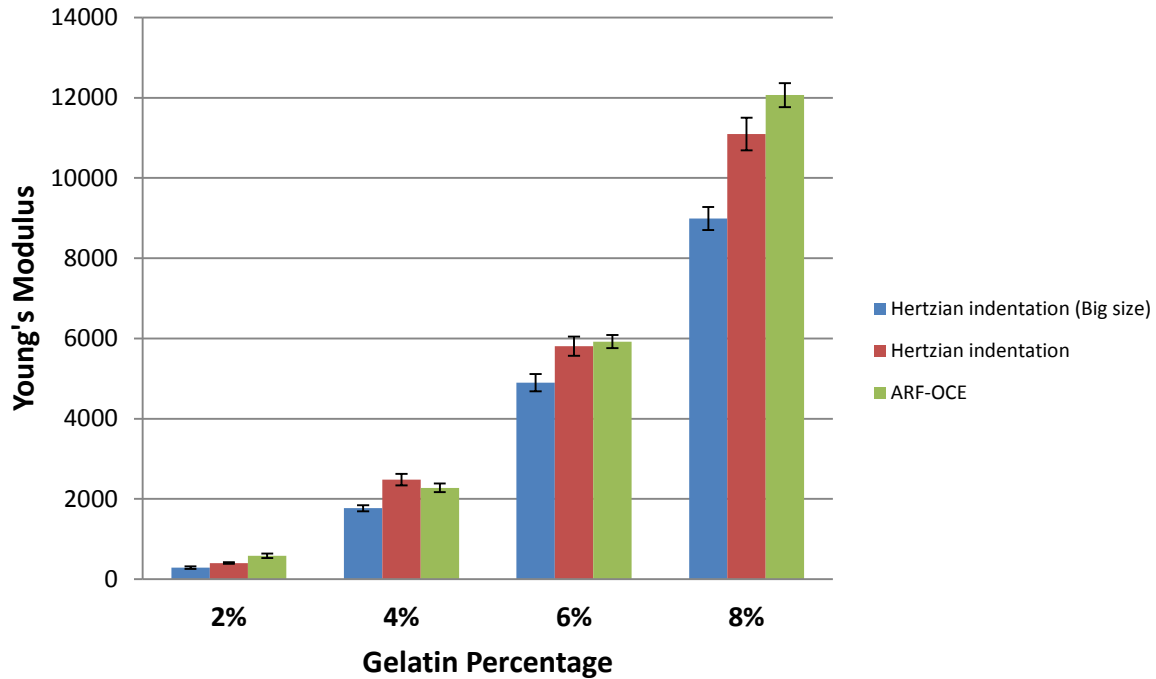


**Figure 3.4.** Comparison of the measurement results of Young's modulus measured from Hertzian contact model-based indentation technique and ARF-OCE surface wave imaging on SMALL size samples. Blue bars are a reference value from the BIG size sample measurement. Error bars represent the standard deviation of measurements from three samples made from the same gelatin batch.

### 3.1.2 Boundary-effect simulations and solutions

As shown in Section 3.1.1, both quasi-static and dynamic techniques suffer from the limitation of sample size, and different techniques interact with the boundary differently and therefore the amount of bias (for fixed sample geometry) depends on the material stiffness and the measurement technique. The rule of thumb for indentation is that the radius of the indenter should be less than 10 times the diameter and the height of a cylindrical sample. The rule of thumb for shear wave imaging is that sample dimensions be larger than 2 shear wavelengths at the smallest frequency [92]. Both are met in the large sample scenarios. However, in real applications, it is difficult to control the size and boundary of the material. Therefore, new models or post-processing

methods must be proposed for limited boundary conditions in order to achieve bias-free modulus estimates.

### Correction method for indentation

Stress-field from FEM simulation shows that in the small size samples, the bottom boundary is more likely to interact with the stress field during indentation (Figure 3.5). And the influence from boundary distortion effect increases with the increased stiffness of the material. This challenges the correctness of using standard Hertzian contact models for mechanical measurements in small-size samples of soft biphasic materials [116, 117, 118]. Dimitriadis et al. applied a correction to the Hertzian contact model in order to estimate the Young's modulus from force-displacement curves in thin-layer samples [118]. They derived Green's function for an infinite thickness sample bounded to the substrate and used that to compute the approximate indentation. The new model for material with a finite thickness is given by

$$F = \frac{4E}{3(1-\nu^2)} R^{1/2} \delta^{3/2} \left[ 1 - \frac{2\alpha_0}{\pi} \chi + \frac{4\alpha_0}{\pi^2} \chi^2 - \frac{8}{\pi^3} \left( \alpha_0^3 + \frac{4\pi^2}{15} \beta_0 \right) \chi^3 + \frac{16\alpha_0}{\pi^4} \left( \alpha_0^3 + \frac{3\pi^2}{5} \beta_0 \right) \chi^4 \right] \quad (3.2)$$

where  $R$  and  $\delta$  are the same as Hertzian theory,  $h$  is the sample thickness,  $\chi = \sqrt{R \delta/h}$ , and constant  $\alpha_0$  and  $\beta_0$  are functions of the material Poisson's ratio  $\nu$ . Parameters  $\alpha_0$  and  $\beta_0$  depend on  $\nu$ , and when the sample is not bound to the substrate, they are given by  $\alpha_0 = -0.347 \frac{3-2\nu}{1-\nu}$ ,  $\beta_0 = 0.056 \frac{5-2\nu}{1-\nu}$ . When the sample is bound to substrate, they are given by  $\alpha_0 = -\frac{1.2876-1.4678\nu+1.3442\nu^2}{1-\nu}$ ,  $\beta_0 = \frac{0.6387-1.0277\nu+1.5164\nu^2}{1-\nu}$ .

It is clear that the term outside of the bracket is the Hertzian solution for indentation on semi-infinite surfaces. Inside is the correction that accounts for the thickness reduction. It converges to 1 as the thickness of the sample becomes larger and approaches semi-infinite space. This correction is valid for all ranges of force  $F$ , the indenter radius, and sample thicknesses.

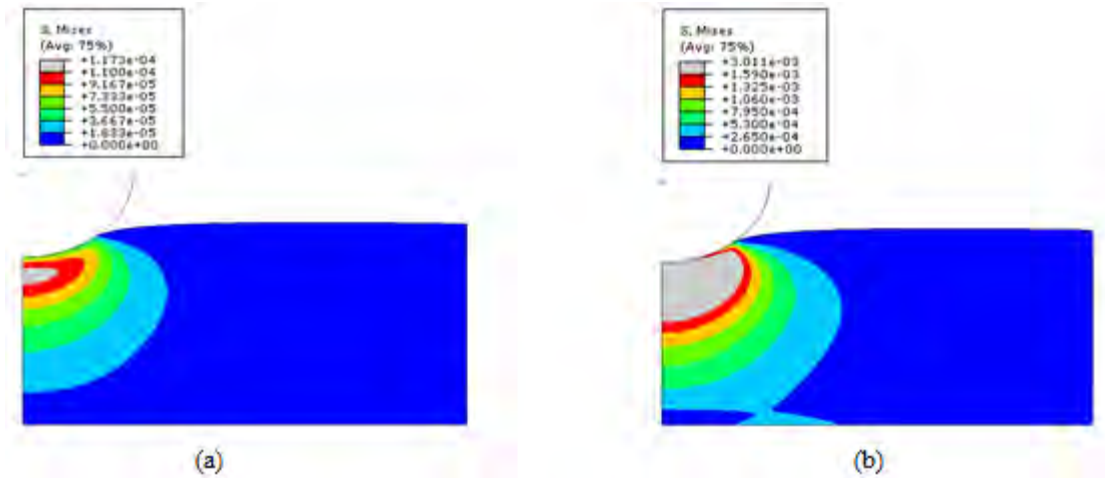


**Figure 3.5.** (a) Finite-element simulation of stress fields during maximum indentation of 2% gelatin gels for the small sample size. (b) The same simulation was repeated for 8% gelatin. The nonzero stress extends deeper into the stiff 8% gel to interact with the lower boundary, thus appearing to stiffen the sample. [68]

Data were re-processed using the Dimitriadis model instead of the Hertzian model for the small size samples for indentation. As shown in Figure 3.6, once the correction for thickness has been made, the biases on Young's modulus estimates are removed. Some deviations might still exist because the surface of small size samples is not perfectly flat, but has a concave shape (meniscus).

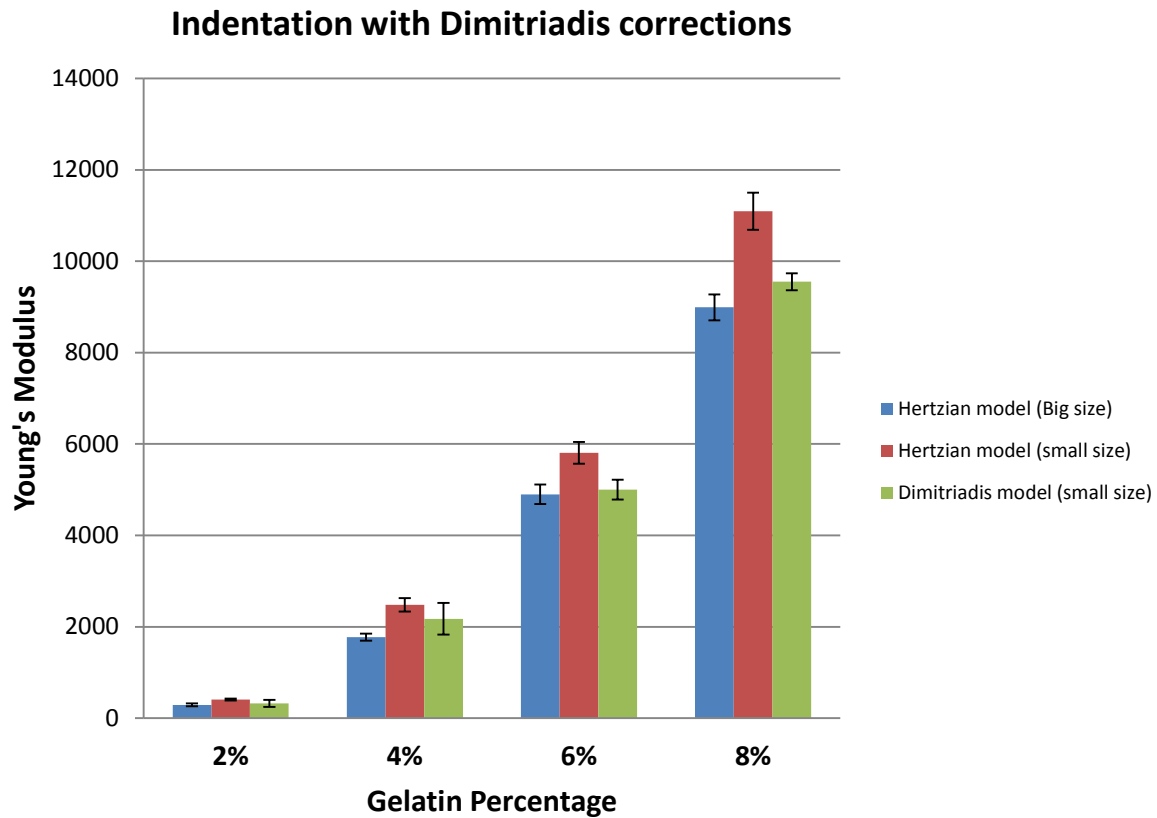


**Figure 3.6.** Comparison of the measurement results of Young's modulus measured from Hertzian contact model-based indentation technique and Dimitriadis model in small size sample. Results from big size samples are plotted as a reference.

### Correction method for ultrasonic shear wave imaging

The parameter reduction from wave propagation assumes a homogeneous continuum of semi-infinite extent. Sample heterogeneity or boundaries generate reflected waves and spatially-varying wave speeds that distort the linear-phase assumption and hence bias estimates of the complex shear modulus. Because shear waves are highly attenuated at frequencies above 1 kHz, reflections in a finite lesion are of concern primarily at frequencies below 1 kHz where the measurements are made. Wave reflections and the related artifacts of shear-speed are easy to detect because, when they occur, the gradient of temporal shear-wave phase (Figure 3.7) is not constant.

The question addressed in this section is how much measurement bias is generated in the presence of a reflected wave, and how the effect from the wave reflection can be minimized if it is unavoidable.

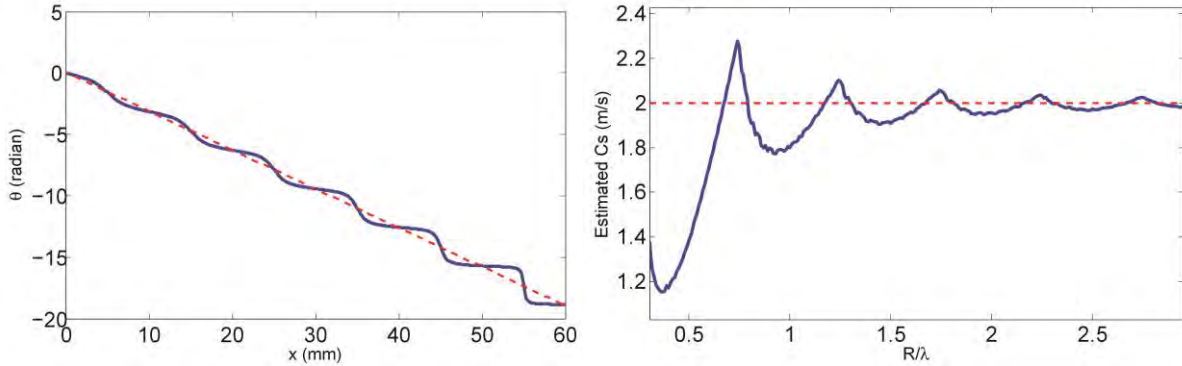


**Figure 3.7.** Simulation of wave reflection in a material that has  $\lambda = 2$  cm and  $\alpha = 0.5$  cm $^{-1}$  (the attenuation coefficient in tissue is around 0.8~2 cm $^{-1}$  [119]). The left plot shows how shear-wave phase,  $\theta(x)$ , varies as a function of radial distance from a source  $\omega/2\pi = 100$  Hz) placed at  $x = 0$ . There is a strong reflector located at  $x = R = 60$  mm from the source. The blue line is  $\theta(x)$  in the presence of reflected waves and the red line ( $\theta = -2\pi x/\lambda$ ) is the phase without reflections. Shear wave speed  $C_s(\omega)$  is estimated from the slope of  $\theta(x)$  over  $0 \leq x \leq R$ . The plot on the right shows how shear-wave speed estimates vary as the distance between the source and reflecting boundary increases.  $R$  is normalized by the shear wavelength  $\lambda$ .

Let  $w_i$  be an incident plane wave of unit amplitude traveling to the left direction. Then  $w_r$  is a reflected wave of amplitude  $0 < A < 1$  from a boundary located at  $x = R$  that is traveling to the right direction. At radial temporal  $\omega$  and spatial  $k$  frequencies,

$$w_i(x, t) = e^{-\alpha x} \cos(t - kx) \quad (3.3)$$

$$w_r(x, t) = A e^{-\alpha(R-x)} \cos(\omega t + kx + \phi) \quad (3.4)$$

where  $A = A_0 e^{-\alpha R}$ ,  $A_0$  and  $\phi$  are reflection coefficients, and  $k = 2\pi/\lambda$ , is the wave number at shear wavelength  $\lambda$ . Assuming  $w_i$  is reflected only once before it dissipates, the net wave in steady state is the sum,

$$w = w_i + w_r = \cos(\omega t + \frac{\phi}{2} + \theta(x)) \quad (3.5)$$

where the spatial phase is  $\theta(x) = \arctan\left(\frac{1-A_0 e^{-2\alpha R(1-\frac{x}{R})}}{1+A_0 e^{-2\alpha R(1-\frac{x}{R})}}\right)\tan(-kx - \phi/2)$  and  $0 \leq \frac{x}{R}, A_0 \leq 1$ .

When  $A_0 = 0$ , there is no reflection from the boundary. Therefore  $w = w_i$ , and phase is a linear function of position from the source:  $\theta(x) = -kx - \phi/2$  and  $\frac{d\theta}{dx} = -\omega/C_s$ . At the other extreme, when  $A_0 = 1$  and  $\alpha = 0$ , then  $\theta(x) = 0$  and a standing wave is generated.

In Equation 3.5, it is proved that the spatial phase shift is distorted by the reflected wave  $w_r$ . To further study the relationship of the measured modulus and the true modulus in the presence of reflected waves in arbitrary geometry, a numerical simulator is employed to generate shear wave data so the phase bias resulting from reflections can be measured. In one situation, the finite-difference time-domain (FDTD) solver [98] was used to simulate 1-D shear waves that propagate in time along the x-axis, while measuring the z-axis component of particle velocity along x. The simulated medium was a homogeneous viscoelastic solid with elastic modulus  $\mu = 4$  kPa and viscous coefficient  $\eta = 4.5$  Pa s. A source, located at the origin, vibrated harmonically at either 150 Hz or 250 Hz. Shear waves were computed numerically at all values of x every  $\Delta t = 6 \mu s$  during a 0.3 s experiment time, then down-sampled in time as needed to match data acquired during experiments. The phase-gradient method described above is applied to estimate shear-wave speed. In each plot below, the vibration plane source is at the origin and there is a perfectly reflecting boundary located at  $x = R$ .

In the second situation, the FDTD solver was reconfigured to generate 3-D cylindrical waves from a needle-like source vibrating at 150 Hz and placed in the center of a cylindrical sample. Boundaries are set to be fixed boundary conditions with a very stiff material with several hundred mega Pascal. Shear waves radiating from the linear source were reflected at the side

boundaries. The medium inside the numerical sample was homogeneous and similar to 4% gelatin with elastic modulus coefficient  $\mu = 700$  Pa and viscous coefficient  $\eta = 0.1$  Pa s. All other simulation parameters were the same as the 1-D FDTD simulations. Figure 3.8 shows the distortion of wave field at a single time point in the simulation.

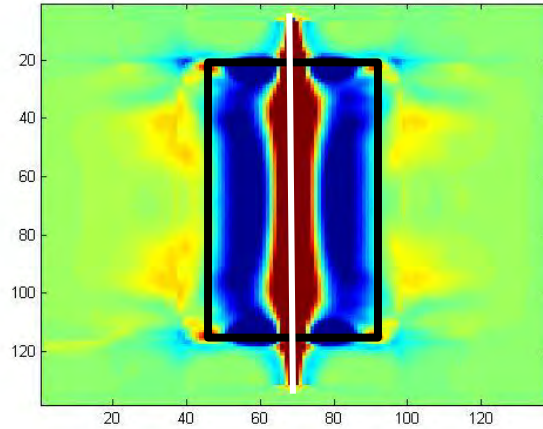


**Figure 3.8.** A cross-section of 3-D FDTD simulation of shear wave propagation in cylindrical sample. The black rectangular demonstrates the sample boundaries. The white line in the center represents the vibrating needle. Axis ticks are labeled in pixels with each pixel equals to 0.5mm.

Simulation results show that wave reflections generate stair-step patterns in the phase as a function of distance from the source (top row of Figure 3.9). Depending on the lateral extent to which phase data are used to calculate a slope for shear-wave speed estimation, Figure 3.9 shows there are different amounts of bias introduced. For example, computing the phase gradient over 40 mm of phase measurements using 1-D wave simulations results in very little measurement error compared with estimates taken over 4 mm of data. Notice for the 1-D data (bottom row of Figure 3.9) that the bias error within an 18-mm-radius sphere is larger than it is in a 44-mm-diameter sphere. Reflected-wave attenuation increases as the sphere diameter increases. The results of the data analysis applied to these 3-D wave-simulation data are summarized in Table 3.2. Since only

one frequency was simulated, an elastic medium is assumed when estimating the modulus values shown.

Finally, gelatin phantoms are constructed to verify experimentally the simulation results. Gelatin hydrogel cylinders were constructed using 8% gelatin with different diameters. Shear-wave speeds measured at 150 Hz were examined for all gelatin phantoms. A needle was inserted along the long axis of the cylinder and vibrated while shear waves were measured using Doppler ultrasound. The results of ultrasound measurements in gelatin phantoms is shown in Table 3.3, where the vibration source was located along the long axis of the gelatin phantom while shear waves radiating along the axis normal to the vibration.

Measurements based on 3-D simulations and phantom experiments both show that reflections generated in the sample with the smallest size produced the largest biases in shear-wave speed measurements. As the inclusion size increases, the modulus bias became less than 10% provided the inclusion diameter was greater than two shear wavelengths. These findings provide some guidance on estimating measurement bias for different size inclusions or lesions based on the shear wavelength. Of course, by increasing the vibration frequency, the shear wavelength decreases and the attenuation coefficient increases, and thus the bias is reduced while the random errors will be increasing as the echo SNR falls. Also using pulsed stimulation rather than harmonic-force stimulation reduces reflections at the cost of reduced SNR for particle velocity estimates. There are several factors that need to be considered in assessing measurement errors.

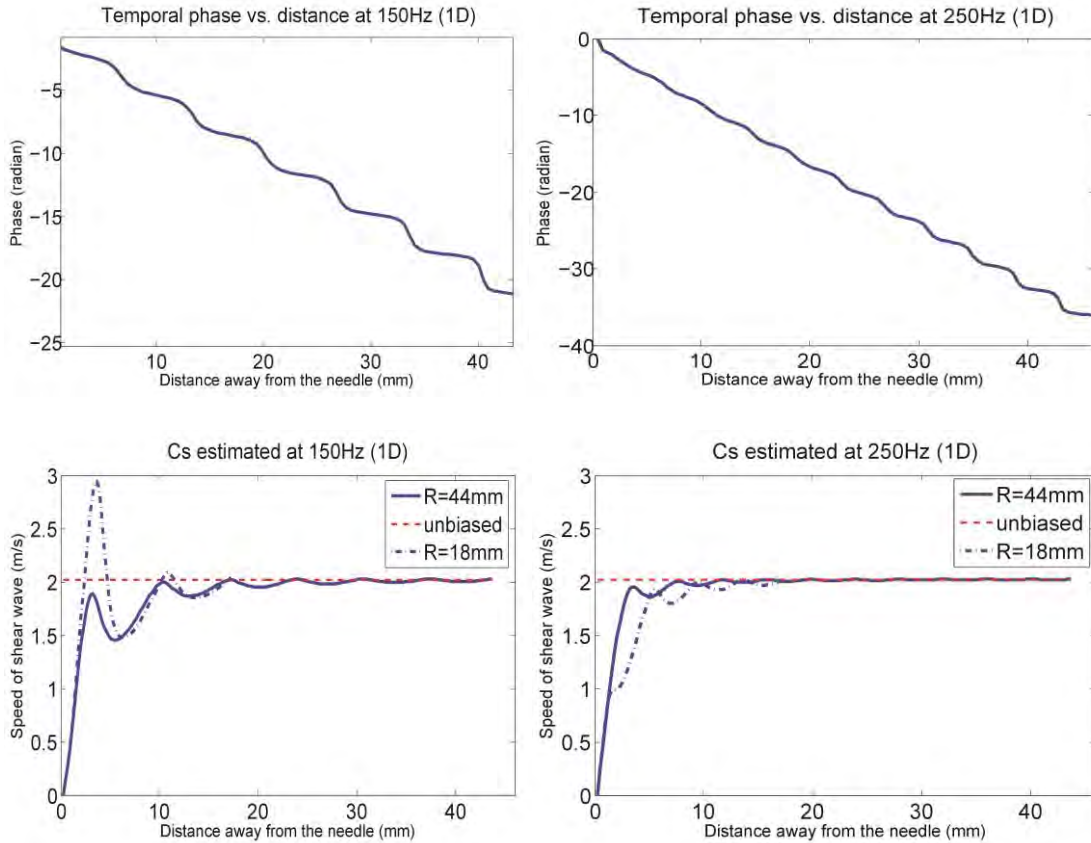


**Figure 3.9.** Numerical simulations of shear-wave spatial phases in the presence of reflections and  $C_s$  measurements. Plots in the top row are shear-wave phase simulated as a function of distance from a vibrating source. There is a reflector positioned at  $R$  mm from the source placed at the origin for the 1-D wave geometry where  $R=18$  mm and 44 mm. In the bottom row, estimates of shear-wave speed are plotted as a function of source-reflector distance.  $R = 18$  mm in the dotted lines and  $R = 44$  mm in the solid lines. Each value in a wave-speed plot is found by applying linear regression to phase data from the origin up to the corresponding abscissa value shown. Plot columns from left to right are the 1-D FDTD simulation at 150 Hz and at 250 Hz. The dotted red lines in the sound-speed plots represent the shear-wave speed input to the simulation. In all situations, speed estimates obtained from the simulated wave data converge to the values input to the simulator.

**Table 3.2.** The bias of estimates for numerical samples with different diameters (at 50 Hz)

Radius (mm)	Number of wavelength	$C_s$ (m/s) before filter	$\mu$ (Pa) before filter	Bias of $\mu$	$C_s$ (m/s) after filter	$\mu$ (Pa) after filter	Bias of $\mu$
$\infty$	$\infty$	0.837	700.569	0.081%	0.834	695.556	-0.63%
45	3	0.901	811.801	15.97%	0.842	708.964	1.28%
30	1.88	0.998	996.004	42.28%	0.834	695.556	-0.63%
27	1.35	0.945	893.025	27.57%	0.844	712.336	1.76%
25	1.35	1.277	1630.729	132.9%	0.831	690.561	-1.34%
21	1.35	1.1651	1357.45801	93.9%	0.817	667.489	-4.64%
18	0.9	1.294	1674.436	139.2%	0.761	579.121	-17.2%

**Table 3.3.** The bias of estimates for 8% gelatin samples with different diameters (at 150 Hz)

Radius (mm)	Number of wavelength	$C_s$ (m/s) before filter	$\mu$ (Pa) before filter	Bias of $\mu$	$C_s$ (m/s) after filter	$\mu$ (Pa) after filter	Bias of $\mu$
74.8	7	1.61	2592.1	0%	1.61	2592.1	0%
31.3	2.93	1.61	2592.1	0%	1.61	2592.1	0%
20.2	1.88	1.46	2131.6	17.77%	1.6	2560	-1.23%
12.7	1.18	1.38	1904.4	26.53%	1.59	2528.1	-2.46%
15.7	1.46	1.26	1587.6	38.75%	1.62	2560	1.24%
10.5	0.98	1.01	1020.1	61.42%	1.55	2402.5	-7.31%

If harmonic shear wave imaging is applied when the sample size is less than two wavelengths of the shear wave, reflected waves from boundaries can be removed by applying directional filters under some circumstances [120]. The superposition of the incident wave that propagates to the right and the reflected wave that propagates to the left (attenuation is omitted) are given by

$$w(x, t) = w_i(x, t) + w_r(x, t) = \cos(kx - \omega t) + A \cos(kx + \omega t + \phi) \quad (3.6)$$

The wave  $w(x, t)$  in complex plan can be expressed as

$$w(x, t) = \frac{1}{2} (e^{i(kx - \omega t)} + e^{i(\omega t - kx)} + A e^{i\phi} e^{i(\omega t + kx)} + A e^{-i\phi} e^{i(-\omega t - ikx)}) \quad (3.7)$$

Hilbert transformation of  $w(x, t)$  will eliminate conjugate exponents,

$$\text{Hilbert}[w(x, t)] = \frac{1}{2}(e^{i(kx-\omega t)} + Ae^{i\phi}e^{i(\omega t+kx)}) \quad (3.8)$$

where the first term represents the incident wave and the second term represents the reflected wave. Spatial-temporal filters can be applied in frequency domain to eliminate the waves propagating in specific directions. The filtering is performed in the frequency domain (Figure 3.10). Since the filtering is a linear operation, the model used to estimate the modulus is still valid.

Figure 3.11 further examines the applicability of the directional filter in materials that have spatially changing mechanical properties (using 3-D FDTD simulation). As seen in the left image, due to the inhomogeneity of the mechanical property, the wave number  $k$  has more than one peak in frequency domain. The same directional filter was applied to the corrupted waves, and the pre-defined spatial variation of shear wave speed was perfectly recovered.

Gelatin phantoms were made to verify the applicability of directional filter in real applications. A frequency range between 30 Hz to 100 Hz is tested, as higher frequencies will not have significant boundary reflections. Because gelatin is almost elastic, the shear wave speeds measured in this frequency range should not be dispersive. In Figure 3.12, blue dots represent the measured shear wave speeds, and the red dots represent those after the directional filter was applied. The benefit of directional filter correction is obvious. However, the two lowest frequencies, 30 Hz and 35 Hz, still have some bias assuming the shear wave speeds do not change with frequency. This might be due to the interference of second and third reflections from the side as well as from the top and bottom of the sample. The directional filter was applied to the simulation data and the gelatin phantom data with various diameters. The corrections to shear wave speed estimations are appended to Table 3.2 and Table 3.3. The true values for shear wave speed are restored successfully using directional filter, as long as the size of the phantom is larger than 1 wavelength.

For samples that are smaller than 1 wavelength in dimension, multiple reflected waves could be present. Wave fields in 3D must be obtained in order to filter out those reflected waves from different directions.

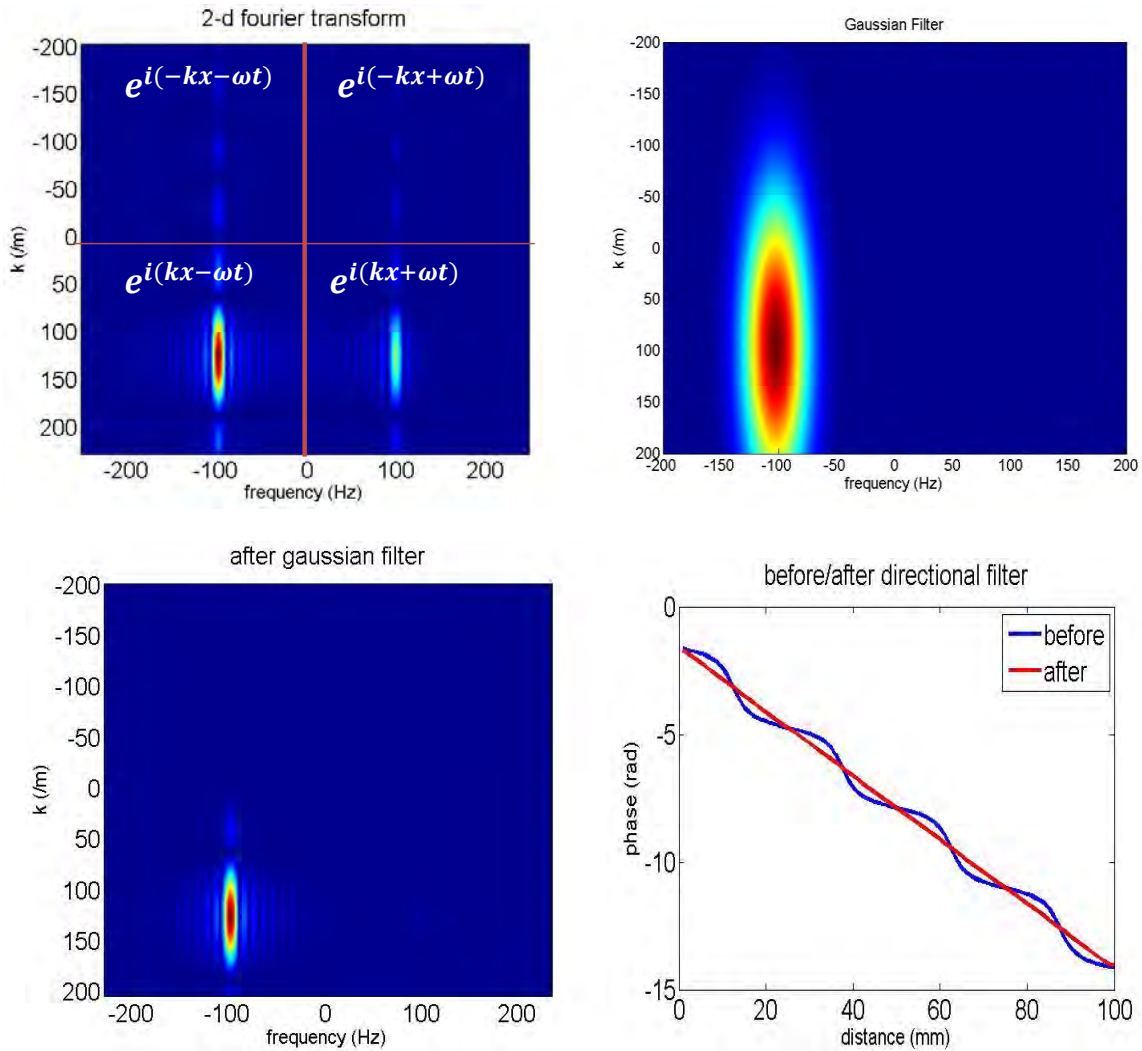


**Figure 3.10.** Directional filter of homogeneous sample. This set of pictures shows the mechanism of directional filter. In the left, top figure, the complex wave field is transformed into spatial-temporal domain using 2D Fourier Transformation. The amplitude of the reflected wave is about 15%~20% of the incident wave. The top, right figure is the 2D Gaussian filter that is applied to remove the reflected waves, which results in the bottom, left spectrum. The new wave field after filtering has a linear phase as expected. The bottom, right figure show the comparison of shear wave phase shift before and after the directional filter is applied.

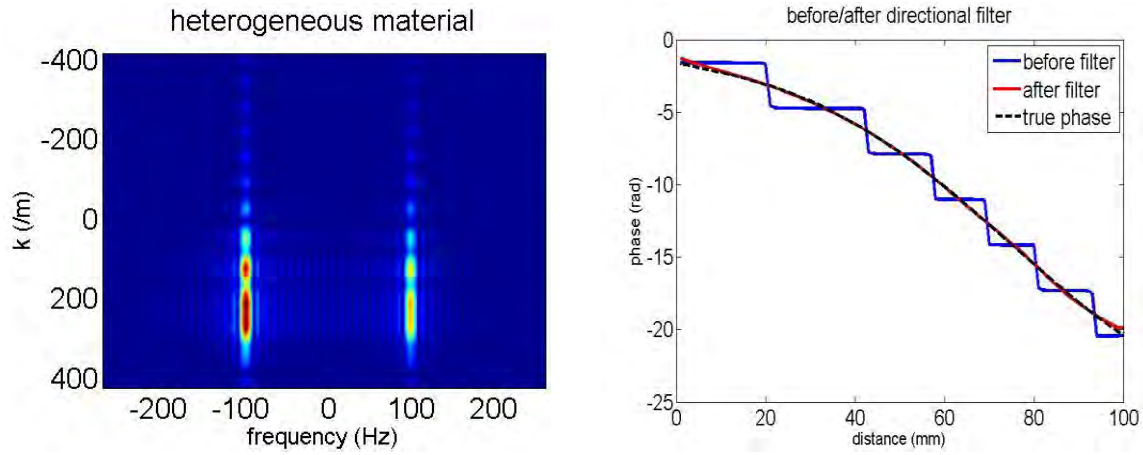


**Figure 3.11.** Application of directional filter to inhomogeneous samples. Image on the left shows the 2D spectrum of the complex wave field. Image on the right shows the correction of shear-wave phase shift.

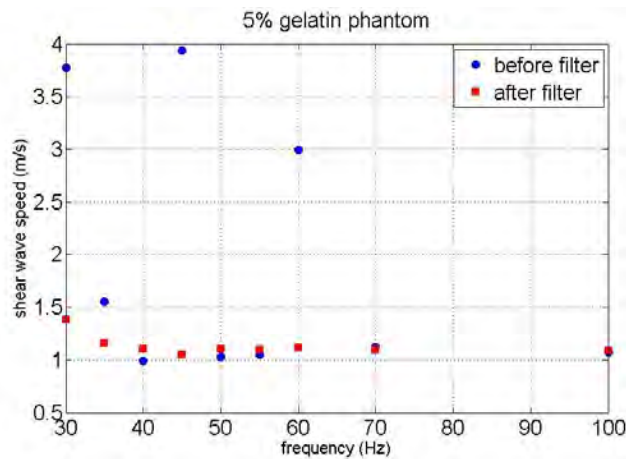


**Figure 3.12.** Application of directional filter in gelatin phantom. The excitation was at a very low frequency. Cylindrical sample was made from 5% gelatin with the diameter of 44 mm ( $R = 22$  mm). Needle-based ultrasonic imaging method was used to obtain the shear wave speeds.

The directional filter was proven to eliminate the reflected waves that propagate in the opposite direction. It could be used when the size of the sample is limited, or the sample has an internal inclusion which also generates reflected waves. Figure 3.3 shows that 8% gelatin sample with medium size yields different Young's modulus values when using indentation and shear waves techniques. This bias comes from boundary reflections and can be corrected using a

directional filter, as shown in Table 3.4. Once the correction of geometry has been made, the Young's modulus values estimated by indentation and shear wave are statistically identical. Both Figure 3.6 and Table 3.4 suggest that different measurement techniques can produce the same estimation as long as the correct model is used for the technique.

**Table 3.4.** Medium size 8% gelatin before and after directional filter

	Before filter	After filter
Ultrasonic shear-wave (Medium size)	11185.57±193.686	9244.276±160.07 *
Hertzian indentaiton (Big size)	8990.333±284.04 *	

\*The two-tailed P value equals 0.22. By conventional criteria, this difference is considered to be not statistically significant.

### Correction method for ARF-OCE

In the ARF-OCE technique, the Rayleigh wave propagation speed is approximated to be the same as the shear wave speed (only a small factor of 1.05 slower) at each frequency, assuming the waves are propagating in a semi-infinite medium without any interference from the reflected waves [87]. However, some of the samples used for ARF-OCE technique are quite limited in both diameter and thickness. Therefore, the reflections or wave interference may come from both the side boundaries and the bottom of the sample. As the preliminary phantom experiments data shown in Figure 2.19, measurements on the samples with the same geometry are consistent. But when the same imaging procedure was applied on samples with the same material property but different geometry, repeatability is not guaranteed. To study this, I constructed phantoms of different geometries using 8% gelatin because 8% has the strictest boundary constraints among all of the

samples used. In order to make sure these samples have the same material property, they were cut from the same sample gelatin sample using punches and blades. Figure 3.13 (top) shows the findings on how the diameter of the sample and thickness of the sample affect the wave dispersion curves. The dispersion curve of the smaller size sample almost overlaps with the normal size one, indicating that the side boundary has little reflection effect because the frequencies used (200 Hz ~ 3500 Hz) are high enough to meet the “2-wavelength” criteria. On the other hand, the thin sample shows slight disagreement in the low frequency range, which is also observed in literature [114]. The overestimation of shear speed at low frequency for thin samples is probably caused by the occurrence of the first order symmetric Lamb waves (S0) due to the limited height of the sample (Figure 3.13 (bottom)). Lamb waves exist when surface waves reach the bottom of the sample before dying out, which generates reflective energy in the axial direction. In the experimental setup, the bottom of the sample can be considered as a fixed boundary, thus the symmetric Lamb wave is the dominant one [121]. When the thickness  $d$  is larger than one wavelength  $\lambda$ , the value of  $\omega d/V_s$  is larger than 6.28, and then the estimated wave speed will converge to the true shear wave speed  $V_s$ . As a result, the effect from the Lamb-Rayleigh wave does not affect the measurement unless the thickness of the sample is less than 1 wavelength of the wave. Since most of the samples are thick enough and satisfy this requirement, the bias caused by Lamb waves can be avoided. If some of the samples do not meet this constraint, the measurements in the low frequency range may be dropped. In the case of an ultra-thin material such as vessel wall and cornea, modifications to the experimental setup and physical model are needed to take advantage of the Lamb wave instead of Rayleigh wave.

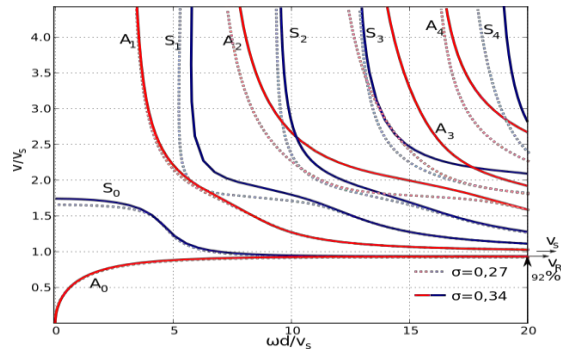
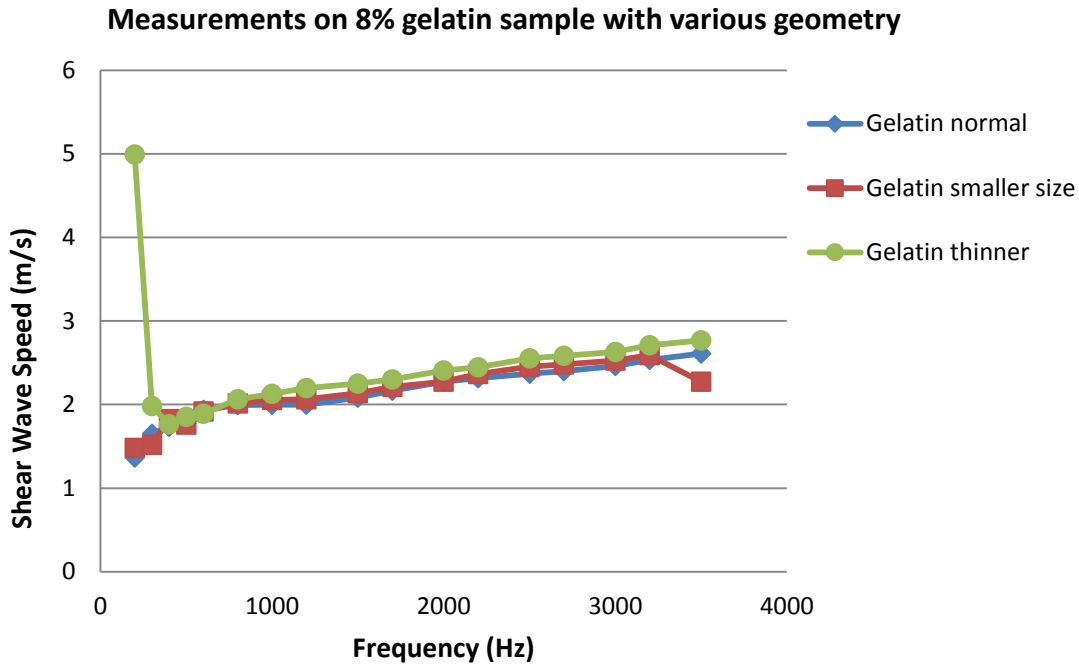


**Figure 3.13.** (top) Shear-wave dispersion curve measured on 8% gelatin sample of different geometries. Normal size sample is 34 mm in diameter and 8mm in thickness. Small size sample is 24 mm in diameter and 8 mm in thickness. Thin sample is 34 mm in diameter and 4.5 mm in thickness. (bottom) Dispersions curves of free Lamb waves (symmetric S, asymmetric A) for two different Poisson's ratios.

After boundary condition corrections are applied for both shear-wave and surface-wave measurements, their measurements were compared for 4% gelatin-concentration samples in Figure 3.14. Although each measurement has its own frequency ranges, there is an overlap range around

300 Hz where it shows good agreement between these estimates. This is the first time that anybody has shown consistent results for two different dynamic techniques. The Young's modulus values (calculated from the average of  $C_s$  estimates over all frequencies) were  $1.76 \pm 0.04$  kPa for the shear wave ultrasonic technique and  $2.18 \pm 0.14$  kPa for the surface wave ARF-OCE technique. The Young's modulus measured using quasi-static Hertzian indentation estimated was  $1.77 \pm 0.08$  kPa for the same sample (Figure 3.2). These similarities provide confidence that the wave-based elasticity imaging can reliably yield moduli that compare well with standard materials measurements. Since the viscosity of gelatin is ignored during estimation, the observed differences in modulus values can be expected, especially at high frequency. This is one of the reasons that the modulus estimations from ARF-OCT are slightly higher than the US technique. Another possible reason could be that when pouring the hot gelatin fluid into molds of different sizes, the congealing rate will be substantially different; therefore the stiffness might be affected.

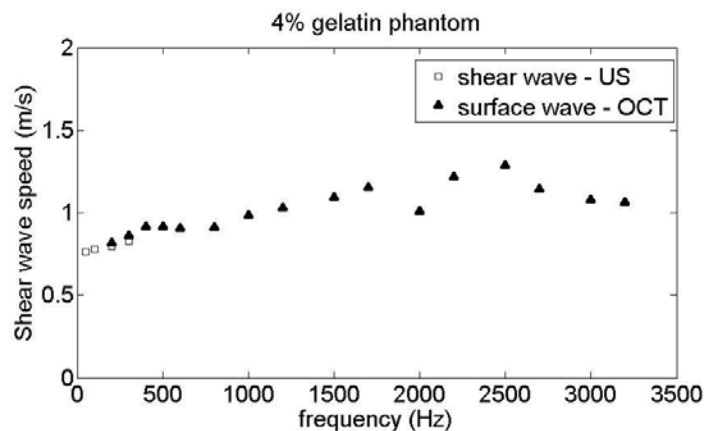


**Figure 3.14.** Comparison of wave dispersion curves measured on 4% gelatin sample using shear wave imaging technique and surface wave imaging technique. Shear wave and surface wave were tracked by ultrasound and optical coherence tomography, respectively.

### **3.2 The effect of rheological models on measurements**

Gelatin samples are well suited for cross-modality comparison between elastic imaging techniques and other material characterization techniques such as mechanical indentation. It provides methodological validation for different measurement approaches without too much interference from the choice of rheological models. In previous sections, the consistency of Young's modulus measurements among all three techniques has been achieved when the assumptions of the physical model are not violated. However, pure gelatin phantoms do not accurately model the time-dependent behavior of many soft tissues. For viscoelastic or time-dependent material, comparing different techniques is not easy. It has been proved in the previous section (Figure 3.15) and also by others [122] that all of the techniques have a good agreement in the overlapped frequencies, but it is not guaranteed that the same rheological model can have a good fit for all the techniques and produce the same model parameter estimations. There might not be a final solution for this problem, but rather some rules that could be followed from case-by-case studies. Chapter 2.2.3 preliminarily concludes that model choice will influence the final results. This chapter will focus on learning this influence through ultrasonic shear wave imaging studies.

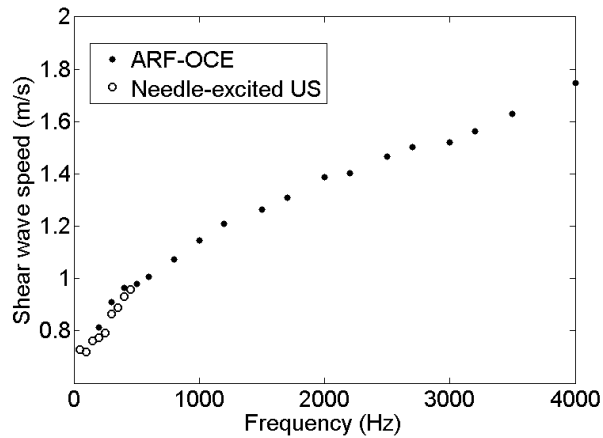


**Figure 3.15.** Shear wave dispersion curves measured on viscoelastic sample by ultrasonic shear wave imaging and ARF-OCE.

The rodent tumors that were examined in Section 2.3.3 have presented viscoelastic properties in the shear wave dispersion curves in Figure 2.14, where the Kelvin-Voigt model was used because it is a prevalent model in the field of soft tissue mechanics and usually yields reasonable measurements of the elastic modulus and viscosity modulus estimates. Table 3.5 lists some other rheological models to compare with the Kelvin-Voigt model for fibroadenomas. Figure 3.16 shows the details of the fitting, and the goodness of fitting metric – reduced  $\chi^2$  statistic is summarized in Figure 3.17. The K-V model gives larger fitting residuals for fibroadenomas compared with the Maxwell and Zener models. However, all three models fit the data from carcinomas equally well. From the shear wave dispersion curve and  $\chi^2$  values, it is not obvious which model is more appropriate. Although shear wave attenuation is not required for the technique, it could provide some insights on model choices. A simulation was first performed on the model predicted curves. Figure 3.18 shows the dispersion of shear velocities and attenuation coefficients from 0 Hz to 1000 Hz for both models and are plotted at selected values. In the figure, the dispersive behaviors vary for both models, especially in low and high frequency ranges. For shear wave velocity dispersion curve, note that Maxwell requires larger E value to approach the

K-V model in the frequency region of the measurements, which is consistent with the fitting results shown in Table 3.5.

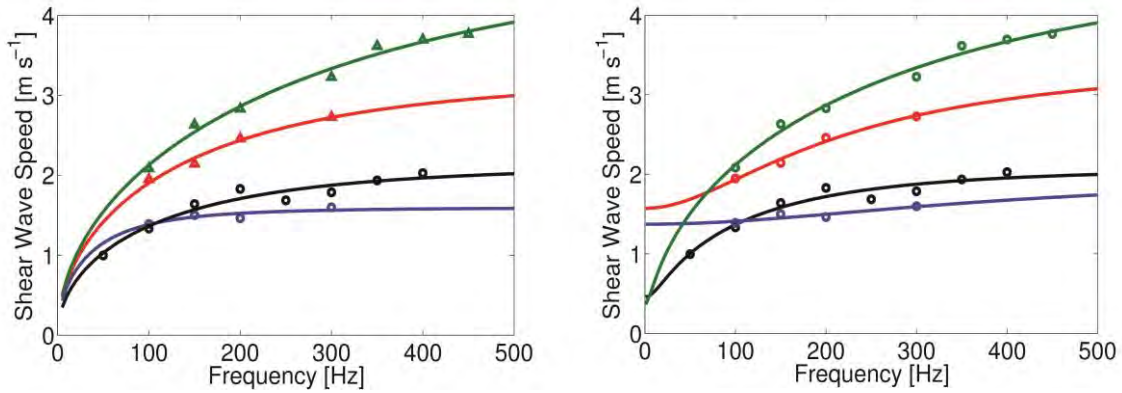
Figure 3.19 illustrates the shear wave attenuation dispersion curves from both types of rodent tumors. Due to the dissimilarity of tissue constituents (rat tumor contains more collagen and mouse tumor contains mainly cells), attenuation dispersion curves behave quite differently. Mouse carcinoma tumors have higher attenuation coefficients than rat tumors at lower frequencies and reach a plateau earlier. This behavior is similar to the Maxwell model where the convergence of  $C_s$  and  $\alpha$  is shown at higher frequencies. On the other hand, rat fibroadenoma tumors have constantly increasing attenuation coefficients, which is closer to what Kelvin-Voigt would predict. Thus, attenuation dispersion curves are correlated with tumor type, more precisely tissue components and structure, which suggests that Maxwell model is more appropriate in describing fluid-rich and cellular structures, and Kelvin-Voigt is more appropriate in describing the solid protein and muscle structures.

However, the reality might be more complicated than a “first-order” rheological model with only two elements in the model. Every tissue has both fluidic portion and solid portion in its mechanical behaviors, and different techniques will have certain emphasis on these behaviors according to the excitation method and frequency ranges. Therefore, for biphasic material like tissue, models should contain both fluid (Maxwell) and solid (Kelvin-Voigt) components [94, 122], especially for techniques like ARF-OCE which cover a wide frequency band. Combinations of the two simplest models (Kelvin-Voigt and Maxwell) include the Jeffrey model, Zener model, and higher order models such as the Generalized Maxwell model, etc. These models will be suitable for a larger variety of tissue types and techniques than just Kelvin-Voigt or Maxwell model

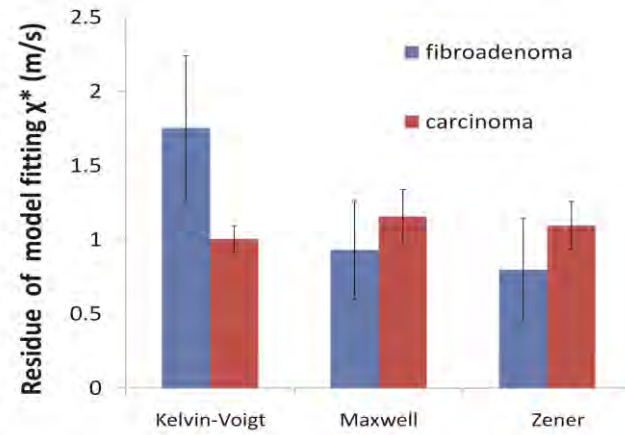
alone, and in theory will provide more comprehensive information about tissue components and structures.

Table 3.5 Estimates of viscoelastic parameters for rat fibroadenomas using different models

MODEL	Kelvin-Voigt			Maxwell			Zener			
fibroadenoma	$\mu$ [Pa]	$\eta$ [Pa·s]	$\chi^2$	$\mu$ [Pa]	$\eta$ [Pa·s]	$\chi^2$	$\mu_1$ [Pa]	$\mu_2$ [Pa]	$\eta$ [Pa·s]	$\chi^2$
1	1832.2	0.9	0.86	2558.6	3.03	0.59	3937.4	3613.9	2.06	0.76
2	1485.6	1.16	4.52	4604	1.92	1.25	4385	217.1	2.34	1.39
3	2728.6	3.46	9.55	10722	3.53	0.89	11793.8	3127.7	5.01	1.03
4	4420.4	3.54	2.71	24453	3.99	0.97	23385	128.8	4.18	0.67



**Figure 3.16.** Dots represent the dispersion curves measured in four different rat fibroadenomas, and lines represent the best-fit of Maxwell model (left) and Zener model (right).



**Figure 3.17.** Reduced  $\chi^2$  statistics for the Kelvin-Voigt, Maxwell, Zener rheological models. Error bars indicate  $\pm 1$  standard error.

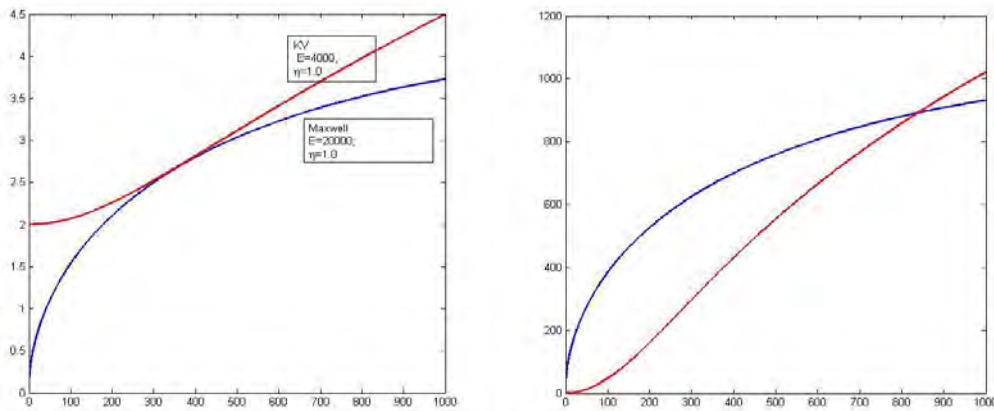


**Figure 3.18.** Simulated shear wave speed (left) and attenuation coefficient (right) as a function of frequency. Y-axis is  $C_s$  (m/s) for the left image, and  $\alpha$  (m<sup>-1</sup>) for the right one. Both have x-axis as frequency. K-V model (red curve) and Maxwell model (blue curve) are plotted. Shear wave speed is simulated from equation

$$c_s = \frac{\omega}{k} = \sqrt{\frac{2(G'^2 + G''^2)}{\rho(G' + \sqrt{G'^2 + G''^2})}}$$

equation  $\alpha = \sqrt{\frac{\rho\omega^2(\sqrt{G'^2 + G''^2} - G')}{2(G'^2 + G''^2)}}$ .

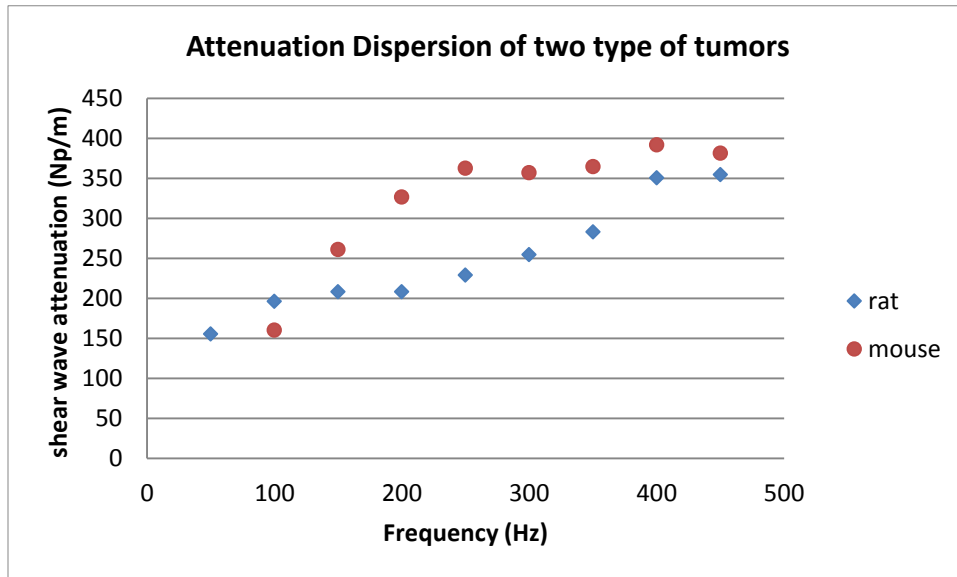


**Figure 3.19.** Experimental shear wave attenuation dispersion of rat and mice tumors. Animal tumors used in this plot are Rat 4 and Mouse 4. As shown in the figure, rat tumor data fitted to K-V model, and mouse tumor data are more like Maxwell model in the sense that shear wave speed and attenuation reach plateaus.

### 3.3 Summary

Each technique and rheological model have its own usefulness in some scenarios for some types of tissues, and if used correctly will reveal biological conditions. When making the true quantitative estimates that could be used to perform clinical diagnosis for tissue, measurement techniques (with its corresponding physical model) and rheological models are the two main parts that affect the results of the estimation. This chapter examines how techniques and rheological models affect measurements.

First, can all the techniques achieve modality independent measurements? This question has been addressed by a series of gelatin measurement studies in Section 3.1. Gelatin is chosen because it is close to a purely elastic material that does not need to imply a rheological model. The

fact that Young's modulus estimations using all three techniques give the same value demonstrates that the inter-technique agreement can be achieved as long as the physical model assumptions are not challenged. In some cases where the assumption is challenged by the presence of boundary reflections and vibrational modes, post-processing methods could be used to eliminate the bias of the measured results. Then, some viscoelastic materials were also examined, and measurements were found to be consistent in the overlapped frequency ranges, at least for the two dynamic methods. This finding ensures that 1) comparing the results from different techniques is fair, and elastography techniques can be geared to the standards that often used in literatures; 2) the full spectrum responses of the material can be obtained through different modalities, each of which has its own bandwidth.

In order to compare the model-based parameterized mechanical measurements, various rheological models and their results for tissue measurements are also examined. We learned that: 1) Simple models like the Kelvin-Voigt and Maxwell model are suitable for only a subset of tissue types due to the distinct behaviors in the low and high frequency ranges. The Maxwell model appears to be more appropriate for representing a viscoelastic fluid and the K-V model is suitable for a real solid material. A combination of the K-V and Maxwell (eg. Zener) models give a more realistic representation of material media such as biopolymers. 2) Even one type of material can exhibit very different mechanical behaviors in one test if the frequency bandwidth is broad. The rheological model must be very flexible in representing the mixing behaviors of fluid and solid components in order to incorporate the transition responses of them. It is also important to keep the number of parameters low.

It is critical to introduce a better model that could describe mechanical behaviors of a wide frequency range in different types of tissues. The model parameters should have good biological

contrast, which represent tissue components or structural properties. It is also important to maintain the balance between model complexity and model resemblance of measurements. The current integer-order models from the constitutive equation are having difficulty satisfying the above requirements simultaneously. Fractional-order rheological models, given its flexibility, wide-applicability, and mathematical simplicity, might be a good fit for biomaterials like tissues. The next two chapters will focus on the introduction of Kelvin-Voigt Fractional Derivative (KVFD) model into mechanical characterization for viscoelastic materials, and the value KVFD model brings to tissue identification and diagnosis.

## CHAPTER 4: KVFD MODELLING FOR VISCOELASTIC MATERIALS

Using the correct technique and model will assure finding the best parameters for retrieving tissue information, and thus adding diagnostic values. From previous chapters, three techniques have been successfully used to measure mechanical properties. It is shown that the results from all three techniques are consistent in gelatin samples. Therefore, the selection of methods just depends on the availability of modality. However, for time-varying materials like tissue, such comparison cannot be made due to the lack of a universal model for all techniques. Most models are specific to one technique or a narrow frequency range, and are particular to certain tissue types. It is difficult to choose a model that is applicable over the entire frequency range that covers very low frequency indentation, medium frequency shear waves used in ultrasonic shear wave imaging, and high frequency surface waves used in ARF-OCE. Kelvin-Voigt fractional derivative (KVFD) model has the potential to serve as one of the models that could fit all three techniques, and thus enabling me to investigate the value of each technique.

In this chapter, the KVFD model will be evaluated using indentation technique. To examine the ability of KVFD model in depicting viscoelastic materials, a type of viscous phantom was developed that represents more aspects of the tissue properties.

### **4.1 Background**

Fractional-derivative (FD) models have been applied in part to solve this dilemma. FD models represent viscoelastic material responses more closely than integer-order models and with

fewer parameters [123-126]. Fractional-derivative models are combinations of spring and fractional-order dashpot elements that reflects both elastic and time-dependent viscous mechanical behavior. The model fits load-relaxation data well despite a small number of fit parameters. Fractional Maxwell model, fractional Kelvin-Voigt (KVFD) model and fractional standard linear solid models have been widely used to describe the mechanical response of a variety of biological tissues as well as tissue-mimicking phantoms [127-132]. As for modeling load-relaxation curves, KVFD was shown to represent soft polymer dynamics very well, and the corresponding model parameters have been interpreted in terms of the material properties of elasticity and viscosity [132].

In this chapter, models for estimating viscoelastic properties are explored using the ramp-hold relaxation paradigm. Integer-order models expressed as Prony-series are compared to fractional-order expressions based on the Kelvin-Voigt material model. The performance of the analytical solution in describing the time-dependent mechanical response was examined using soft viscoelastic polymers with systematically varied viscosity. The effects of different experimental conditions on KVFD parameter estimations are studied; e.g., the durations of the relaxation time series included in the model fits, the strain rates of the applied ramp deformations, and measurements using spherical indentation are also compared with those of plate compression. Results are evaluated based on estimation precision and measurement independence. Conclusions and recommendations for experimental protocols using the ramp-hold relaxation test are offered.

## **4.2 Material and method**

#### 4.2.1 Gelatin-Cream viscoelastic phantom

The viscoelastic samples in this experiment are made of gelatin powder, deionized water and a skin cream each in specific weight percentages. Gelatin powder (Type B, Rousselot Inc., Dubuque IA) was mixed with deionized water in a beaker at room temperature, and heated in a 70°C water basin for 45 minutes. The beaker was covered with aluminum foil to prevent water evaporation. It was stirred every 5 minutes until visually clear. After the gelatin-water mixture was removed from the water bath, it was cooled at room temperature to 30°C, cream was added and stirred well until visibly homogeneous, and then the mixture is poured into cylindrical molds to congeal. The cylindrical mold is precisely machined to ensure a high degree of axial symmetry and flat, parallel end surfaces. Since samples retain their shape after being removed from the mold, they present a flat parallel surface to the plate compressor.

Cream (Vanicream, Pharmaceutical Specialties, Inc. Rochester, MN) was added to the molten gelatin as water was removed and the gelatin concentration held fixed in order to increase the viscosity of the sample without significantly changing stiffness. This gel-cream mixture is a solidified emulsion of cream particles suspended in liquid gelatin that is allowed to congeal into a solid. These samples express viscoelastic properties in the range of soft biological tissues. In contrast, gelatin gels constructed without the cream particles generally respond elastically to compression [36]. The molds used to form samples for spherical indentation testing are 50 mm in diameter and 20 mm in height. The molds used to form samples for plate testing are 37.5 mm in diameter and 19 mm in height. All samples were covered with plastic wrap and stored at room temperature for 16 hours after construction and before mechanical testing. It is very important that the sample-manufacturing process is exactly reproduced in detail for material properties to be reproducible day to day.

Three different samples were prepared with the same gelatin concentrations (5% by weight). The concentrations of cream were 5%, 15%, and 50% by weight, and the corresponding deionized water concentrations were 90%, 80%, and 45%, respectively. These three samples are labeled Gel5Cream5, Gel5Cream15, and Gel5Creal50 in the Results section.

#### 4.2.2 Theory of KVFD model

The Kelvin-Voigt Fractional Derivative (KVFD) model describes the time-dependent relaxation behavior of viscoelastic materials. Strengths of this model include its flexibility for describing different types of materials with just three parameters. The linear KVFD model is illustrated in Figure 4.1.

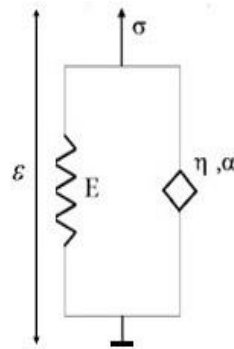


**Figure 4.1.** Schematic representation of the KVFD model

Stress  $\sigma$  is predicted from the applied strain  $\varepsilon$  given the relaxation modulus  $G$  of the material through the Boltzmann superposition integral [75],

$$\sigma(t) = \int_{-\infty}^t G(t-\tau) \frac{d\varepsilon(\tau)}{d\tau} d\tau \quad (4.1)$$

For the KVFD model, the constitutive equation for the stress-strain relationship can be expressed by the following fractional-derivative equation [133]

$$\sigma(t) = E_0 \varepsilon(t) + \eta \frac{d^\alpha \varepsilon(t)}{dt^\alpha} = E_0 \left( \varepsilon(t) + \tau^\alpha \frac{d^\alpha \varepsilon(t)}{dt^\alpha} \right) \quad (4.2)$$

where  $E_0$  is the elastic modulus,  $\eta$  is a viscosity coefficient, and  $\alpha$  is a real number between (0,1) that defines the derivative order. Letting  $\eta = E_0 \tau^\alpha$ , the relaxation time constant  $\tau$  is used in place of  $\eta$  to give the second form of Equation 4.2 to define a 3-D feature set for materials characterization  $(E_0, \alpha, \tau)$ .

The Laplace transforms of Equations 4.1 and 4.2 can be equated to show the relaxation modulus for the KVFD model is

$$G(t) = E_0 \left( 1 + \frac{(t/\tau)^{-\alpha}}{\Gamma(1-\alpha)} \right), \quad (4.3)$$

where  $\Gamma(z) = \int_0^{\infty} e^{-t} t^{z-1} dt$  is a Gamma function.

In the following sections, a mathematical solution is derived for the ramp-hold relaxation test based on the KVFD model for both the spherical-indenter and plate-compressor geometries. These are the analytic solutions fit to relaxation time series, including the ramp deformation, to estimate the 3-D feature set.

### 4.2.3 Ramp-hold relaxation solution for spherical and plate indenter

Mechanical testing employed the TA-XTPlus Texture Analyzer with two compression probes: a spherical-tipped indenter with 5mm diameter and a flat plate compressor having a diameter larger than the cylindrical samples. Load-relaxation tests with ramp deformations were performed on each sample at room temperature.

A hemispherical indentation tip is pressed into the surface of a large-size sample at a constant velocity, after which the probe position is held fixed, as the relaxation of the force on the probe is monitor over time.

A force-displacement relation is used in place of a stress-strain relation modeling spherical indentation data. The Boltzmann integral expression for spherical indentation under displacement control was shown to be [74]

$$P(t) = \frac{8\sqrt{R}}{3} \int_0^t G(t-\tau) \frac{dh^{3/2}(\tau)}{d\tau} d\tau \quad , \quad (4.4)$$

where  $P(t)$  is the force and  $h(t)$  is the displacement depth of the indenter tip into the sample. The ramp-hold displacement function is

$$h(t) = \begin{cases} kt, & 0 \leq t \leq T_r \\ h_{\max} = kT_r, & t \geq T_r \end{cases} \quad , \quad (4.5)$$

where  $T_r$  is the duration of the ramp and  $k$  is the velocity of the indenter tip during that time.

The time-varying force response predicted to occur during the ramp-hold relaxation test is derived by combining Equations 4.3 – 4.5,

$$P_r(t) = \begin{cases} 4\sqrt{R}k^{3/2}E_0t^{3/2} \left[ \frac{2}{3} + \frac{(t/\tau)^{-\alpha}}{\Gamma(1-\alpha)} B\left(\frac{3}{2}, 1-\alpha\right) \right], & 0 < t \leq T_r \\ 4\sqrt{R}k^{3/2}E_0T_r^{3/2} \left[ \frac{2}{3} + \frac{\left(\frac{t}{T_r}\right)^{3/2} \left(\frac{t}{\tau}\right)^{-\alpha}}{\Gamma(1-\alpha)} B\left(\frac{T_r}{t}, \frac{3}{2}, 1-\alpha\right) \right], & t \geq T_r \end{cases} \quad (4.6)$$

where  $B(x, y) = \int_0^1 t^{x-1}(1-t)^{y-1} dt$   $\text{Re}(x) > 0, \text{Re}(y) > 0$  is a complete beta function and

$B(a; x, y) = \int_0^a t^{x-1}(1-t)^{y-1} dt$  for  $a \in [0, 1]$  is an incomplete beta function.

The step-hold displacement function is  $h(t) = h_{\max} u(t)$ , where  $u(t)$  is the unit step function. So Equation (1) reduces to

$$P(t) = \frac{8\sqrt{R}}{3} E_0 h_{\max}^{3/2} \left( 1 + \frac{(t/\tau)^{-\alpha}}{\Gamma(1-\alpha)} \right) \text{ for } t > 0 \quad . \quad (4.7)$$

A detailed derivation is provided in [134].

The spherical indenter used in the experimental studies has a diameter one-tenth that of the sample diameter to minimize boundary effects. The maximum displacement of the spherical probe into the top surface of the sample was always  $h_{\max} = 1$  mm. However, the probe speed was varied between 0.02 - 5.0 mm/s to give a range of ramp times. Afterward, the probe was held in place for 200 - 300 s while the decaying force on the probe from viscous relaxation was measured. All tests were conducted with deionized water on top of the samples to minimize surface adhesion forces. It has been verified that water was not significantly absorbed by the samples during the experiments, and thus the mechanical properties of the phantom were not significantly influenced

by the water. The agreement was proved to be within measurement error provided the measurements were completed within an hour [68].

In the plate compression tests, a plate larger than the sample surface compresses a cylindrical sample from above and free-slip boundary conditions are assumed. The sample is placed on a flat immovable surface with its side boundaries free to expand. A ramp displacement compresses the sample and is held fixed as the force on the plate is measured over time.

The time-dependence of the ramp-hold strain function is similar to Equation 4.5, except that the strain  $\varepsilon(t)$  is used instead of displacement  $h(t)$ . Using the Boltzmann integral expression from Equation 4.1, the stress-relaxation response for the plate compressor is [75]

$$\sigma_r(t) = \begin{cases} \frac{\varepsilon_0 E_0 t}{T_r} \left[ 1 + \frac{(t/\tau)^{-\alpha}}{\Gamma(2-\alpha)} \right], & 0 \leq t \leq T_r \\ \frac{\varepsilon_0 E_0}{T_r} \left[ T_r - (t - T_r) \frac{((t - T_r)/\tau)^{-\alpha}}{\Gamma(2-\alpha)} + t \frac{(t/\tau)^{-\alpha}}{\Gamma(2-\alpha)} \right], & t > T_r \end{cases} \quad (4.8)$$

The step-hold strain function is  $\varepsilon(t) = \varepsilon_0 u(t)$ , which reduces Equation 4.1 to

$$\sigma(t) = \varepsilon_0 E_0 \left( 1 + \frac{(t/\tau)^{-\alpha}}{\Gamma(1-\alpha)} \right). \quad (4.9)$$

During plate-compression tests, samples were removed from the mold carefully before testing and placed on a flat surface. The top surface of the sample was displaced  $h_{max} = 1$  mm toward the bottom surface at ramp speeds of either 0.1 mm/s or 5 mm/s to give ramp times of  $T_r = 10$  s or 0.2 s. Samples were held for 300 s to measure stress relaxation.

The initial contact point of the plate with the sample surface was established as follows. In a preliminary step, the sample was compressed at very low constant speed (0.01mm/s) before attempting the ramp relaxation test. A short-time moving-average filter was applied to the recorded force-versus-time curve to filter a small amount of load-cell noise as the point at which the force first deviates from zero was detected. Then the probe was positioned at this point, waited at least 1 minute to let the sample recover, and started the ramp-load relaxation experiment. Because the opposing sample surfaces were flat and parallel, this simple method provided a reproducible contact point.

The ramp-hold relaxation curves for spherical indentation and plate compression tests were fitted to the KVFD analytical solutions of Equation 4.6 and 4.8, respectively. For each relaxation curve, model parameters  $E_0$ ,  $\alpha$ , and  $\tau$  were varied, and the set of parameters generating the least-squared error between model and data became the estimates. Parameters were initially selected manually to approximate the fit, which became the initial values for least-square regression fits in MATLAB. The KVFD solutions for ramp relaxation curves describe the entire ramp-and-hold experimental time series. Thus any data segments from the curve should yield the same parameter estimation within numerical uncertainties. Due to noise in the experimental data, the least-squares fitting algorithm can truncate the search early if it becomes trapped in local optimal points. Manually selecting the initial values eliminated this problem.

It should be noted that for plate-compression tests only, there is a very small linear drift of the relaxation stress not explained by the model. A similar effect was reported in [135]. Drifting might be caused by instrument drift during measurements spanning 300 s or, more likely, as the assumed nonslip boundary conditions may have a small amount of friction that delays sample expansion during plate compression. A weak linear trend term  $at$  is added to the model after the

10 s ramp concluded to improve the quality of fit. Values for slope constant  $\alpha$  were found to range between -0.004 and -0.001 in the experiments.

### **4.3 Results**

There are no established standards for calibrating viscoelastic measurements in soft materials, although comparisons among independent measurement techniques can test for precision and consistency [68]. A model-based solution can be valuable for predicting viscoelastic properties from load-relaxation time series if it satisfies the following coupled criteria: 1) The model reliably predicts sample responses with few parameters; 2) Parameter estimates are robust to changes in experimental variables and conditions; 3) The same model applies to different materials having a variety of mechanical properties in a range of interest.

In this study, I approached validation of the KVFD model solution for a ramp-hold relaxation test by first identifying a stable, reproducible, viscoelastic material. A series of measurements were made varying several key experimental parameters and observed the variability of KVFD model parameters,  $(E_0, \alpha, \tau)$ . The precision of estimates was examined by comparing KVFD results to those of the DMW model using spherical indentation and plate compression testing over a range of experimental variables. I also varied the material properties of the test samples within a small range of soft biological tissues to test model applicability.

#### **4.3.1 Impact of relaxation time on the variability of estimated model parameters**

For this study, the sample labeled 5Gel15Cream (5% gelatin, 15% cream, 80% water) is subjected to a force/stress relaxation test. The ramp time  $T_r$  is fixed at 10 s for both spherical indentation and plate compression. Figure 4.2 gives an example of the relaxation data from spherical indentation and the best fit to the model given by Equation 4.6. The four time durations examined are indicated on the time axis in Figure 4.2.

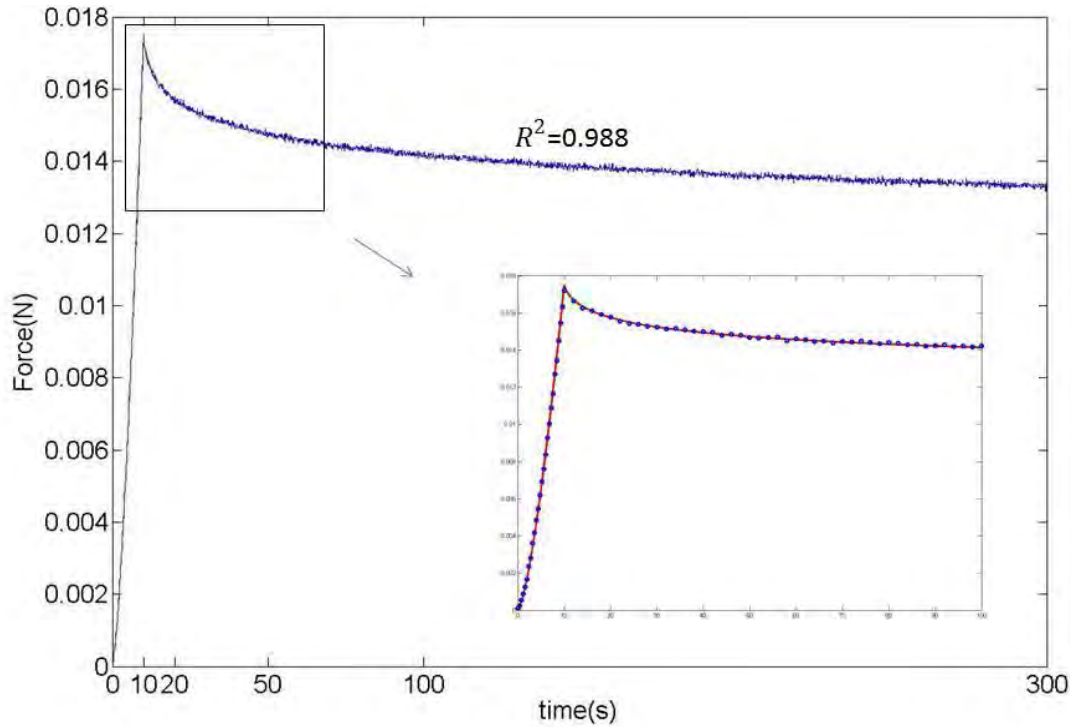


**Figure 4.2.** KVFD fitting of a measured ramp-hold relaxation curve for 5Gel5Cream sample using spherical indentation. The measured force-relaxation curve is shown as blue dots and the best-fit model curve is shown as a red dotted line. The experimental data in the zoomed figure is down sampled a factor of 10 in the ramp phase and 50 in the holding phase.

### a) Spherical indentation

Parameter values are estimated by fitting the KVFD ramp solution to different time durations of the relaxation data. Results are listed in Table 4.1. The coefficient of variation (CV) reflects the reproducibility of the fitting results for the different durations indicated in the first row of the table. CV1 represents the variability of fitting the ramp and the holding phase of the force-

measurement time series up to the time indicated, and CV2 represents the variability of fitting only the holding phase, which begins at 10 s.

**Table 4.1.** KVFD model parameters estimated from different durations of the relaxation data (top row) for the 5Gel15Cream sample using spherical indentation.

time (s)	0-20	0-50	0 -100	0-300	10-20	10-50	10 -100	10-300	CV1	CV2
$E_0$ (Pa)	2038.2	2032.1	2027.8	2021.3	2109.9	2096.2	2077.6	2068.1	0.0035	0.009
$\alpha$	0.134	0.135	0.135	0.135	0.133	0.135	0.135	0.135	0.0037	0.0037
$\tau$ (s)	28.388	29.292	29.792	30.192	19.292	22.692	25.692	29.092	0.0264	0.1730

\* CV1 values are coefficients of variation for fits including the ramp phase of the relaxation curve. CV2 values do not include the initial 10 s ramp phase. Values shown are from measurements made on one sample.

First, there is no significant change in  $\alpha$  when model fitting the holding phase at various durations with or without the initial 10 s of ramp data.  $\alpha$  is the most stable material parameter in this study; it is robust to variations in experimental parameters. Second, the elastic modulus  $E_0$  has the lowest coefficient of variation when the ramp data is included in the fit (CV1). Also, including the ramp phase, the modulus estimates decrease about 4%. Similarly, the time constant estimates  $\tau$  are most precise when the ramp data are included in the fitting procedure, and excluding the ramp biases  $\tau$  estimates. Noise in the recording of the time-varying force means that curve-fitting results may not be unique; the best fits are strongly influenced by the initial values supplied to the regression. It is believed that by including the ramp time in the fitting procedure, the chance of finding that one parameter set that best describes the entire time period is increased, thus the parameters generated are less dependent on the duration of the force data.

In comparison to some commonly used models for force-relaxation tests, parameters analogous to those of the KVFD set were obtained from a second-order Prony series assuming a Double Maxwell-arm Wiechert (DMW) model [74], yielding a relaxation modulus  $G(t)$  given by

$$G(t) = C_0 + C_1 \exp(-t / \tau_1) + C_2 \exp(-t / \tau_2) \quad (4.10)$$

As others reported [74], there is no analytic solution for the time-varying force. If analyzing the relaxation curve during the holding phase only, we can assume the force  $P_r(t)$  has a form similar to Equation 4.10,

$$P_r(t) = B_0 + B_1 \exp(-t / \tau_1) + B_2 \exp(-t / \tau_2) \quad (4.11)$$

The ramp correction technique shown in Equation (13) was adopted from the work of Mattice et al. [74]. If the correction factor is defined by  $RCF_k = \frac{\tau_k}{t_R} (\exp(t_R / \tau_k) - 1)$ , then model parameters can be corrected using

$$C_0 = \frac{B_0}{h_{\max}^{3/2} (8\sqrt{R} / 3)}, \quad C_k = \frac{B_k}{(RCF_k) h_{\max}^{3/2} (8\sqrt{R} / 3)} \quad (4.12)$$

This technique gives equations that relate  $B_k$  obtained by fitting Equation 4.11 to relaxation data and  $C_k$  in Equation 4.10. Two metrics derived from the model parameters: the infinite-time relaxation modulus  $G(\infty)$  and fraction number  $\alpha_f$  are calculated to compare with their KVFD counterparts  $E_0$  and  $\alpha$  for examining model stability under different experimental conditions.  $G(\infty)$  is set equal to  $C_0$  from Equation 4.10, and  $\alpha_f$  is defined as:

$$\alpha_f = 1 - \frac{G(\infty)}{G(0)} = \frac{\sum_{i=1}^n C_i}{C_0 + \sum_{i=1}^n C_i} \quad (4.13)$$

Fitting the DMW model to the same relaxation data, the results are summarized in Table 4.2. Because there is no analytic solution for ramp loading, only the holding phase was fitted to Equation 4.11. Model parameters are found for ramp indentation using Equations 4.12 and 4.13.

**Table 4.2.** DMW models parameters estimated from different durations of the relaxation data (holding phase only) for the 5Gel15Cream sample using spherical indentation.

time (s)	10-20	10-50	10-100	10-300	CV2
$C_0$ (Pa)	1553.2	3265.9	3308.6	3116.4	0.2997
$\alpha_f$	0.566	0.614	0.587	0.580	0.0488
$\tau_1$ (s)	7.47	2.485	3.66	121.00	1.7314
$\tau_2$ (s)	2.02	46.44	41.33	9.17	0.9053

\* CV2 values may be compared with those in Table 1.

Among the DMW parameters,  $\alpha_f$  stands out as relatively stable, however the other parameters are sensitive to the duration of the relaxation data selected for inclusion in model fitting. Compared with KVFD model parameters  $E_0$ ,  $\alpha$ , and  $\tau$  parameters, DMW parameters  $C_0$ ,  $\alpha_f$  and time constants  $\tau_1$  and  $\tau_2$  have CVs that are 4~30 times larger. Greater estimation precision indicates a uniqueness of the KVFD solution across the entire measurement time. In summary, the KVFD ramp solution for spherical indentation (Equation 4.6) reliably and precisely describes the entire relaxation time series with less parametric variability than the DMW model. Including the ramp portion of the relaxation data improves the fit, which yields more precise model parameter estimates. One cannot expect the two models to give the same values, but it is expected that the estimates for each model to be independent of the duration of the data used in the model fitting procedures.

## b) Plate compression

The analysis was repeated for plate compression on 5Gel15Cream samples. Parameter estimates are found from the solution derived for the KVFD model and plate compression geometry in Equation 4.8. These results are listed in Table 4.3. For comparison, fitted results using the DMW model also for plate compression and the same durations of relaxation data are summarized in Table 4.4. Note that the analytical solution for the DMW model during the ramp-loading period can be derived for plate compression but not spherical indentation.

From the data in Tables 4.3 and 4.4, the KVFD model parameters are found to be much more stable with respect to the duration of the relaxation curve when compared with those of the DMW model. Notice too that the KVFD model has fewer and more precisely estimated parameters, which offer major advantages when these parameters are mapped into elasticity image data provided contrast is also transferred with high fidelity.

**Table 4.3.** KVFD parameter estimates from different durations of the plate compression relaxation curve

time (s)	0-20	0-50	0 -100	0-300	10-20	10-50	10 -100	10-300	CV 1	CV 2
$E_0$ (Pa)	2019.7	2031.1	2029.6	2029.4	2089.3	2039.3	2032.0	2031.0	0.0026	0.0136
$\alpha$	0.135	0.1360	0.1360	0.1360	0.134	0.135	0.135	0.136	0.0037	0.006
$\tau$ (s)	80.53	76.56	77.06	73.64	30.56	56.83	61.62	70.37	0.0367	0.3124

\* Sample used is 5Gel15Cream. CV1 includes the initial 10 s ramp data and CV2 does not. Values shown are from measurements on one sample.

**Table 4.4.** DMW parameter estimates from different durations of the plate compression relaxation curve.

time (s)	0-20	0-50	0 -100	0-300	10-20	10-50	10 -100	10-300	CV 1	CV 2
$C_0$ (Pa)	3902.0	3664.0	3521.0	3299.0	3333.1	3567.7	3558.2	3216.5	0.0704	1.410
$\alpha_j$	0.646	0.329	0.293	0.314	0.239	0.194	0.192	0.277	0.0380	0.1371
$\tau_1$ (s)	1.02	25.49	46.22	99.98	91.37	34.98	41.83	169.1	0.7335	0.9758
$\tau_2$ (s)	10.59	2.04	4.39	7.22	46.57	31.97	22.54	20.03	0.3968	0.6087

\*Sample used is 5Gel15Cream. CV1 includes the initial 10 s ramp data and CV2 does not.

### 4.3.2 Impact of ramp time $T_r$ on model parameter estimates

$T_r$  should not influence parametric estimates provided the model fits the measurements equally well over a practical range of applied indentation speeds. For spherical indentation, a strain of 0.05 is applied over a range from 0.2 s to 100 s. Below a  $T_r$  threshold value, quickly deforming the sample to approximate a step function is likely to create an underdamped response in the instrument that is not accounted for by the model. The variability of parameters estimated from the KVFD ramp solution for ramp durations between 0.2 s and 100 s are repeated on several 5Gel15Cream samples. There is at least 30-minute waiting time between the measurements for the same samples for the samples to fully recover before the next test. All measurements were made on three 5Gel15Cream samples from the same batch.

Figure 4.3 shows the fitting results for  $T_r$  values of 0.2 s, 33 s, 50 s and 100 s. The  $R^2$  metric for the same ramp times are found in Table 5, which shows the data are well described by the best-fit model especially for  $T_r \geq 10$  s.  $R^2$  will not equal to 1 because of signal-independent noise in the time-varying force measurements. These results suggest that material properties are not strain-rate dependent in this range and the model consistently accounts for the force relaxation occurring during the ramp deformation.

It is expected that all of the curves in Figure 4.3 will converge at large relaxation times because the elastic modulus at infinite time  $G(\infty)$  is equal to  $E_0$  in the KVFD model, which does not depend on  $T_r$ . As shown in Figure 4.3, relaxation curves for different ramp times tend to converge for relaxation time  $>250$  s except at  $T_r = 0.2$  s, suggesting the step-relaxation response is biased by the measurement process.

**Table 4.5.** Coefficient of determination  $R^2$  for goodness fitting measurement of 5Gel15Cream sample and the KVFD model

$T_r$ (s)	0.2	2	10	20	33	50	100
$R^2$	0.968	0.979	0.988	0.988	0.988	0.989	0.988

The stability of the three KVFD parameter estimates can be assessed from the plots of Figure 4.4. When  $T_r$  is between 10~50 seconds, all three parameters are influenced very little by  $T_r$ . Among all these parameters,  $\alpha$  has the smallest CV because it is only sensitive to the shape of the relaxation curve, whereas  $E_0$  is influenced by the amplitude that depends on the initial contact between the probe and the sample surface. Variability in initial contact is well known to cause uncertainty in model-parameter estimates.  $\alpha$  is the most stable parameter, while  $\tau$  is significantly more dependent on  $T_r$  compared with  $E_0$  and  $\alpha$ .

Very small  $T_r$  can approximate a step deformation. However, indenting at high probe velocity introduces uncertainties from instrument oscillations. As shown in figure 4 when  $T_r \leq 10$

s, estimated parameters deviate from values obtained at longer ramp times where a plateau is reached.

Ramp deformations are preferred over steps; nevertheless, measurements should be made over a range of  $T_r$  when investigating different sample types to ensure a plateau is reached. If  $T_r$  is too long, the measurement system might drift or sample properties might change. For this emulsion, parameter estimates are stable for  $10 \leq T_r \leq 50$  s. Others also found that short-ramp relaxation data fitted to a step-relaxation solution can result in big parameter errors [74, 136].

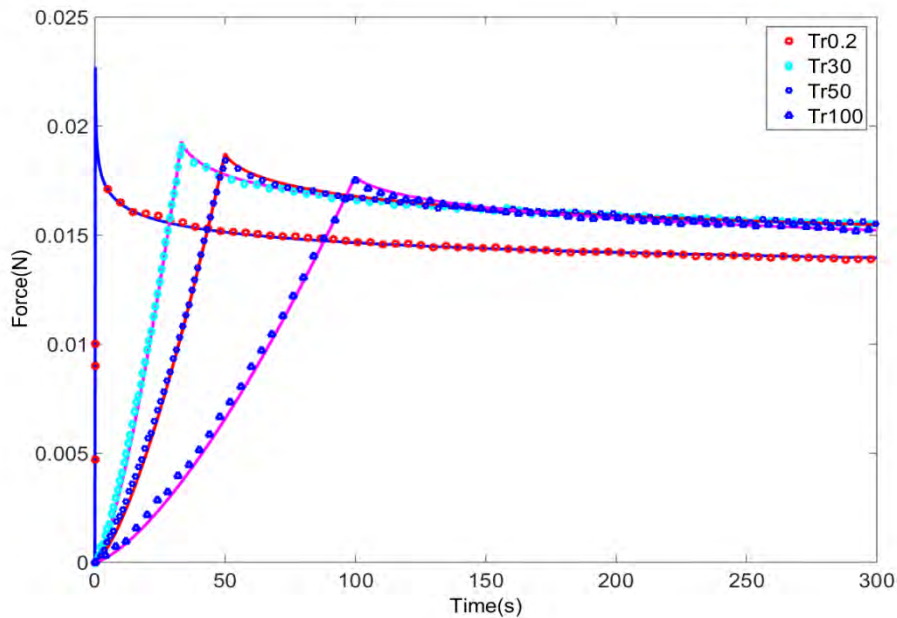


**Figure 4.3.** Illustration of KVFD model fits to data from 5Gel15Cream samples acquired using ramp times between 0.2 s and 100 s. Points plotted are experimental relaxation data and the curves use the best-fit KVFD model-based solutions. Experimental data are down sampled by factors of 10-50 in the ramp phase and 120 in the holding phase for display purposes.

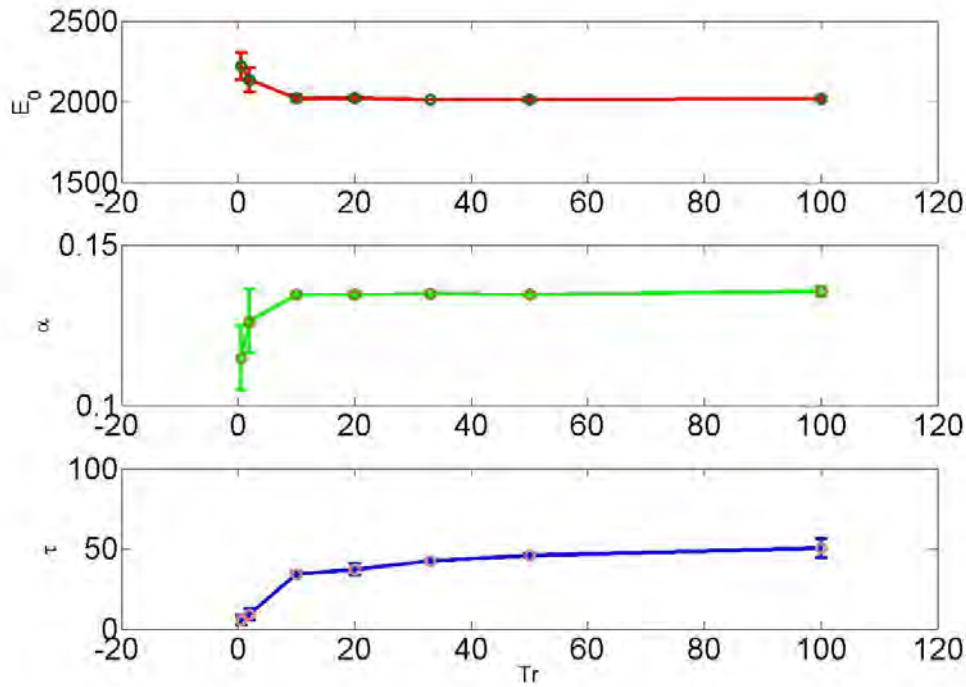


**Figure 4.4.** Estimated parameters for the 5Gel15Cream sample measured for different ramp times,  $T_r$ . Measurements are indicated by the mean points  $\pm 1$  sd. Means are averaged over data from three samples. Lines are added only to clarify trends.

### 4.3.3 Quantifying samples with varying properties

The above two sections discuss the stability of the parameters estimated by the KVFD and DMW models from ramp relaxation data on one type of sample (5Gel15Cream). In this section, samples with different viscosities are examined for different stress-strain probe geometries.

Samples with three different cream concentrations (5%, 15%, 50%) and the same gelatin concentration (5%) were constructed. 3-5 samples from the same batch of each material type were prepared for analysis. The entire recorded time series including the ramp phase were fitted to the proposed ramp solutions. Figure 4.5 shows examples of experimental relaxation curves and

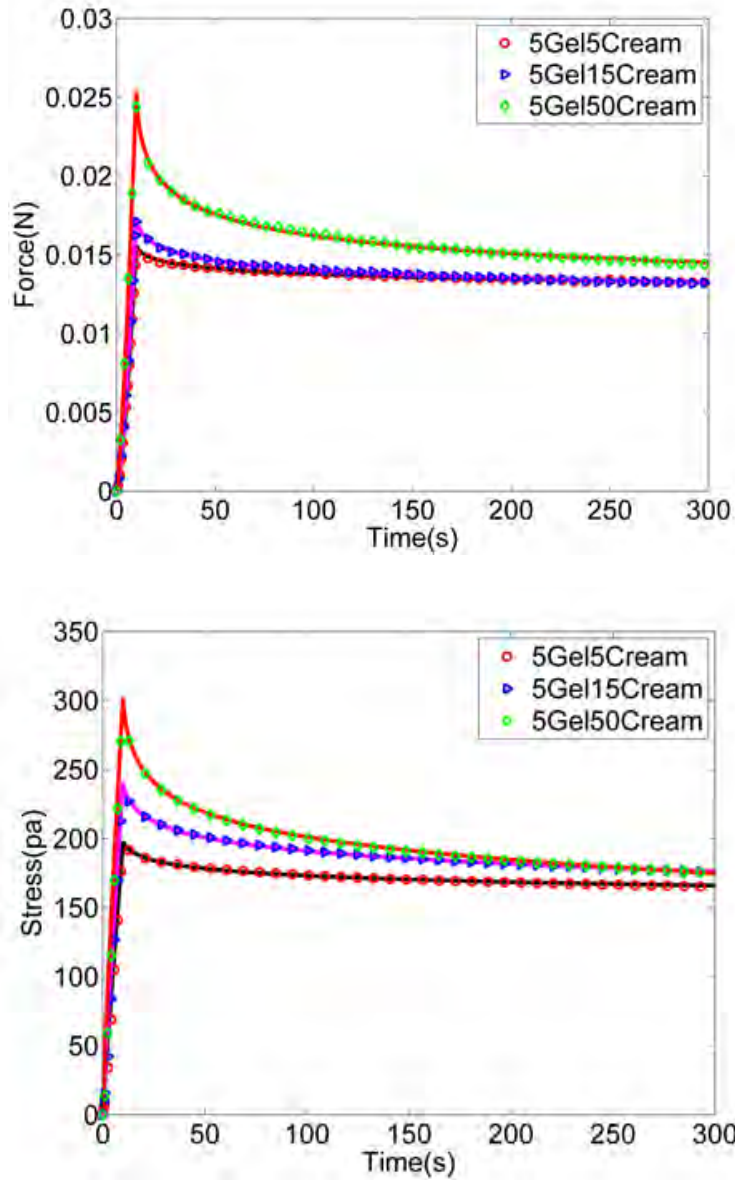
corresponding model predictions for each sample concentration for tests using spherical indentation (top) and plate compression (bottom). The models represent the experimental data very well; i.e.,  $R^2 \geq 0.98$ .

Table 4.6 contains the numerical values of model parameters from spherical indentation and plate compression tests. The results for the two geometries agree within one standard deviation of the measurement. Students T-test suggested that the two measurements have no significant difference for all cream concentrations at the 0.05 significance level. The high consistency of estimates comparing two testing geometries further confirms the reliability of utilizing the ramp solution of the KVFD model to describe viscoelastic properties.

**Table 4.6.** Comparison of parameter estimates from spherical indentation and plate compression testing using the KVFD model and emulsion samples with cream concentrations of 5, 15, and 50% to vary the viscosity.

Sample		5%	15%	50%
Spherical indentation tests	$E_0$	1782.51±53.20	2020.92±28.31	1952.51± 20.62
	$\alpha$	0.0768±0.002	0.135±0.001	0.209±0.002
	$\tau$	38.69±19.82	34.31±13.61	150.6741±11.48
Plate compression tests	$E_0$	1754.90±56.61	2029.30±57.73	1942.31 ±32.12
	$\alpha$	0.0798±0.002	0.136±0.005	0.216± 0.007
	$\tau$	47.56±21.21	68.80± 36.06	159.46±15.77

\* The mean value for measurements obtained on three samples at each cream concentration are shown and the error bars are ±1 sd.



**Figure 4.5.** Spherical indentation (top) and plate compression (bottom) test measurements (points) along with best-fit KVFD solutions (lines). The three curves correspond to the samples listed in the legend. The experimental curve is down sampled by a factor of 5~10 in the ramp phase and 100~150 in the holding phase.

#### 4.4 Discussion and conclusion

Experimental error contributes uncertainty to model parameter estimates. Except for the random error from force/displacement sensors, parameter uncertainty could originate from several sources in this study.

First, inaccuracies in recording indentation depth  $h_{max}$  can add significant bias to parameter estimations, especially  $E_0$ . Unlike stiff materials, it is challenging to identify the moment of the initial contact with the indenter probe when studying soft, wet tissue-like materials. Any deviation from the exact indentation depth, including surface roughness, biases  $E_0$ .

Second, errors occur as part of the fitting process. Least-squares fitting of experimental data to model functions is challenging because of noise in the force measurements, which enables the regression algorithm to settle into local minima rather than the global minimum. The problem is amplified as the number of model parameters increases. The experience enabled us to select model parameters when initiating numerical searches that were close to those giving a global minimum error. Fitting the full duration of the ramp-hold relaxation curve yields more precise parameter estimates by avoiding local minima traps. Also, the concise feature set of the KVFD model coupled with the ramp-hold stimulus leads to more reliable parameter estimates.

Third, despite my best efforts to manufacture uniform test materials reproducibly, there remain variations in material properties within and among the samples tested. The mechanical properties of hydrogels are affected by the details of thermal history, including manufacturing temperature, heating duration, cooling rates, time and temperature at which the cream is added. The fact that gelatin stiffness varies over time when chemical cross-linkers are not used and with

pH further makes the sample elastic modulus vulnerable to measurement variations [68]. I was aware of these influences and made every effort to minimize all material property variations by standardizing the sample manufacturing process.

Finally, the boundary conditions of the sample are another common source of variation in indentation testing of soft materials. Inner-sample stress variations near stiff or soft boundaries influence force measurements. The general rule of thumb for spherical indentation is for the diameter of the probe to be less than one tenth of the sample diameter. The validity of this rule was confirmed for representative gelatin samples recently [68]. Indented samples were 50 mm in diameter for a 5 mm probe diameter.

It is verified that  $T_r$  does not produce significant changes in model parameter estimates provided  $T_r$  is larger than 10 s in these emulsion samples. Including the ramp deformation, the model fits involving force/stress relaxation data from 50-300 s in duration yield equivalent results.

Samples were deformed using two geometries in this study: spherical indentation and plate compression. Each has advantages under different situations. The spherical indenter minimizes the effects of irregular sample geometries and has fewer boundary effects as long as the diameters of the samples are much larger than indenter. Spherical indentation also has no strict requirement on surface flatness, as long as a small flat region can be found. It is widely used to characterize viscoelastic materials. However, depending on the dynamic range of the load cell, spherical indentation may not be ideal for very soft materials ( $<3$  kPa) as the contact area is too small to generate sufficient force to avoid significant quantization errors in digital force measurements. In contrast, plate compression increases the net force in soft materials, using more of the dynamic range of the sensor, but requires the sample surface to be very flat. Also, sample area and height

must be precisely measured since they strongly influence stress and strain calculations. Moreover, plate compression of samples induces a small drift in relaxation force over time when the frictional forces at the sample-plate surface are non-uniform. The choice between the two geometries depends on sample properties, where spherical indentation is preferred except for very soft samples.

In summary, closed-form solutions for ramp-relaxation testing of soft viscoelastic materials involving the KVFD model give precise estimates of model parameters for spherical indentation and plate compression within a broad range of experimental conditions. These parameters can be interpreted in terms of viscoelastic properties of the material. Step deformation experiments should be avoided when possible. The consistency of results shown in this report suggests that experimentally-independent estimates are possible by fitting models to measurements spanning the entire force-relaxation time series. Other rheological models should be explored, but the results suggest the ramp-relaxation experiment combined with the concise parameter set of the KVFD model offers much estimation stability and precision. Since there are no standard materials for calibrating relaxation measurements, it cannot be claimed to measure intrinsic material properties. Nevertheless, the high precision and independence of the results on experimental parameters suggests this approach offers advantages for mechanical measurements of soft materials in the elastic modulus range of many soft tissues (<10 kPa) where precise measurements can be difficult to achieve.

## CHAPTER 5: ASSESSING COMPOSITIONAL AND STRUCTURAL INFORMATION OF TISSUE USING KVFD MODEL

Previous chapters mainly focus on two topics in tissue mechanical characterization: measurement techniques and rheological models. Three techniques have been successfully developed to measure mechanical behaviors at distinct frequencies (see Chapter 2), and the consistency of quantifying elastic modulus using these techniques was verified through gelatin phantoms (see Chapter 3). Commonly used models such as the Kelvin-Voigt and the Maxwell models demonstrate usefulness for some tissue types and frequency bandwidth, however, the Kelvin-Voigt fractional derivative (KVFD) model is more representative in describing viscoelastic behaviors of a large collection of soft tissue types, with just one additional parameter, which is the fractional order (see Chapter 4). The KVFD model is also suitable for modeling responses captured within a wide frequency bandwidth.

With these techniques and models being developed, a more critical question needs to be addressed: what is the biological interpretation of the model parameters or is there any correlation between tissue and model. Translating these model parameters into a concise set of intrinsic mechanical properties related to tissue composition and structure remains challenging. In this chapter, I will focus on correlating the mechanical parameters estimated by the KVFD model with tissue components and structures, and evaluating the sensitivity of these parameters in reflecting tissue changes. Two different measurement techniques, at the low and high frequency ends respectively, are used for mechanical characterization, and the model parameters obtained are compared in terms of the accessibility to various features about the tissue. These topics are first explored using the same biphasic samples used in the previous chapter. The proportion of the two

main components (gelatin and cream) will be varied in order to mimic the compositional changes. Because of its compositional simplicity, it is easier to identify the relationship of each component with the estimated model parameters. The findings on the relationship will be confirmed with the *ex vivo* liver studies, where livers are undergone different thermal alterations.

## **5.1 Material and method**

### *a) Gelatin-Cream phantoms*

The congealed gelatin-cream samples are emulsions of cream particles suspended within the denatured collagen-polymer aggregates, where each cream particle in the emulsion is itself a finer-scale emulsion. Gelatin represents the extracellular matrix in tissues, and Vanicream represents pockets of interstitial lipid. The phantom is simple to make, has adjustable components, samples have reproducible properties, and the two components are independent of each other. For a fixed gelatin concentration, as the concentration of cream is increased in a sample, water is removed so the total sample mass remains at 100 g. This recipe is scaled up to produce at least 6 samples at every concentration. As long as the concentration of the gelatin component is fixed, the sample stiffness remains roughly constant. Cream adds a fluidic component that generates a time-varying mechanical response during quasi-static compressive macro-indentation. Without cream, the pure gelatin responds elastically to indentation.

The detailed manufacturing process of the biphasic phantom has been described in Section 4.2.1. To provide a broad range of time-varying mechanical responses similar to those observed in soft parenchymal tissues, both gelatin and cream concentrations are varied as follows. At each of three gelatin concentrations (3%, 5%, and 8% by weight) 6 samples are constructed at one of five

different cream concentrations (0%, 5%, 20%, 30%, and 50% by weight). Samples labeled G3C5 contain 3 g gelatin, 5 g Vanicream, and 92 g deionized water per 100 g of sample material. A sample labeled G8C20 has 8 g of gelatin powder, 20 g of cream, and 72 g of water per 100 g. From magnified visual inspection of the samples, it appears that cream particles in the congealed gel samples are liquid at room temperature (22 °C) used for measurements.

Since the elastic modulus of the samples is very sensitive not only to component fractions but to the thermal history of the samples during manufacturing and storage, the samples were made during three different days, 2 samples each day. In this way, inter-sample variability would be observed as well as measurement uncertainty. Error bars in plots summarizing gel-cream sample measurements are standard deviations measured from 6 samples unless otherwise noted.

In this study, two major techniques will be used to measure the same material: indentation technique and surface wave ARF-OCE technique. My attempt is to compare the estimated KVFD parameters from the two techniques in terms of the correlation with material compositional change. There are several reasons that the needle-based ultrasound technique is not included. First, the frequency ranges of the ultrasonic technique (100 Hz ~ 500 Hz) are covered by the ARF-OCE technique (200 Hz ~ 5000 Hz). Second, both ARF-OCE and ultrasonic techniques estimate the same quantity - wave propagation velocities at multiple frequencies, and the overlapped frequency region should be consistent (proved in Figure 3.14). Therefore, the ultrasonic method is not used. Another important reason for choosing the optical technique over the ultrasonic technique is that the KVFD model is fitted to the data in frequency domain. A broader frequency bandwidth would increase the reliability of the estimations.

*b) Indentation technique*

Mechanical tests were conducted on all samples using the TA-XT Plus Texture Analyzer (Texture Technologies, Algonquin, IL USA) with a 5-mm-diameter spherical indentation probe. Two mechanical tests were performed on each sample: a ramp load-unload hysteresis test and a force-relaxation test with ramp loading. The time series data for the two experiments are illustrated in Figures 2.2 and 2.3. All of the hydrogel samples were tested while bonded to their cylindrical molds. The size of the mold was shown to be large enough to avoid significant boundary influences during indentation for pure gelatin samples at concentrations between 3% and 8% [68].

During ramp-hold force-relaxation testing (section 2.1.2), the maximum indentation depth was  $s_{max} = 1$  mm applied at the center of the flat cylindrical sample face. The load-on ramp speed was  $v = 0.04$  mm/s delivered during a ramp time of  $T_r = 25$  s. Subsequently, the probe position was held constant for 300 s as relaxation of the force was monitored. During the load-unload testing (section 2.1.1), where a ramp-load and ramp-unload sequence was applied, the same experimental parameters  $v$  and  $T_r$  were applied. Other details of the experiments are the same as the methods of Chapter 4.

Ramp-relaxation measurements for each gel-cream sample were combined in a regression fit with Equation 4.6 to estimate the KVFD model parameters  $E_0$ ,  $\alpha$ , and  $\tau$  for that sample. For example, the best-fit model response for sample G5C20 is shown along with the measurement data on the left side of Figure 5.1. Applying the same parameter estimates (without further fitting), the load-unload responses can be predicted theoretically by combining Equation 2.2 and Equation 4.4, and then compare with the experimental measurements (shown on the right side of Figure 5.1). The KVFD model parameters estimated from data obtained using the ramp-hold experiment

closely predicts data obtained from a load-unload experiment. The discrepancy at the end of the two curves (near  $t = 50\text{s}$ ) occurs because the model does not allow the probe to separate from the sample surface. Experimentally, the probe that was sprayed with a lubricant so it detached from the sample surface before returning to the initial height.

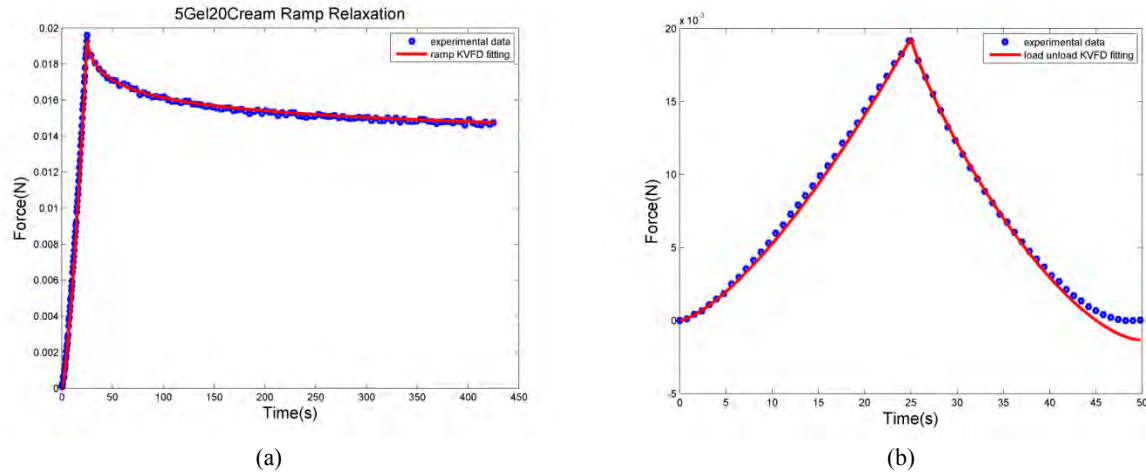


**Figure 5.1.** Data and model fitting for the ramp-relaxation (a) and the load-unload experiments (b). (a) Fitting Equation 4.6 (solid line) to the ramp-relaxation data (dots) acquired from a G5C20 sample, we found the KVFD model parameters  $E_0 = 2.38$  kPa,  $\alpha = 0.163$ , and  $\tau = 8.31$  s. (b) Applying those same parameter values to predict force  $P(t)$  for the load-unload experiment that closely represents the measurements (dots).

c) *Wave propagation technique*

All of the samples prepared for indentation tests and ARF-OCE tests were from the same gelatin batch. The gelatin and cream mixture was congealed in a large deep petri-dish. 24 hours later, the whole piece was cut into several cylindrical samples (with 25 mm in diameter and 8 mm in thickness each) for ARF-OCE measurements. Surface wave based ARF-OCE experiments were performed in the same manner as the experiments in Chapter 2 and 3. The shear wave speeds were analyzed from the velocity of the waves propagating at the sample surface, and the dispersion curves were prepared for rheological model fitting.

The relationship between the shear wave speed dispersion curve and the complex modulus is defined in Equation 2.10. For the Kelvin-Voigt model, the storage modulus  $\mu_r = \mu_1$  and the loss modulus  $\mu_i = \omega\mu_2$ . The storage and loss modulus for KVFD model is defined in [130]:

$$\mu_r = \mu_1 + \mu_1 \left(\frac{\mu_2}{\mu_1}\right)^\alpha \omega^\alpha \cos\left(\frac{\pi}{2}\alpha\right) \quad (5.1)$$

$$\mu_i = \mu_1 \left(\frac{\mu_2}{\mu_1}\right)^\alpha \omega^\alpha \sin\left(\frac{\pi}{2}\alpha\right)$$

If  $\alpha = 1$ , Equation 5.1 becomes the Kelvin-Voigt model. If  $\alpha = 0$ , then  $\mu_i = 0$ , indicating that there is no loss for this material. Furthermore, if let  $\tau = \frac{\mu_2}{\mu_1}$ , then  $\mu_1 \left(\frac{\mu_2}{\mu_1}\right)^\alpha = \mu_1 \tau^\alpha = \eta$ , where  $\eta$  is the viscosity coefficient mentioned in the ramp relaxation method. Some examples of how well the KVFD model fit shear wave imaging results are shown in Figure 5.2.

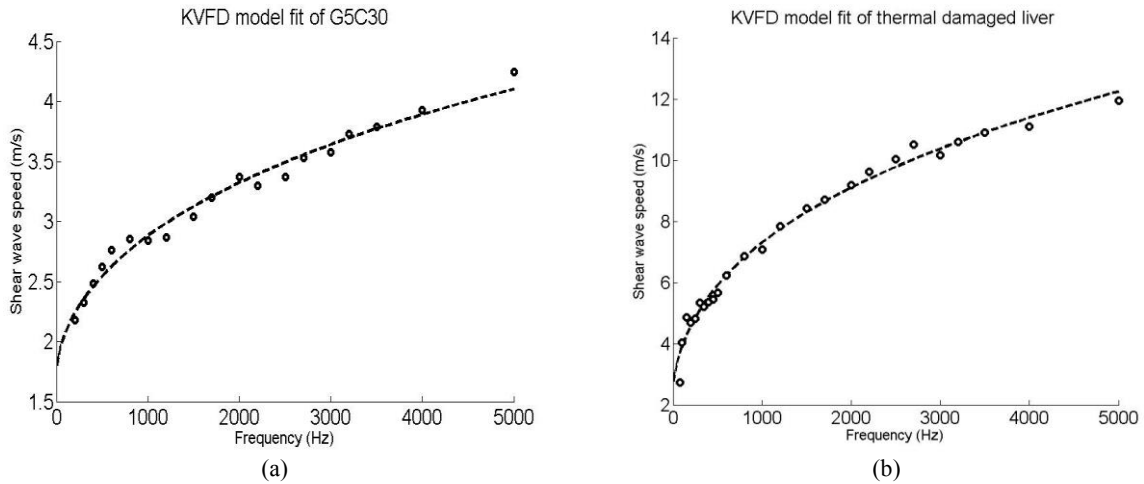


**Figure 5.2.** KVFD model fitting for the dispersion curves measured by ARF-OCE. (a) Fitting Equation 5.1 (dash line) to the shear wave speed dispersion data (circles) acquired from a G5C30 sample, we found the KVFD model parameters  $\mu_1 = 2.01$  kPa,  $\mu_2 = 2.12$  kPa s and  $\alpha = 0.49$ . (b) Fitting Equation 5.1 (dash line) to the shear wave speed dispersion data (circles) acquired from a thermal damaged liver sample. KVFD model parameters for damaged liver is  $\mu_1 = 5.38$  kPa,  $\mu_2 = 29.9$  kPa s and  $\alpha = 0.62$ .

## 5.2 Interpretation of KVFD model parameters in biphasic phantom

The KVFD model can closely predict mechanical behaviors obtained from both quasi-static and dynamic techniques, thanks to the flexibility that the fraction order  $\alpha$  provides. Others have also found good correlation between the fractional derivative models and experimental measurement data of viscoelastic media [139-140]. The next step is to study how the estimated KVFD model parameters are correlated with tissue microstructural signatures and components. In addition, how one would interpret changes of each parameter differently when different techniques are used. In the following two subsections, the biphasic phantoms with various concentrations of gelatin (solid matrix) and cream (fluid) will be used for the investigation of KVFD model parameters from both low frequency indentation measurement and high frequency wave propagation measurement. The contents of this section are based on the paper [137] which is in preparation.

### 5.2.1 Low frequency indentation measurements

From Equation 4.3, we can infer that  $E_0$  is the relaxation modulus measured at infinite time, i.e.  $E_0 = G(\infty)$ . The fractional-order parameter  $0 < \alpha < 1$  is widely regarded by many people as a measure of material fluidity; specifically,  $\alpha \rightarrow 0$  for solids,  $\alpha \rightarrow 1$  for fluids, and intermediate values reflect mixtures of the two phases [142, 143]. Relaxation time constant  $\tau$  scales measurement time  $t$  in the power-law  $(t/\tau)^{-\alpha}$  of Equation 4.3. It is a measure of the time required for the stressed medium to relax and reach temporal equilibrium in terms of force and displacement. Data and simulations will be presented to support and amplify upon those interpretations.

*a) Elastic parameter  $E_0$*

The elastic modulus measured by applications of the Kelvin-Voigt (integer-order derivative) or KVFD models is approximately the shear modulus [68, 81, 98]. To show this is also true for KVFD model, I compared  $E_0$  with the elastic modulus determined from Hertzian contact theory and shear-wave propagation measurements. Since the latter quantities only apply to linear-elastic solids in a semi-infinite geometry, measurements in pure-gelatin cylinders were acquired for these comparisons; i.e., samples G3C0, G5C0, and G8C0. The shear modulus was estimated via Hertzian theory by assuming gelatin gels are incompressible. In that case, Hertzian estimates of Young's modulus are divided by three to estimate shear modulus.

Table 5.1 shows that values for the KVFD parameter  $E_0$  are approximately equal to the shear modulus as expected using the same force-displacement time series. The table also shows the results are approximately equal to those using other measurement techniques [68, 81, 98].

**Table 5.1** Comparison of  $E_0$  and shear modulus values from gelatin gel samples

Gelatin % (sample label)	KVFD $E_0$ (Pa)	Hertzian Shear Modulus (Pa)	Shear modulus <sup>†</sup> (Pa)
3% (G3C0)	329 ± 11	292 ± 14	320 ± 28**
5% (G5C0)	766 ± 30	806 ± 18	930*
8% (G8C0)	2120 ± 80	2070 ± 27	2286 ± 315***

\*Measurements from [68] in pure gelatin at concentrations of 2%, 4%, 6%, and 8% were fit to the polynomial  $y = 178.75x^2 - 426.5x + 485$  to interpolate and estimate a value at 5%. Thus no error bar is reported.

Orescanin et al. reported gelatin prepared in the manner of our study by applying an ultrasonic impulse-response measurement method to 3% gelatin\*\* [81] and rheometer-based estimates to 8% gelatin \*\*\* [98].

<sup>†</sup>Comparisons are with previous measurements made in our lab to minimize sample-preparation variability.

Estimates of  $E_0$  for all gel-cream samples are summarized in Figure 5.3 (a). Each curve is formed from data using a different gelatin concentration. Clearly,  $E_0$  increases with gelatin concentration.  $E_0$  also increases with cream concentration initially, which is probably from molecular level changes made to the crosslinking structure in the denatured collagen aggregates

with the addition of cream. However, sample stiffness is relatively insensitive to cream concentrations above 20%<sup>3</sup>. Two-way ANOVA test results showed significant differences between various gelatin concentrations ( $p = 0.0005$ ) and little significance to the differences between various cream concentrations ( $p = 0.129$ ) [27].

In summary, the KVFD model parameter  $E_0$  approximates the shear modulus. It is sensitive to gelatin concentration but relatively insensitive to cream at concentrations greater than 20%. Hence,  $E_0$  reflects sample stiffness determined primarily by gelatin concentration. It is relatively independent of its fluidic content for cream concentrations between 5% - 50%.

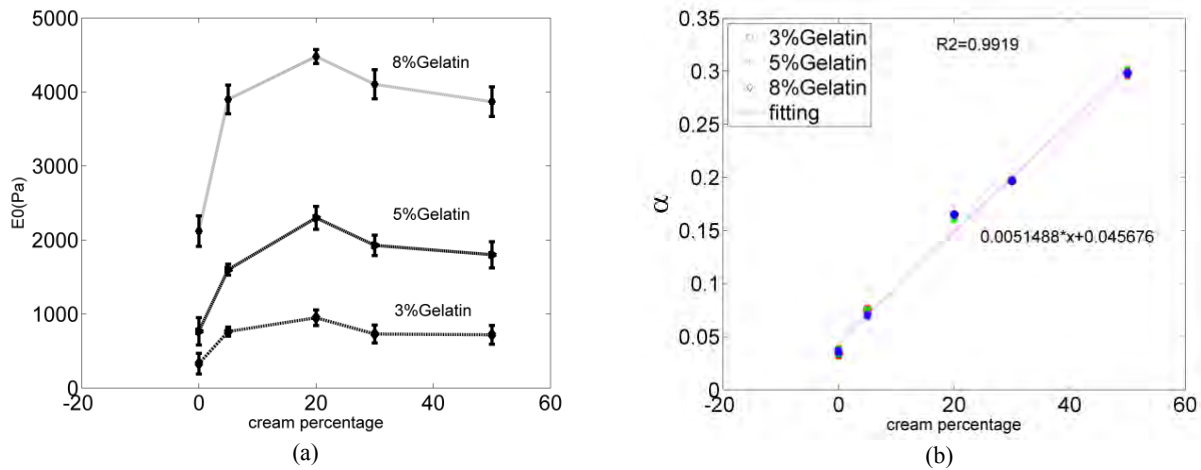


**Figure 5.3.** Estimates of  $E_0$  (a) and  $\alpha$  (b) versus sample Vanicream concentrations are shown. Parameters were obtained by fitting ramp-relaxation data to the KVFD model. The different curves in each plot are for different gelatin concentrations. On the right, the line labelled “fitting” is found from a linear regression to the data shown ( $R^2 = 0.992$ ). Each error bar indicates  $\pm 1$  sd obtained from measurements on six samples.

<sup>3</sup> There are well-known secondary effects that contribute to variations in  $E_0$  with cream concentration. For example, Vanicream is acidic ( $\text{pH} = 3.73$ ). Increasing gelatin acidity at high cream concentrations will soften the samples [27]. Thus, the downward trend in  $E_0$  at cream concentrations observed above 20% is expected.

*b) Derivative-order parameter  $\alpha$*

In Equation 4.3, the coefficient  $\alpha$  determines the “rate” of energy dissipation over time during the indentation process; more specifically the shape of the stress relaxation curve over time. For example, when  $\alpha$  is large, the energy dissipates quickly. Whereas, when  $\alpha$  is small, the energy dissipation is gradual. Therefore, in biphasic materials, the percentage of the freely flowing medium is related to  $\alpha$  [141] and the rate of energy dissipation. In solid viscoelastic materials,  $\alpha$  is also related to the connectivity of the solid matrix networks [138]. Higher connectivity will facilitate greater energy dissipation.

Figure 5.3(b) displays the measurements of  $\alpha$  versus cream concentration in gel-cream emulsion samples. The error bars for the measurements on six samples summarized by each plotted point are very small. It is seen that  $\alpha$  is proportional to cream concentration ( $R^2 = 0.992$ ). The linear regression line is plotted in the figure. The intercept of the line  $\alpha = 0.046$  is close to the  $\alpha$  estimated in pure gelatin. Although gelatin is often regarded as an elastic solid, it exhibits a small amount of time-dependency when deformed, which may come from protein crosslinks or hydrogen bonds breaking and reforming. The dramatic change of  $\alpha$  with cream percentage shows that the added cream component is the main source of energy loss during indentation process. Furthermore, the time required to dissipate the majority of the energy also shortens. Cream is added in replacement of water in the gel-cream compound. With the reduction of the tightly bounded water and gelatin macromolecules, the resistance on the cream decreases and it is easier for the fluidic component to relax. Therefore, as the cream is added,  $\alpha$  will increase.

In contrast, two-way ANOVA tests show there are no significant differences between gelatin concentrations ( $p = 0.82$ ), implying  $\alpha$  does not depend on gelatin concentration. Thus,

gelatin does not affect the rate of energy dissipation over time during the indentation process, only cream content and water content affect.

c) *Time constant  $\tau$  and viscous modulus  $\eta$*

The KVFD model of Equation 4.3 shows that  $\alpha$  and  $\tau$  combine with measurement time to predict the rate at which force relaxes through the scaled power-law factor  $(t/\tau)^{-\alpha}$ . For a given  $\alpha$ , relaxation time constant  $\tau$  is the other parameter that describes the time-dependent behavior. If we re-write Equation 4.3 with  $\eta = E_0\tau^\alpha$ , then  $\eta$  is proportional to the time-varying portion of stress per unit strain (Equation 5.2). Therefore,  $\eta$  can be called as viscous coefficient.

$$G(t) = E_0 \left( 1 + \frac{(t/\tau)^{-\alpha}}{\Gamma(1-\alpha)} \right) = E_0 + \eta \left( \frac{t^{-\alpha}}{\Gamma(1-\alpha)} \right) \quad (5.2)$$

Figure 5.4(a) shows that  $\tau$  increases only with cream percentage, reflecting the increased viscous relaxation of the emulsion. Figure 5.4(b) shows that  $\eta$  increases with both cream and gelatin concentration. With both  $\alpha$  and  $\tau$  being sensitive to cream concentrations, the mechanism could be quite different.  $\alpha$  is associated with the speed of internal energy dissipation, while  $\tau$  is the measurement of the quantity of the components or crosslinks that contribute to the mechanical energy loss. From Equation 5.2, it is speculated that the viscous coefficient  $\eta$  is linearly proportional to the total energy loss during indentation. In particular, normalizing the viscous coefficient by the shear modulus,  $\eta/E_0$ , eliminates the gelatin-concentration dependence, leaving only the time-dependent components of the material (Figure 5.4 (c)). It further demonstrates a unique relationship between  $E_0$  and gelatin concentration.

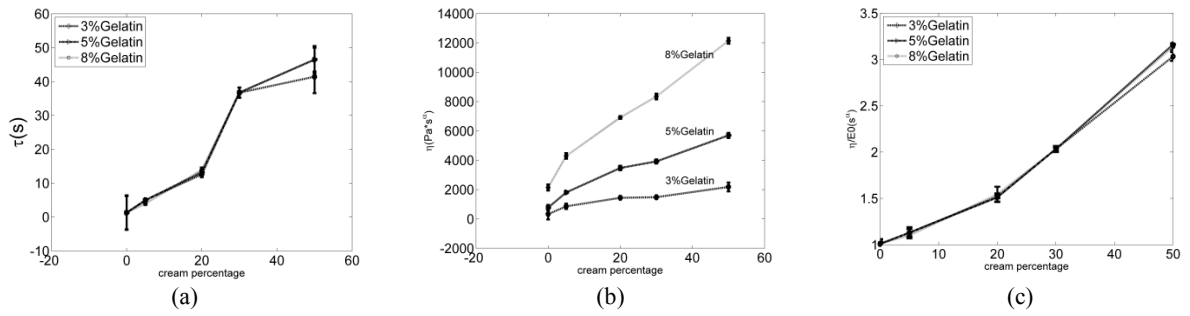


**Figure 5.4.** (a) The monotonic increase in KVFD parameter  $\tau$  with Vanicream concentration is essentially independent of gelatin concentration. (b) However, the increase in viscous modulus  $\eta$  with cream concentration does depend on gelatin concentration unless  $\eta$  is normalized by  $E_0$  (c). The error bars shown indicate  $\pm 1$  sd for measurements on six samples.

The following part demonstrates that the viscous coefficient  $\eta$  is linearly proportional to the energy loss during load-unload test. In Chapter 2.1.1, a measurement for energy loss was introduced from load-unload experiments to approximate the viscosity of a material. Numerical simulation was performed first to examine the possible correlation between viscous coefficient  $\eta$  and the loss-energy  $E_A$  calculated. Predictions were made for all combinations of three parameters when  $E_0$  was varied from 0.1 to 7.3 kPa,  $\alpha$  from 0.01 to 0.7 and  $\tau$  from 0.1 to 2500 s. These parameter ranges span those observed experimentally in the emulsion and liver-tissue samples. Figure 5.5 (a) shows that  $E_A$  is proportional to  $\eta$ , i.e.,  $E_A = k\eta$ , where the coefficient  $k = k(\alpha, T_r)$  depends on the material parameter  $\alpha$  and measurement parameter  $T_r$ . Each line in the plot is associated with one value of  $\alpha$ , such that combinations of  $E_0$  and  $\tau$  at fixed  $\alpha$  and  $T_r$  can be found along that line. The proportionality between viscosity  $\eta$  and loss energy  $E_A$  suggests that energy loss in a load-unload indentation experiment, that is the model-independent  $E_A$  is highly correlated

with the viscous coefficient in a ramp-hold experiment as described by  $\eta$  from the KVFD model. Figure 5.5(b) displays  $E_A$  versus  $\alpha$  for  $\eta$  fixed at  $800 \text{ Pa}\cdot\text{s}^\alpha$  and at four values of  $T_r$ . For each ramp time  $E_A$  peaks at a different value of  $\alpha$ . This is caused by the dramatic decrease of  $\Gamma(1 - \alpha)$  term in Equation 5.2 when  $\alpha$  increases. This can also be explained from the physics perspective. Note that mostly elastic media exhibit little or no frictional loss, i.e.,  $E_A(\alpha \rightarrow 0) \approx 0$ . Similarly, for a fluid where  $\alpha \rightarrow 1$ , frictional losses can be higher than those of elastic media but remain relatively low, especially for slower ramp speeds. Between the extremes, the parameter  $\tau$  that indicates the quantity of viscous components is powered by the rate of energy dissipation  $\alpha$ , and is amplified by the elasticity scaler, which predicts the total mechanical energy losses.

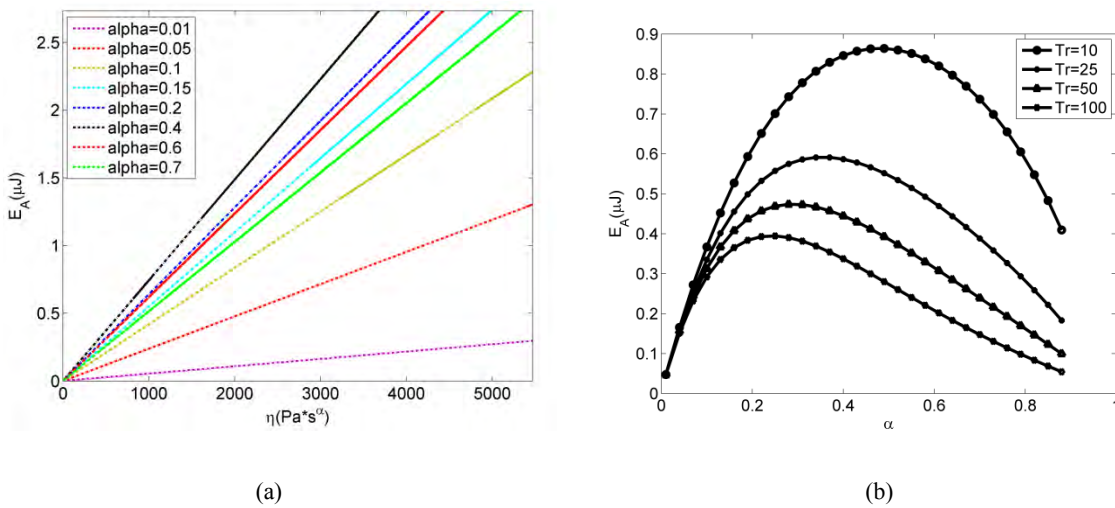


**Figure 5.5.** (a) The predicted relationship between viscous coefficient  $\eta$  and loss energy  $E_A$  is illustrated for eight values of  $\alpha$  between 0 and 1 at  $T_r = 25 \text{ s}$ . (b)  $E_A$  is plotted as a function of  $\alpha$  for four  $T_r$  values and at  $\eta = 800 \text{ Pa}\cdot\text{s}^\alpha$ . For both sets of plots, the maximum indentation depth was  $s_{\text{max}} = 1 \text{ mm}$ .

The above simulation was verified experimentally. Figure 5.6 displays measurements of  $E_A$  (points) acquired during load-unload experiments. These are plotted against separate measurements of  $\eta$  obtained from ramp-relaxation data. One set of samples was used for both measurements. Lines associated with the measurement points in the figure are predictions made using Equation 2.2 for the average  $\alpha$  measurement value. As predicted, measurements from samples with the same cream concentration (fixed  $\alpha$ ) but different gelatin concentrations fall along a straight line in the  $\eta$  versus  $E_A$  plane. Also predicted, the measured loss energy from a quasi-static load-unload experiment is linearly related to the viscous modulus computed from the KVFD model applied to ramp-relaxation experiments. One set of model parameters describes data from both experiments.

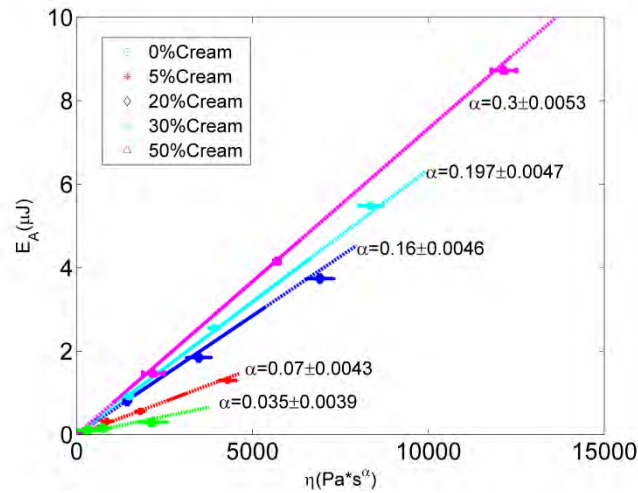


**Figure 5.6.** The predictions of Figure 5.5 (lines) are compared with measurements on gelatin-cream samples (points). Three gelatin concentrations, 3%, 5%, and 8%, at each of the five cream concentration indicated in the legend are shown. A fixed cream concentration establishes a line corresponding to  $\alpha$ , along which we find the three gelatin concentrations. Along each line, the 3% gelatin samples have the smallest  $E_A$  value while the 8% gelatin samples have the largest. Error bars indicate  $\pm 1$  s.d. for samples described in Table 5.2.

Table 5.2 shows the relative uncertainty in  $E_A$  given errors in  $\eta$  measurements applied in the predictive models. Values in the table are bias errors along with the two values in brackets that give the confidence intervals corresponding to  $\pm 1$  standard deviation (sd) for each  $\eta$  measurement. The measurement of energy loss is denoted by the caret  $\hat{E}_A$  to distinguish them from the predictions,  $E_A$ . To evaluate confidence intervals between measured and predicted values, the relative error is computed using

$$e_r = \frac{|\hat{E}_A - E_A|}{E_A} \quad (5.3)$$

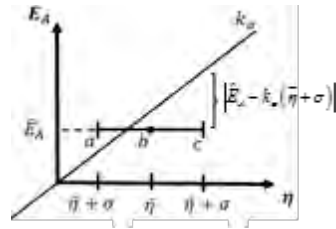
All bias errors are less than 20% and many are less than 5%; the notable exception being the elastic (pure-gelatin) samples. The smallest prediction errors occur in stiff viscoelastic samples.

The magnitudes of the relative errors and confidence intervals indicate that it is reasonable to use a pre-generated prediction plot to relate loss energy and viscous modulus parameters at least in these test samples. Consequently, either measurement can be made to estimate KVFD parameters.

**Table 5.2.** Prediction errors for energy loss in biphasic phantoms with different cream concentrations

$e_b[e_a, e_c]$	0%	5%	20%	30%	50%
3%	0.156 [0.103 0.369]	0.177 [0.031 0.321]	0.019 [0.046 0.083]	0.025 [0.046 0.096]	0.149 [0.103 0.196]
5%	0.173 [0.123 0.464]	0.026 [0.054 0.106]	0.066 [0.038 0.094]	0.025 [0.003 0.054]	0.008 [0.018 0.035]
8%	0.199 [0.083 0.314]	0.044 [0.009 0.078]	0.051 [0.036 0.066]	0.033 [0.019 0.047]	0.033 [0.020 0.047]

Fractional bias error is  $e_b = |\hat{E}_A - k_\alpha \bar{\eta}| / k_\alpha \bar{\eta}$  as shown in the figure, where  $\bar{\eta}$  is mean value. In brackets we display the confidence interval



In summary, the KVFD model parameters,  $E_0$ ,  $\alpha$ , and  $\tau$ , characterize respectively the elasticity, fluidity, viscosity of compressed biphasic emulsions in ramp-relaxation tests. These model parameters help explain the response of samples to the indentation technique in terms of sample components and molecular structure.  $E_0$  is shear modulus that quantifies material stiffness controlled primarily by gelatin concentration. At the cream-concentration range of 20-50%, emulsion stiffness does not significantly change, although secondary effects provide small systematic variations. Parameter  $\alpha$  indicates the intrinsic speed at which the emulsion internally dissipates mechanical energy as it relaxes the applied force toward an equilibrium state. In this study, it is proportional to the cream percentage due to the increased volume fraction of freely

flowing fluid as well as the decreased volume fraction of fixed water contained in the material. Time constant  $\tau$  is associated with the amount of cream or components in the material that contributes to the time-dependent behavior during the indentation tests. It is found that  $E_0$ ,  $\alpha$ , and  $\tau$  form a basis that spans the feature space for component characterization of these relatively simple emulsions. Interestingly, a derived parameter from these three bases  $\eta = E_0\tau^\alpha$  is shown to contain the same information as the widely used energy loss metrics in hysteresis loop. The total mechanical energy losses as heat can be predicted through the parameter  $\tau$  that indicates the quantity of viscous components, powered by the rate of energy dissipation  $\alpha$ , and amplified by the elasticity scalar.

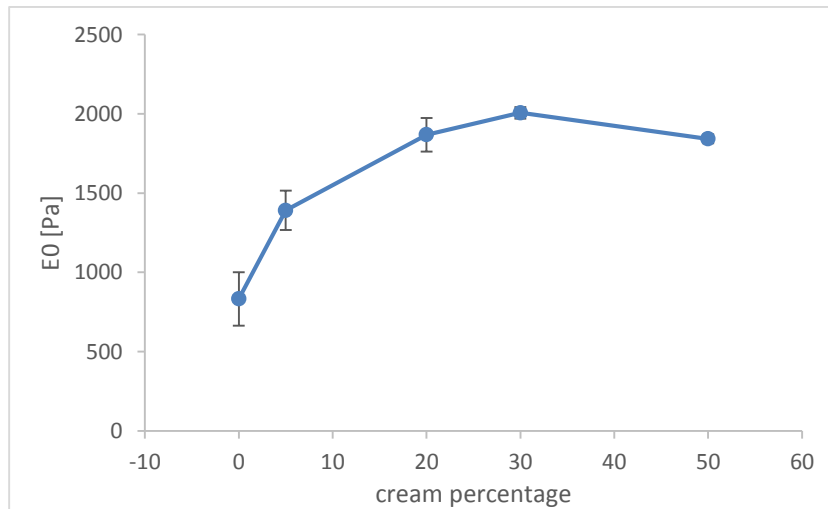
### **5.2.2 High frequency wave imaging measurements**

Equation 5.1 and Equation 2.10 combined together will give the dispersion curve defined by KVFD model parameters. Fitting the same model to the measurements from two drastically different frequency responses may or may not yield the same parameter estimates. For elasticity related parameters, the two techniques should not yield different estimates since elastic coefficient  $E_0$  is not frequency dependent. For time-dependent properties, the consistency of the parameters depends on whether the same viscous or fluidic responses can be collected by different techniques. The high frequency technique is not sensitive to components that have relaxation time constant  $\tau$  that is larger than several seconds (e.g., freely flowing fluid). Instead, it is more sensitive to the crosslinks and electrostatic bonds which have a much shorter relaxation time constant.

For the dynamic wave imaging technique, only 5% gelatin samples were used (G5C0, G5C5, G5C20, G5C30, G5C50).

a) Elastic parameter  $E_0$

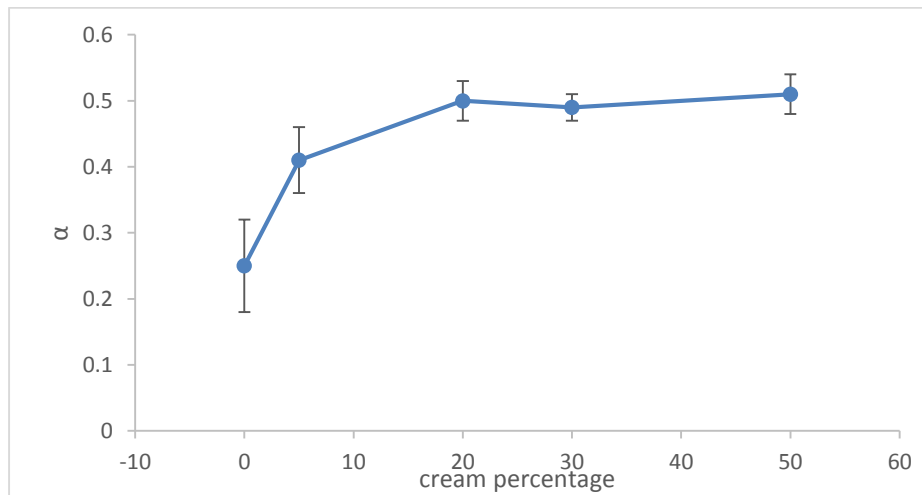
Figure 5.7 shows the estimation results from samples with five different cream concentrations and the same gelatin concentration. Compared with results in Figure 5.3, ANOVA test shows no significant difference of the measurements between  $E_0$  measurements from the two techniques. The elastic modulus measured by applications of the KVFD model on indentation technique and dynamic wave imaging technique are very close. Like in indentation technique, it also predicts the initial stiffening effect when the cream is added. This proves that  $E_0$  is not a parameter that depends on force frequency. Therefore, the KVFD model parameter  $E_0$  still approximates the shear modulus for high frequency techniques.



**Figure 5.7.** Estimates of  $E_0$  versus sample Vanicream concentrations using dynamic wave imaging technique. Parameters were obtained by fitting dispersion data (200 Hz ~ 5000 Hz) to the KVFD model. Each error bar indicates  $\pm 1$  sd obtained from measurements on six samples.

b) Derivative-order parameter  $\alpha$

In Equation 5.1,  $\alpha$  determines the overall shape of the storage modulus  $G'$  and loss modulus  $G''$ . Figure 5.9 shows the different behaviors of  $G'$  and  $G''$  when  $\alpha$  varies. When  $\alpha = 1$ ,  $G'$  is a constant, and  $G''$  is a straight line, which is in accordance with the Kelvin-Voigt model prediction (Figure 5.9(e)). When  $\alpha \rightarrow 0$ ,  $G'$  is also a constant, and  $G''$  is approximately zero (Figure 5.9(a)). Between two extremes,  $\alpha$  controls the rate at which  $G'$  and  $G''$  changes with frequency. When  $\alpha$  is between 0~0.5, the increase rate of  $G'$  is greater than the increase rate of  $G''$  (Figure 5.9(b)), and when  $\alpha$  is between 0.5~1, the increase rate of  $G''$  exceeds that of  $G'$  (Figure 5.9(d)). When  $\alpha = 0.5$ ,  $G'$  and  $G''$  increase in parallel (Figure 5.9(c)). Usually, the change of  $\alpha$  is due to some internal structural changes of solid matrix networks [143], which would change the energy dissipation patterns.



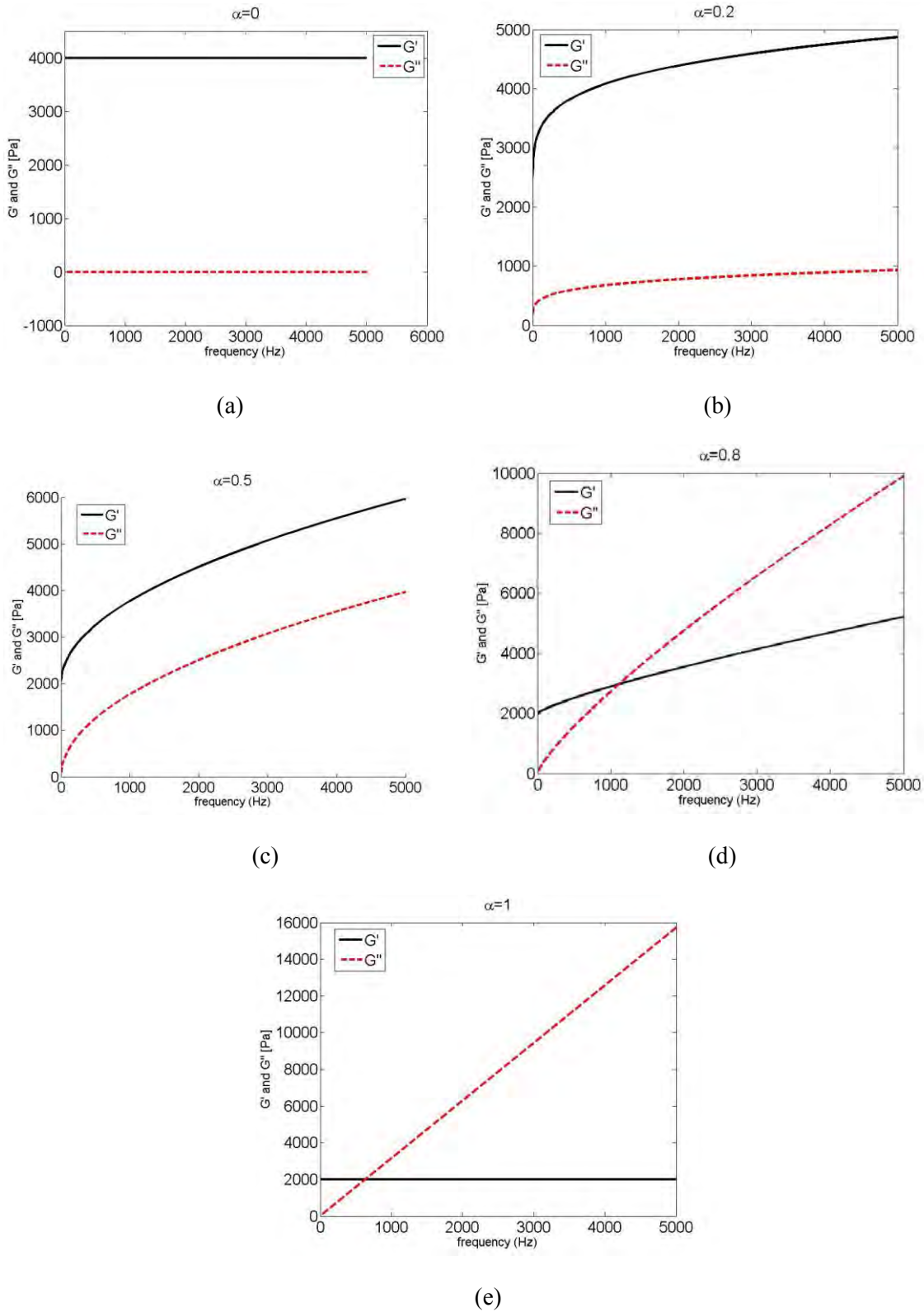
**Figure 5.8.** Estimates of  $\alpha$  versus sample Vanicream concentrations using dynamic wave imaging technique. Parameters were obtained by fitting dispersion data (200 Hz ~ 5000 Hz) to the KVFD model. Each error bar indicates  $\pm 1$  sd obtained from measurements on six samples.

Figure 5.8 shows the estimates of  $\alpha$  versus cream concentrations using dynamic wave imaging technique. In contrast to the linear behavior in indentation estimates shown in Figure 5.3(b), the  $\alpha$  estimates increase initially and plateau at  $\alpha = 0.5$ . The difference can be explained as the fluidity from the cream plays a dominant role in dissipating energy in low frequency indentation technique, while in the high frequency technique, fluidity is negligible due to the small strain applied in short periods. Under these conditions, hydrogen and electrostatic bonds (crosslinks) determine viscous behavior. Therefore the molecular structure of the solid matrix network will affect the energy dissipated [143].

The introduction of cream into the gelatin hydrogel system will cause some internal rearrangement of protein and fluid components initially when cream is first introduced, but the effects stabilize after the cream concentration exceeds 10%~20% of the sample mass.

*c) Time constant  $\tau$  and viscous modulus  $\eta$*

The parameter  $\tau$  is defined as  $\tau = \frac{\mu_2}{\mu_1}$ . From Figure 5.10, it is seen that the trend of  $\tau$  is similar to  $\alpha$ . It reaches some equilibrium after the cream concentration exceeds 20% of the sample volume. I suspect that the addition of Vanicream mass has some effects on the distribution and density of gelatin crosslinks. The parameter  $\eta$  is defined as  $\eta = \mu_1 \left( \frac{\mu_2}{\mu_1} \right)^\alpha = \mu_1 \tau^\alpha$ . Similar to the low frequency technique,  $\eta$  is a combination of  $\mu_1$ ,  $\tau$  and  $\alpha$ , which is proportional to the total energy dissipated. Figure 5.10 shows there is no significant change of the total energy loss as the cream concentration increases.



**Figure 5.9.** Simulation of the behavior of storage modulus ( $G'$ ) and loss modulus ( $G''$ ) when  $\alpha$  varies between 0 and 1. Frequency range (0 ~ 5000 Hz) is the same as examined in experiments.

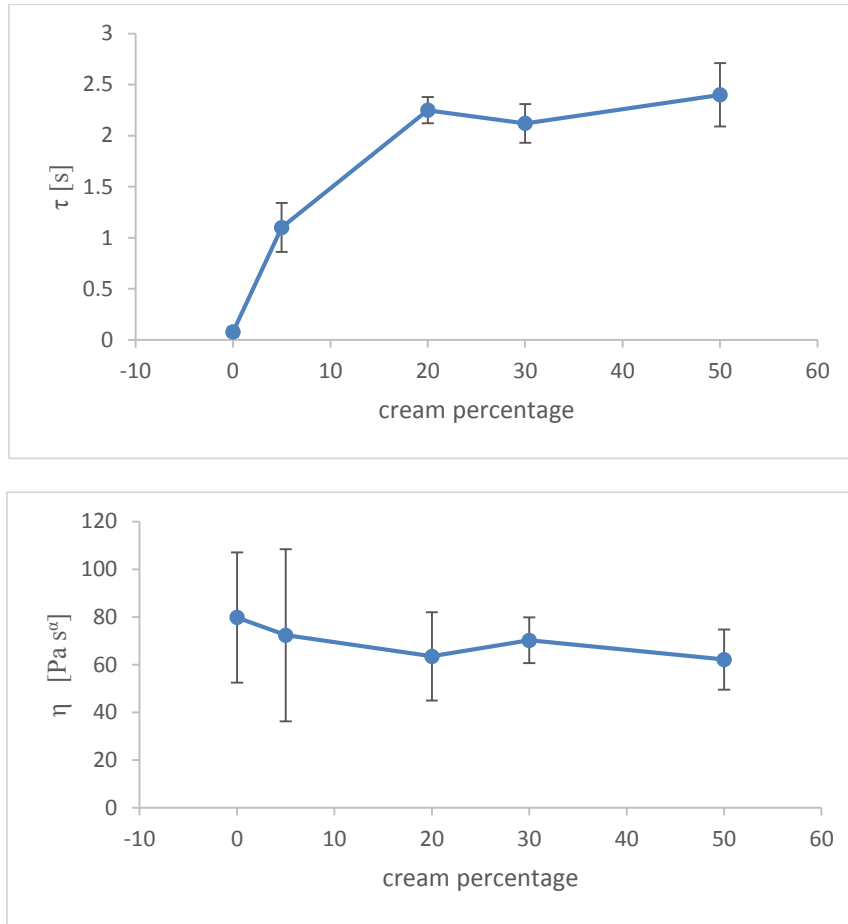


**Figure 5.10.** Estimates of  $\tau$  (upper) and  $\eta$  (lower) versus sample Vanicream concentrations using dynamic wave imaging technique. Parameters were obtained by fitting ramp-relaxation data to the KVFD model. Each error bar indicates  $\pm 1$  sd obtained from measurements on six samples.

### 5.3 KVFD model parameters change during liver hyperthermia and ablation

Given the above analysis of KVFD model parameters in emulsion samples, it is now prepared to extend the analysis to ex vivo liver-tissue samples. Of course, liver is compositionally and structurally much more complicated than the two-component gel-cream samples. However, it is also well known that heating liver tissue will systematically stiffen the tissue [144, 145, 146,

147, 148], which is somewhat analogous to changing gelatin concentration in the gelatin-cream samples. Frozen pig livers were obtained from a local market and completely thawed in air over several hours. Measurements were made on ex vivo samples at room temperature within 6 h of thawing. Samples roughly  $40 \times 30 \times 15 \text{ mm}^3$  in size were cut from organ regions lacking major vasculature or ducts. Some specimens were tested without further processing and others after being heated at 45 °C, 55 °C, or 65 °C for 40 min. After heating, samples were placed in isotonic saline at room temperature for at least 45 min before indentation.

A major medical application of liver-tissue heating is curative nonsurgical treatments of hepatocellular carcinoma. Liver tissues are locally heated in patients using percutaneous radiofrequency ablation, microwave ablation, or high-frequency ultrasound (HIFU) ablation techniques [149, 150]. Heating liver to 45 °C for 30-60 min irreversibly damages cells, inhibiting DNA replication and energy-producing mitochondrial function [150]. Faster heating to temperatures above 60 °C causes irreversible protein denaturation, which is also cytotoxic, leading to coagulative cellular necrosis. Besides cellular damage, protein structure is changed, altering the extracellular matrix in ways that can be sensed through macroscopic mechanical testing [146, 147]. Porcine liver samples were heated in saline for 40 min at 45 °C, 55 °C, or 65 °C before cooling the tissue for 45-60 min in room temperature saline prior to mechanical testing.

Indentation measurements for thermally-damaged liver are compared with those of fresh liver in Figure 5.11 and Table 5.3. As with the gel-cream samples,  $\eta$  was measured as a function of  $E_0$ ,  $\alpha$ ,  $\tau$  using ramp-relaxation experiments and fit those data to the KVFD model to estimate model parameters.  $E_A$  was also measured using load-unload experiments.  $T_r = 25 \text{ s}$  was applied to all liver measurements. Mean values are plotted against each other in Figure 5.11. The last line in Table 5.3 lists the errors and the confidence intervals that are expected when predicting loss

energy from the KVFD parameters. The error bars in plots summarizing liver-tissue measurements are standard deviations of three measurements made on one liver sample acquired at different locations (assuming liver tissue is isotropic). These results are based on the paper [137] which is in preparation.

Dynamic wave imaging measurements for the thermally-damaged liver are listed in Table 5.4. The error bars in the table summarizing liver-tissue measurements are standard deviations of three measurements made on one liver sample acquired at different locations (assuming liver tissue is isotropic).

**Table 5.3.** Ex Vivo Liver sample Measurements using ramp-relaxation

	fresh	heated 45°C	heated 55°C	heated 65°C
$E_0$ (Pa)	75 ± 11	188 ± 22	4150 ± 368	7398 ± 587
$\alpha$	0.41 ± 0.01	0.35 ± 0.007	0.27 ± 0.005	0.27 ± 0.004
$\tau$ (s)	103 ± 12	850 ± 71	2300 ± 106	2500 ± 127
$\eta$ ( $\times 10^4$ Pa-s <sup>a</sup> )	0.050 ± 0.020	0.199 ± 0.051	3.38 ± 0.313	5.98 ± 0.437
$E_A$ ( $\mu$ J)	0.289 ± 0.033	1.36 ± 0.099	24.5 ± 0.98	42.6 ± 2.14
$e_b[e_a, e_c]$	0.224 [0.142 0.382]	0.130 [0.092 0.224]	0.023 [0.008 0.015]	0.004 [0.003 0.003]

\* Note that shear-modulus values for liver are about 30 times less than typical literature values, e.g., [145], which we attribute to the small sample size.

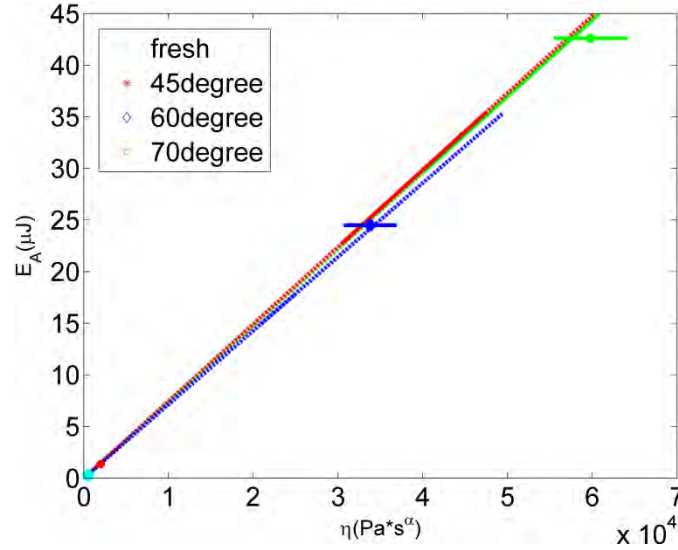


**Figure 5.11.** Similar to Figure 5.6, we plot indentation measurements of  $E_A$  versus  $\eta$  for ex vivo liver samples. The cyan circle marker near the origin is the result for fresh liver. The red star marker also near the origin indicates results for liver heated to 45°C for 40 min. The blue diamond and green hexagram markers indicate measurements for liver heated to 55 °C and 65 °C, respectively, also for 40 min. Error bars along both axes indicate  $\pm 1$  sd in  $\eta$  and  $E_A$  measurements. The lines are for values of  $\alpha = 0.41, 0.35, 0.27$ , found from ramp- relaxation measurements.

**Table 5.4.** Ex Vivo Liver sample Measurements using dynamic wave imaging

	fresh	heated 45°C	heated 55°C	heated 65°C
$\mu_1$ (Pa)	206 ± 76	473 ± 56	2842 ± 265	5384 ± 1574
$\alpha$	0.42 ± 0.05	0.45 ± 0.07	0.65 ± 0.05	0.62 ± 0.03
$\tau$ ( $\times 10^{-3}$ s)	1.02 ± 0.11	6.80 ± 1.26	11.01 ± 1.62	5.5 ± 1.17
$\eta$ (Pa·s $^\alpha$ )	11.43 ± 1.22	50.11 ± 8.28	151.67 ± 25.1	215.16 ± 68.3

Table 5.3 and 5.4 summarizes the results of fitting the KVFD model to ramp-relaxation data from indentation and dispersion data from ARF-OCE respectively. For  $E_0$  measurements, thermal damage clearly modified the parameters. Generally, higher heating temperatures dramatically increase  $E_0$ . However, the elasticity parameters  $E_0$  and  $\mu_1$  measured for the two techniques do not agree with each other. This may be due to the experimental conditions that liver samples were submerged in saline during indentation, causing looseness at the surface of the sample. It is found that liver stiffness increases significantly between 45 °C and 55 °C in both measurements, suggesting a major change in mechanical properties has taken place. Other investigators [148, 150] reported that heating liver above 55-60°C irreversibly transforms extracellular collagen from its normal helical state to a random state, and this change in molecular structure leads to increased collagen crosslinking that is likely to increase stiffness and viscosity [148]. In the same temperature range,  $\alpha$  and  $\tau$  change very little, due to the extracellular collagen denatures to expose charged sites that form a higher density of elastic crosslinks.

For fractional order measurements, the indentation technique predicts that  $\alpha$  decreases during the heating process until 55°C. The energy dissipation takes longer time as the material solidifies (fluid content decreases). Once the major structural transformation is complete,  $\alpha$  stabilizes. On the other hand, the high frequency shear wave imaging technique, which is more sensitive to solid matrix changes than fluidity changes, shows a significant increase in  $\alpha$  after the major structural transformation around 45 °C to 55 °C.

For viscous coefficient measurements, the modest increase in  $\eta$  during liver heating is partially driven by the increase in  $E_0$ , recalling that  $\eta = E_0\tau^\alpha$ . Hence, the greater stiffening of the liver at higher temperatures means that thermally-damaged liver behaves increasingly as a lossy

viscoelastic solid. These changes are consistent with changes in the chemical structure of the collagen matrix being responsible for increased  $E_A$ . Also, the viscosity is consistently increasing as well.  $\tau$  changes drastically at this temperature, probably coming from the suddenly increased number of viscous interactions and chemical bounds due to protein denaturing.

Any changes observed in thermally-damaged ex vivo liver could be different when measured in vivo. The effects of blood perfusion, at the very least, modify the temperature distribution in ablative therapy where tissue temperatures quickly rise above 80 °C and fall as blood perfusion cools the region. The rates of tissue heating and cooling will most certainly have an effect on mechanical properties. The point in this study is to show that KVFD model parameters can explain the effects of thermal damage in liver tissue. However, statements regarding the utility of mechanical properties for indicating therapeutic changes to liver require in vivo studies to account for perfusion.

## 5.4 Summary

The KVFD model provides a three-dimensional feature space of mechanical properties that properly characterizes the composition and structure of biphasic emulsions. Two different frequency techniques each produce the same elasticity parameter when the KVFD model is applied, and the values found are approximately equal to the shear modulus. The two techniques yield different values for  $\alpha$  and  $\tau$  due to the different energy dissipation mechanisms occurring at these different force-frequency bandwidths. In both experiments,  $\alpha$  is related to the energy dissipation rate that is sensitive to the internal structure as well as any molecular and micro-structural changes occurring in the solid network. Theory shows that the response of tissue to mechanical stimuli is a

power law in time (indentation) and frequency (shear wave), with exponent  $\alpha$ . In indentation, where fluid is the main source of energy dissipation,  $\alpha$  and  $\tau$  are closely related to cream concentration. While, in shear wave imaging, energy dissipation is mainly caused by the breaking and reforming of electrostatic and hydrogen bonds in collagen. The difference in the sources of energy dissipation suggests that it should not be surprising that  $\alpha$  measurements vary between the two measurement techniques. Estimation of  $\alpha$  at high force frequencies is more likely to represent crosslink formation and ECM structural changes. Another derived KVFD parameter  $\eta$  is a good approximation of the total energy loss when there is little change in  $\alpha$ . Numerical simulations suggest that the viscosity modulus  $\eta$  and a loss energy  $E_A$  (energy lost during quasi-static force-displacement cycles, which is considered a good metrics for the viscoelastic property of the solid matrix) has a linear relationship, and the slope of the linear relation is determined by fractional order  $\alpha$ . Experimental measurements from phantom and tissue data both show good agreement with the theoretical prediction of  $\eta - E_A$  relation.

Based on the emulsion sample analysis, I then carried out a study on ex vivo liver tissue. Liver samples were heated in a water bath at different temperatures to induce different changes inside the tissue. The KVFD model is found very promising because the parameters described changes caused by thermal damage that were consistent with results in the literature. Elasticity measurement can predict the stiffening of the tissue during heating. Both  $\alpha$  and  $\tau$  are sensitive to the major structural transformation that happens around 45 °C to 55 °C. However, tissue is much more complicated than the two-component phantom. The disagreement of  $E_0$  at low and high frequencies may suggest a higher order FD model (more than one fractional order parameter [151]) is needed to represent responses from multiple elastic components and multiple viscous components.

From these combined results, it is concluded that KVFD model parameters form a concise features space for biphasic medium characterization that describes time-varying mechanical properties. It supports techniques with a wide range of load frequencies. The response from each technique will be sensitive to a set of medium components and related molecular structures. Finding techniques that are sensitive to changes in normal tissue will help diagnosis.

The KVFD model can be applied in medical elasticity imaging, where images formed based on these features can be interpreted in terms of disease processes or treatment-induced effects. Biphasic phantom and *ex vivo* liver results show that it can provide much more details about tissue components and structures than other rheological models I tried. Future work would be to evaluate the necessity of using higher order fractional derivative models for tissue, and to identify the relationship between the model parameters and tissue components, structures and crosslinks with the aid from more quantitative biological measurements such as histology.

## CHAPTER 6: CONCLUSIONS AND FUTURE WORK

### 6.1 Summary and Conclusions

Mechanical properties of soft biological tissues have been studied extensively with the hope of enriching our collective understanding of how tissue composition and structure influence the mechanical properties that guide cellular behavior [6, 19, 44, 152, 153]. Tissue deformation patterns resulting from applied force stimuli can reveal properties of the tissue mechano-environment that can improve our understanding of the overall biological function and behavior of living systems. Additionally, responses from different force stimuli could arise from different selections of tissue structural components (i.e. ECM crosslinks, fluids, viscoelastic proteins), and the appropriate data-reduction models could transform these responses into intrinsic tissue properties. Therefore, to exploit the diagnostic potential of mechanical characterization, one must identify the combinations of measurement techniques and models that provide consistent parametric estimates that are sensitive to diagnostic microscopic features of tissue. The objective of this thesis is to develop a foundation on which the measurement techniques, data-reduction modeling, and biological interpretation can be studied in an integrated manner.

Several techniques facilitate assessing tissue mechanical properties, of which indentation techniques are the most recognized and widely used for basic science investigations due to the simplicity and low cost. In recent years, elastography imaging technologies, which enable measurement of tissue mechanical properties *in vivo*, have been growing rapidly for clinical studies. Both classes of techniques have the potential of accurately mapping the elastic modulus and viscoelastic properties in research labs and in clinic applications. However, few people have ever unified the measurements from different classes of techniques. Three techniques were

developed for characterizing tissue viscoelastic properties based on indentation, ultrasound, and optical coherence tomography respectively. Each technique has its unique force frequency range, and each has been validated individually through numerical simulations, phantom experiments and tissue trials. When the physical assumptions on which a technique is established are violated, often due to the limited size of the sample, bias could be introduced to the measurements. Corrections are applied to minimize the bias, such as the adoption of a new physical model (i.e., Dimitriadis model, Lamb wave equation) or preprocessing of the responses (i.e., directional filters). It has been shown that the three techniques can yield the same Young's modulus estimates for gelatin phantoms with various stiffnesses if the assumptions intrinsic to each technique are not violated. This not only verifies the reliability of each technique, but also suggests that there is an "intrinsic" elastic modulus of a material that can be obtained independent of the technique used, even at drastically different load frequencies.

However, once the mechanical behavior of the material shows time-dependency or frequency-dependency, rheological models must be included in the analysis to provide parametric estimates that summarize those features. The experimental data shows that simple viscoelastic models such as Kelvin-Voigt model, Maxwell model, and Zener model all have limitations. They do not describe long time-duration data or data acquired when the applied load has a broad frequency range, and also are restricted to certain material types. Instead of adding more terms to these integer-derivative models, the Kelvin-Voigt fractional derivative (KVFD) model is adopted. The KVFD model is suitable for complex materials with multiple composites or compartments, which would otherwise require a separate model term for each compartment individually. It represents the measurement data of a broad range in both time and frequency domain with a small

number of parameters, and yields stable estimates for many types of phantoms and tissues. It is superior to integer derivative models for the materials and techniques used in this study.

Moreover, the KVFD model provides a three-dimensional feature space of mechanical properties that properly characterizes the composition and structure of biphasic emulsions. To explore this correlation, tissue-like emulsions with varying elastic and viscous coefficients were developed, consisting of known proportions of gelatin and cream. It is found that the KVFD parameter  $E_0$  is approximately equal to the shear modulus, no matter which technique is used. This agrees with the previous finding that elastic modulus of a material can be obtained independently of the technique. It is also found that the other two parameters  $\alpha$  and  $\tau$  are closely related to energy dissipation. In particular,  $\alpha$  is related to the presence of energy-absorption components; it determines the rate of energy dissipation. Parameter  $\tau$  is related to the quantity of energy-absorption components. In indentation, the cream is the major energy dissipation component. In high-frequency shear wave imaging techniques, energy dissipation is mainly caused by the breaking and reforming of electrostatic and hydrogen bonds in collagen. Therefore,  $\alpha$  and  $\tau$  are most sensitive to cream percentages when indentation techniques are applied.

This knowledge about KVFD parameters is then applied to monitor the transformation of tissue microenvironment in thermally damaged ex vivo liver. Estimates of  $E_0$  predict the slight increase in liver stiffening as temperature begins to increase, and a substantial increase in stiffness above 55°C. The sudden transition above 55°C is a reflection of the increased number of covalent crosslinks due to the irreversible structural changes in collagen molecules caused by heating the tissue. Estimates of  $\alpha$  from indentation testing have shown a continuous decrease until 55 °C. The same tissue samples imaged using shear wave technique have shown a sudden increase of  $\alpha$  at

around 55 °C. It is in accordance with the reports that irreversible damage of the cells happens around 45 °C, and irreversible protein denaturation happens around 50 °C ~ 60 °C. Cell damage together with fluid solidification will influence  $\alpha$  measured from low frequency technique; and protein denaturation will alter the electrostatic and hydrogen bonds of ECM, and thus affecting  $\alpha$  measured from high frequency technique. A derived parameter from these three basic parameters  $\eta = E_0\tau^\alpha$  is a metric to predict the total energy loss, since it is shown in the experiments to correlate linearly with the energy loss in hysteresis loop.

The correlation of the KVFD model parameters with tissue components and microstructures sheds light on the retrieving of information about biological systems using mechanical characterization techniques. It will lead to an improved understanding of how components interact to influence mechanical behavior of living systems. Different characterization techniques may probe different tissue components depending on the mechanism of the stimuli.

In summary, I achieved the goal of finding combinations of measurement techniques and rheological models that reveal tissue microscopic features that potentially contain diagnostic information. Three techniques were developed. Each offers strengths in a large variety of applications and it is sensitive to a different set of viscous components in tissue. KVFD model was found to be appropriate in representing the experimental data, as well as providing parameters that reflect the contrast of elastic and viscous components. The combinations of techniques and KVFD model have great potential to be able to separate healthy and pathological tissues described by the histological features. This work demonstrates three techniques, one of the rheological models and the correlation of the obtained model parameters with tissue components and structures. However, one can use the same framework for other technique-model combinations. The future for diagnostic imaging techniques continues to brighten as we gain knowledge on the relationship

between mechanical parameters and specific tissue features. The evolution of this field has the potential to bridge molecular, cellular, and tissue biology and lead to new approaches in the treatment of patients, linking these pathological changes to the exact mechanical behavior at a mesoscale tissue level larger than the cell but smaller than the organ.

## 6.2 Future work

### *1) Imaging techniques*

All conclusions drawn in this thesis are subjected to an assumption: the material is homogeneous. However, all tissues exhibit anisotropic and heterogeneous properties at different levels. It still needs to be studied on how reliable results of the two imaging techniques will be for heterogeneous tissue samples. Resolution is another topic for further study, given that the region of interest in tissue is usually small in size. The mechanical resolution of the imaging techniques will define the limits of the techniques in clinic practice.

Although the concept of mechanical resolution is unclear in this field, it is obvious that large shear wavelength would render low mechanical resolution. In tissue experiments, small wavelength always means high frequency, low signal quality and very limited propagation distance due to high attenuation coefficient. There is a tradeoff between mechanical resolution and signal to noise ratio when shear wave based techniques are used. If high resolution (less than 1 micrometer) is required in practice, other excitation techniques such as ARFI [28] are also available.

## *2) Rheological modeling*

In the frequency domain, KVFD model represents the dispersion curves very well (Figure 5.2). However, it is not guaranteed that model predicted storage modulus ( $G'$ ) and loss modulus ( $G''$ ) match the measured  $G'$  and  $G''$ . In this study,  $G'$  and  $G''$  as a function of frequency were not obtained directly from the experiments to make this comparison. To verify that KVFD is the best representative rheological model,  $G'$  and  $G''$  curves are needed to be represented by the model simultaneously.

The disagreement between  $E_0$  measured by two techniques invokes some questions about the insufficiency of the KVFD model. People have been using a higher order fractional derivative model with one additional fractional order  $\beta$  [151]. The rationale is that if there are two viscous components causing energy dissipation at different rates, then two fractional orders will correspond to the two components respectively. The behavior of  $G'$  and  $G''$  may facilitate the identification of the necessity for higher order models.

## *3) Biological Interpretation*

As shown in Chapter 5, tissue-like materials can enable us to interpret the relationship between medium components and model parameters. However, the two-component phantom (gelatin-cream) is still too simple to guide tissue investigations. Tissue properties are determined in part by fluid movement in the open- and closed-cell compartments found within a viscoelastic collagen matrix that is actively maintained by the embedded cells to meet programmed needs. In future work, a multi-component phantom with more than one viscous component will be

constructed. For tissue correlation studies, characteristic histology and other quantitative biological measurements should also be included to perform the correlation analysis with modulus coefficients.

## REFERENCES

- [1] Butcher DT, Alliston T, Weaver VM. A tense situation: forcing tumour progression. *Nat Rev Cancer*. 2009 Feb;9(2):108-22.
- [2] Guillot C, Lecuit T. Mechanics of epithelial tissue homeostasis and morphogenesis. *Science*. 2013 Jun 7;340(6137):1185-9
- [3] Krishnan KM. Biomedical Nanomagnetism: A spin through possibilities in imaging, Diagnostics, and Therapy. *IEEE Trans Magn*. 2010 Jul 1;46(7):2523-2558.
- [4] de Ledinghen V, Vergniol J, Barthe C, Foucher J, Chermak F, Le Bail B, Merrouche W, Bernard PH. Non-invasive tests for fibrosis and liver stiffness predict 5-year survival of patients chronically infected with hepatitis B virus. *Alimentary Pharmacology & Therapeutics* 2013;37(10): 979-88.
- [5] Fleury E, Fleury JSV, Piato S, Roveda D. New elastographic classification of breast lesions during and after compression. *Diagn Interv Radiol*. 2009;15: 96–103.
- [6] Samani A, Zubovits J, Plewes D. Elastic moduli of normal and pathological human breast tissues: an inversion-technique-based investigation of 169 samples. *Physics in Medicine and Biology*. 2007;52(6):1565-76.
- [7] Mahmud A, Feely J. Arterial stiffness is related to systemic inflammation in essential hypertension. *Hypertension*. 2005;46(5):1118-22.
- [8] Butcher DT, Alliston T, Weaver VM. A tense situation: forcing tumour progression. *Nature Reviews Cancer*. 2009;9(2):108-22.
- [9] Bergamaschi A, et al. Extracellular matrix signature identifies breast cancer subgroups with different clinical outcome. *J Pathol*. 2008 Feb;214(3):357-67.
- [10] Buganza Tepole A, Ploch CJ, Wong J, Gosain AK, Kuhl E. Growing skin - A computational model for skin expansion in reconstructive surgery. *J. Mech. Phys. Solids*, 2011;59:2177-2190.
- [11] Hoffler CE, Guo XE, Zysset PK, Goldstein SA. An application of nanoindentation technique to measure bone tissue Lamellae properties. *J Biomech Eng*. 2005 Dec;127(7):1046-53.
- [12] Fei Liu, Daniel J. Tschumperlin, Micro-mechanical characterization of lung tissue using atomic force microscopy. *J Vis Exp*. 2011 Aug 28;(54).
- [13] Oyen ML. Nanoindentation of biological and biomimetic materials. *Experimental Techniques*. 2011; 37:73–87.
- [14] Ophir J, Céspedes I, Ponnekanti H, Yazdi Y, Li X. Elastography: a quantitative method for imaging the elasticity of biological tissues. *Ultrasonic Imaging*. 1991;13(2):111–134
- [15] Qiu Y, Sridhar M, Tsou JK, Lindfors KK, and Insana MF. Ultrasonic viscoelasticity imaging of nonpalpable breast tumors: preliminary results. *Academic Radiology*, 2008;15(2):1526-1533.
- [16] Tanter M, Bercoff J, Athanasiou A, et al. Quantitative assessment of breast lesion viscoelasticity: initial clinical results using supersonic shear imaging. *Ultrasound Med. Biol*. 2008;34(9):1373–1386

- [17] Kemper J, Sinkus R, Lorenzen J, Nolte-Ernsting C, Stork A, Adam G. MR elastography of the prostate: initial *in-vivo* application. *Rofo*. 2004;176(8):1094–1099.
- [18] Sinkus R, Tanter M, Xydeas T, Catheline S, Bercoff J, Fink M. Viscoelastic shear properties of *in vivo* breast lesions measured by MR elastography. *Magn. Reson. Imaging*. 2005;23(2):159–165.
- [19] Huwart L, Sempoux C, Salameh N, et al. Liver fibrosis: non-invasive assessment with MR elastography. *NMR Biomed*. 2006;19(2):173–179.
- [20] Palmeri ML, Wang MH, Dahl JJ, Frinkley KD, Nightingale KR. Quantifying hepatic shear modulus *in vivo* using acoustic radiation force. *Ultrasound Med. Biol*. 2008;34(4):546–558.
- [21] Chen S, Urban M, Pislaru C, et al. Shearwave dispersion ultrasound vibrometry (SDUV) for measuring tissue elasticity and viscosity. *IEEE Trans. Ultrason. Ferroelectr. Freq. Control*. 2009;56(1):55–62.
- [22] Bercoff J, Tanter M, Fink M. Supersonic shear imaging: a new technique for soft tissue elasticity mapping. *IEEE Trans. Ultrason. Ferroelectr. Freq. Control*. 2004;51(4):396–409.
- [23] Chaturvedi P, Insana MF, Hall TJ. 2-D Companding for noise reduction in strain imaging. *IEEE Transactions on Ultrasonics Ferroelectrics and Frequency Control*. 1998;45(1):179-91.
- [24] Sridhar M, Liu J, Insana MF. Elasticity imaging of polymeric media. *Journal of Biomechanical Engineering-Transactions of the ASME*. 2007;129(2): 259-72.
- [25] Kennedy BF, Koh SH, McLaughlin RA, Kennedy KM, Munro PR, Sampson DD. Strain estimation in phase-sensitive optical coherence elastography. *Biomedical Optics Express*. 2012 Aug 1;3(8):1865-79.
- [26] McGrath DM, Foltz WD, Al-Mayah A, Niu CJ, Brock KK. Quasi-static magnetic resonance elastography at 7 T to measure the effect of pathology before and after fixation on tissue biomechanical properties. *Magn Reson Med*. 2012 Jul;68(1):152-65.
- [27] Yapp RD, Insana MF, “pH-induced contrast in viscoelasticity imaging of biopolymers”. *Phys Med Biol*. 2009 Mar 7;54(5):1089-109..
- [28] Palmeri ML, Dahl JJ, MacLeod DB, Grant SA, Nightingale KR. On the feasibility of imaging peripheral nerves using acoustic radiation force impulse imaging. *Ultrason Imaging*. 2009 Jul;31(3):172-82.
- [29] Itoh A, Ueno E, Tohno E, Kamma H, Takahashi H, Shiina T, Yamakawa M, Matsumura T. Breast disease: clinical application of US elastography for diagnosis. *Radiology*. 2006 May;239(2):341-50.
- [30] Cho N, Moon WK, Kim HY, Chang JM, Park SH, Lyou CY. Sonoelastographic strain index for differentiation of benign and malignant nonpalpable breast masses. *J Ultrasound Med*. 2010 Jan;29(1):1-7.
- [31] Pallwein L, Mitterberger M, Struve P, Pinggera G, Horninger W, Bartsch G, Aigner F, Lorenz A, Pedross F, Frauscher F. Real-time elastography for detecting prostate cancer: preliminary experience. *BJU Int*. 2007 Jul;100(1):42-6
- [32] Lyschchik A, Higashi T, Asato R, Tanaka S, Ito J, Hiraoka M, Insana MF, Brill AB, Saga T, Togashi K. Cervical lymph node metastases: diagnosis at sonoelastography--initial experience. *Radiology*. 2007 Apr;243(1):258-67.

- [33] Wang S, Li J, Manapuram RK, Menodiado FM, Ingram DR, Twa MD, Lazar AJ, Lev DC, Pollock RE, Larin KV. Noncontact measurement of elasticity for the detection of soft-tissue tumors using phase-sensitive optical coherence tomography combined with a focused air-puff system. *Opt Lett*. 2012 Dec 15;37(24):5184-6.
- [34] Ahmad A, Huang PC, Sobh NA, Pande P, Kim J, Boppart SA. Mechanical contrast in spectroscopic magnetomotive optical coherence elastography. *Phys Med Biol*. 2015 Sep 7;60(17):6655-68
- [35] Liang X, Boppart SA. Biomechanical properties of in vivo human skin from dynamic optical coherence elastography. *IEEE Trans Biomed Eng*. 2010 Apr;57(4):953-9.
- [36] Greenleaf JF, Fatemi M, Insana M. Selected methods for imaging elastic properties of biological tissues. *Annu Rev Biomed Eng*. 2003;5:57-78.
- [37] Paszek MJ, Zahir N, Johnson KR, Lakins JN, Rozenberg GI, Gefen A, Reinhart-King CA, Margulies SS, Dembo M, Boettiger D, Hammer DA, Weaver VM. Tensional homeostasis and the malignant phenotype. *Cancer Cell*. 2005 Sep;8(3):241-54.
- [38] Insana MF, Bamber JC. Editorial: Tissue motion and elasticity imaging. *Phys Med Biol*. 2000 Jun;45(6):2.
- [39] Butcher DT, Alliston T, Weaver VM. A tense situation: forcing tumour progression. *Nat Rev Cancer*. 2009 Feb;9(2):108-22.
- [40] Fatemi M, Wold LE, Alizad A, Greenleaf JF. Vibro-acoustic tissue mammography. *IEEE Trans Med Imaging*. 2002 Jan;21(1):1-8.
- [41] Alizad A, Fatemi M, Whaley DH, Greenleaf JF. Application of vibro-acoustography for detection of calcified arteries in breast tissue. *J Ultrasound Med*. 2004 Feb;23(2):267-73.
- [42] Qiu Y, Sridhar M, Tsou JK, Lindfors KK, Insana MF. Ultrasonic viscoelasticity imaging of nonpalpable breast tumors: preliminary results. *Acad Radiol*. 2008 Dec;15(12):1526-33.
- [43] Tanter M, Bercoff J, Athanasiou A, Deffieux T, Gennisson JL, Montaldo G, Muller M, Tardivon A, Fink M. Quantitative assessment of breast lesion viscoelasticity: initial clinical results using supersonic shear imaging. *Ultrasound Med Biol*. 2008 Sep;34(9):1373-86.
- [44] Sandrin L, Fourquet B, Hasquenoph JM, Yon S, Fournier C, Mal F, Christidis C, Ziol M, Poulet B, Kazemi F, Beaugrand M, Palau R. Transient Elastography: A new noninvasive method for assessment of hepatic fibrosis. *Ultrasound Med Biol*. 2003 Dec;29(12):1705-13.
- [45] Huwart L, Peeters F, Sinkus R, Annet L, Salameh N, ter Beek LC, Horsmans Y, Van Beers BE. Liver Fibrosis: Non-invasive assessment with MR elastography. *NMR Biomed*. 2006 Apr;19(2):173-9.
- [46] Bavu E, Gennisson JL, Couade M, Bercoff J, Mallet V, Fink M, Badel A, Vallet-Pichard A, Nalpas B, Tanter M, Pol S. Noninvasive in vivo liver fibrosis evaluation using supersonic shear imaging: a clinical study on 113 hepatitis C virus patients. *Ultrasound Med Biol*. 2011 Sep;37(9):1361-73.
- [47] Bhatia KS, Tong CS, Cho CC, Yuen EH, Lee YY, Ahuja AT. Shear wave elastography of thyroid nodules in routine clinical practice: preliminary observations and utility for detecting malignancy. *Eur Radiol*. 2012 Nov;22(11):2397-406.

- [48] Chan R, Chau A, Karl W, Nadkarni S, Khalil A, Iftimia N, Shishkov M, Tearney G, Kaazempur-Mofrad M, Bouma B. Oct-based arterial elastography: robust estimation exploiting tissue biomechanics. *Opt Express*. 2004 Sep 20;12(19):4558-72.
- [49] Nightingale K, McAleavey S, Trahey G. Shear-wave generation using acoustic radiation force: in vivo and ex vivo results. *Ultrasound Med Biol*. 2003 Dec;29(12):1715-23.
- [50] Chakouch MK, Charleux F, Bensamoun SF. Quantifying the elastic property of nine thigh muscles using magnetic resonance elastography. *PLoS One*. 2015 Sep 23;10(9): e0138873.
- [51] Park SW, Schapery RA. Methods of interconversion between linear viscoelastic material functions. Part I—A numerical method based on Prony series. *Int J Solids Struct*. 1999 April;36(11):1653-1675.
- [52] Murata H, Shigeto N, Hamada T. Viscoelastic properties of tissue conditioners—stress relaxation test using Maxwell model analogy. *J Oral Rehabil*. 1990 Jul;17(4):365-75.
- [53] Sedef M, Samur E, Basdogan C. Real-time finite-element simulation of linear viscoelastic tissue behavior based on experimental data. *IEEE Comput Graph Appl*. 2006 Nov-Dec;26(6):58-68.
- [54] Jagota A, Argento C, Mazur S. Growth of adhesive contacts for Maxwell viscoelastic spheres. *J. Appl. Phys*. 1998 Jan;83(1):250-259.
- [55] Clayton EH, Garbow JR, Bayly PV. Frequency-dependent viscoelastic parameters of mouse brain tissue estimated by MR elastography. *Phys Med Biol*. 2011 Apr 21;56(8):2391-406.
- [56] Caputo M, Carcione JM, Cavallini F. Wave simulation in biologic media based on the Kelvin–Voigt fractional-derivative stress–strain relation. *Ultrasound Med Biol*. 2011 Jun;37(6):996-1004.
- [57] Kiss MZ, Varghese T, Hall TJ. Viscoelastic characterization of in vitro canine tissue. *Phys Med Biol*. 2004 Sep 21;49(18):4207-18.
- [58] Teodorovich EV. Sliding of a cylinder on a viscoelastic foundation. *J. Appl. Math. Mech*. 1978 Dec; 42 (2), 384–389.
- [59] Golden JM. The problem of a moving rigid punch on an unlubricated visco elastic half-plane. *Q J Mechanics Appl Math*. 1979;32 (1): 25-52.
- [60] Zhu Y, Chen X, Zhang X, Chen S, Shen Y, Song L Modeling the mechanical properties of liver fibrosis in rats. *J Biomech*. 2016 Mar 16. 90(16)30296-2.
- [61] Flugge W. *Viscoelasticity*. Blaisdell Publishing Company , Massachusetts. 1967.
- [62] Christensen RM. *Theory of Viscoelasticity: An Introduction*. Academic Press. 1982.
- [63] Pipkin A. *Lectures on viscoelasticity theory*. Applied Mathematical Sciences. Springer-Verlag. 1972
- [64] Sloninsky GL. Laws of mechanical relaxation processes in polymers. *J Polym Sci, Part C*.1967;16:1667–1672.
- [65] Sridhar M, Liu J, Insana MF. Elasticity imaging of polymeric media. *J Biomech Eng*. 2007 Apr;129(2):259-72.
- [66] Weis A. *The Macromolecular Chemistry of Gelatin*. Academic Press, New York, 1964.

- [67] Orescanin M, Toohey K, Insana MF. Material properties from acoustic radiation force step response. *J Acoust Soc Am*. 2009; 125:2928-2936.
- [68] Khaldoun N Altahhan, Yue Wang, Nahil Sobh, Michael F Insana. Indentation Measurements to validate dynamic elasticity imaging methods. *Ultrason Imaging*. 2015 Sep 16.
- [69] Nitta N, Shiina T, Ueno E. Hysteresis parameter imaging of soft tissue under quasi-static deformation. *Ultrasonics*, 2003 IEEE Sympos. 2003 Oct; 2:1606 – 1609.
- [70] VanLandingham MR. Review of instrumented indentation. *J. Res. Natl. Inst. Stand. Technol*. 2003 Aug;108:249-265.
- [71] Palacio-Torralba J, Hammer S, Good DW, McNeill SA, Stewart GD, Reuben RL, Chen Y. Quantitative diagnostics of soft tissue through viscoelastic characterization using time-based instrumented palpation. *J Mech Behav Biomed Mater*. 2015 Jan;41:149-60.
- [72] Lee S, Knauss WG. A note on the determination of relaxation and creep data from ramp tests. *Mechanics of Time-Dependent Materials*. 2002 Mar;4(1), 1-7.
- [73] Abramowitch SD, Woo SL-Y. An improved method to analyze the stress relaxation of ligaments following a finite ramp time based on the quasi-linear viscoelastic theory. *J Biomech Eng*. 2004 Feb;126(1):92-7.
- [74] Mattice JM, Lau AG, Oyen ML, Kent RW. Spherical indentation load-relaxation of soft biological tissues. *J. Mater. Res*. 2011 Mar;21(08):2003-2010.
- [75] Tzikang C. Determining a Prony series for a viscoelastic material from time varying strain data. 2000
- [76] Sinkus R, Tanter M, Catheline S, Lorenzen J, Kuhl C, Sondermann E, Fink M. Imaging Anisotropic and Viscous Properties of Breast Tissue by Magnetic Resonance Elastography. *Magn Reson Med*. 2005 Feb;53(2):372-87.
- [77] Zhang J, and Muthupillai R. Magnetic Resonance Elastography. In: *Handbook of Imaging in Biological Mechanics*, Neu C and Genin G, Eds., CRC Press 2014.
- [78] Van EE, Paulsen KD, Miga MI, Kennedy FE, Weaver JB. An Overlapping Subzone Technique for MR-Based Elastic Property Reconstruction. *Magn Reson Med*. 1999 Oct;42(4):779-86.
- [79] Van EE, Weaver JB, Miga MI, Kennedy FE, Paulsen KD. Elasticity Reconstruction from Experimental MR Displacement Data: Initial Experience with an Overlapping Subzone Finite Element Inversion Process. *Med Phys*. 2000 Jan;27(1):101-7.
- [80] DeWall RJ, T Varghese, Madsen EL. Shear Wave Velocity Imaging Using Transient Electrode Perturbation: Phantom and Ex Vivo Validation. *IEEE Trans Med Imaging*. 2011 Mar;30(3):666-78.
- [81] Orescanin M, and Insana MF. Shear Modulus Estimation with Vibrating Needle Stimulation. *IEEE Trans Ultrason Ferroelectr Freq Control*. 2010 Jun;57(6):1358-67.
- [82] Li C, Guan C, Cheng X, Huang Z, and Wang R. Quantitative Elastography Provided by Surface Acoustic Waves Measured by Phase-Sensitive Optical Coherence Tomography. *Opt Lett*. 2012 Feb 15;37(4):722-4.
- [83] Nightingale KR., Palmeri ML, Nightingale RW, and Trahey GE. On the Feasibility of Remote Palpation Using Acoustic Radiation Force. *J Acoust Soc Am*. 2001 Jul;110(1):625-34.

- [84] Bernal M, Nenadic I, Urban MW, Greenleaf JF. Material property estimation for tubes and arteries using ultrasound radiation force and analysis of propagating modes. *J Acoust Soc Am*. 2011 Mar;129(3):1344-54.
- [85] Yoshitaka Odagiri, Hideyuki Hasegawa and Hiroshi Kanai. Ultrasonic Measurement of Strain Distribution Inside Object Cyclically Compressed by Dual Acoustic Radiation Force. *Jpn. J. Appl. Phys.* 2008;47:4193.
- [86] Telford WM, Geldart LP, Robert ES. *Applied Geophysics* Cambridge University Press. 1990:149.
- [87] Zhang X, Greenleaf JF. Estimation of Tissue's Elasticity with Surface Wave Speed. *J Acoust Soc Am*. 2007;122(5):2522-2525.
- [88] Kirkpatrick SJ, Wang R, and Duncan DD. OCT-Based Elastography for Large and Small Deformations. *Opt Express*. 2006 Nov 27;14(24):11585-97.
- [89] Bourse G, Myotte P, Xu WJ, Lanceleur P. Evaluation of Elastic Properties of Surface Layer from Rayleigh Wave Dispersion. *Review of Progress in Quantitative Nondestructive Evaluation*. 1999;(18): 1439-1445.
- [90] Li C, Guan G, Reif R, Huang Z, Wang RK. Determining Elastic Properties of Skin by Measuring Surface Waves from an Impulse Mechanical Stimulus using Phase-Sensitive Optical Coherence Tomography. *J R Soc Interface* 2012; 9(70):831-841.
- [91] Wang Y, Adie SG, Boppart SA, Insana MF. Ultrasound and Optical Methods for Dynamic Viscoelastic Imaging. In *Handbook of Imaging in Biological Mechanics*, Neu C and Genin G, Eds., CRC Press. 2014; 81-94 .
- [92] Wang Y, Insana MF. Viscoelastic Properties of Rodent Mammary Tumors Using Ultrasonic Shear-Wave Imaging. *Ultrason Imaging*. 2013 Apr;35(2):126-45.
- [93] Manduca A, Lake DS, Kruse SA, Ehman RL. Spatio-Temporal Directional Filtering for Improved Inversion of MR Elastography Images. *Med Image Anal*. 2003 Dec;7(4):465-73.
- [94] Schmitt C, Hadj Henni A, Cloutier G. Characterization of Blood Clot Viscoelasticity by Dynamic Ultrasound Elastography and Modeling of the Rheological Behavior. *J Biomech*. 2011 Feb 24;44(4):622-9.
- [95] Pritz T. Five-Parameter Fractional Derivative Model for Polymeric Damping Materials. *J Sound Vibration*. 2003;265(5):935-952.
- [96] Magin RL. *Fractional Calculus in Bioengineering*. Begell House, CT. 2006.
- [97] Sinkus R, Siegmann K, Xydeas T, Tanter M, Claussen C, Fink M. MR Elastography of Breast Lesions: Understanding the Solid/Liquid Duality Can Improve the Specificity of Contrast-Enhanced MR Mammography. *Mag Res Med*. 2007;58:1135-1144.
- [98] Orescanin M, Wang Y, Insana MF. 3-D Fdtd Simulation of Shear Waves for Evaluation of Complex Modulus Imaging. *IEEE Trans Ultrason Ferroelectr Freq Control*. 2011 Feb;58(2):389-98.
- [99] Schedin P, Keely PJ. Mammary gland ECM remodeling, stiffness, and mechanosignaling in normal development and tumor progression. *Cold Spring Harb Perspect Biol*. 2011 Jan;3(1):a003228.

- [100] Falzon G, Pearson S, Murison R. Analysis of collagen fibre shape changes in breast cancer. *Phys Med Biol*. 2008 Dec 7;53(23):6641-52.
- [101] Samuel CS. Determination of collagen content, concentration, and sub-types in kidney tissue. *Methods Mol Biol*. 2009;466:223-35.
- [102] Cheng W, Yan-Hua R, Fang-Gang N, Guo-An Z. The content and ratio of type I and III collagen in skin differ with age and injury. *African Journal of Biotechnology*. 2011;10(13):2524-2529.
- [103] Okano F. Study on stromal component of mastopathy—content and type of collagen. *Hokkaido Igaku Zasshi*. 1985 Jul;60(4):555-70.
- [104] Cechowska-Pasko M, Palka J, Wojtukiewicz MZ. Enhanced prolidase activity and decreased collagen content in breast cancer tissue. *Int J Exp Pathol*. 2006 Aug;87(4):289-96.
- [105] Duncan DD, Kirkpatrick SJ, Mark FF, Hunter LW. Transform Method of Processing for Speckle Strain-Rate Measurements. *Appl Opt*. 1994 Aug 1;33(22):5177-86.
- [106] Kirkpatrick SJ, Brooks BW. Micromechanical Behavior of Cortical Bone as Inferred from Laser Speckle Data. *J Biomed Mater Res*. 1998 Mar 5;39(3):373-9.
- [107] Chiang FP. Micro-/Nano-Speckle Method with Applications to Materials, Tissue Engineering and Heart Mechanics. *Strain*. 2008 Jan; 44(1):27-39.
- [108] Li S, Mohan KD, Sanders WW, Oldenburg AL. Toward Soft-Tissue Elastography Using Digital Holography to Monitor Surface Acoustic Waves. *J Biomed Opt*. 2011 Nov;16(11):116005.
- [109] Mohan KD, Oldenburg AL. Elastography of Soft Materials and Tissues by Holographic Imaging of Surface Acoustic Waves. *Opt Express*. 2012 Aug 13;20(17):18887-97.
- [110] Nightingale K. Acoustic Radiation Force Impulse (Arfi) Imaging: A Review. *Curr Med Imaging Rev*. 2011 Nov 1;7(4):328-339.
- [111] Zhang X, Greenleaf JF. Estimation of tissue's elasticity with surface wave speed. *J Acoust Soc Am*. 2007 Nov;122(5):2522-5.
- [112] Fishbein KW, Gluzband YA, Kaku M, Ambia-Sobhan H, Shapses SA, Yamauchi M, Spencer RG, Effects of formalin fixation and collagen cross-linking on T2 and magnetization transfer in bovine nasal cartilage. *Magn Reson Med*. 2007 Jun;57(6):1000-11.
- [113] Bouchard RR, Hsu SJ, Wolf PD, Trahey GE. In vivo cardiac, acoustic-radiation-force-driven, shear wave velocimetry. *Ultrason Imaging*. 2009 Jul;31(3):201-13.
- [114] Nenadic IZ, Urban MW, Aristizabal S, Mitchell SA, Humphrey TC, Greenleaf JF. On Lamb and Rayleigh wave convergence in viscoelastic tissues. *Phys Med Biol*. 2011 Oct 21;56(20):6723-38.
- [115] Zhang X, Qiang B, Greenleaf J. Comparison of the surface wave method and the indentation method for measuring the elasticity of gelatin phantoms of different concentrations. *Ultrasonics*. 2011 Feb;51(2):157-64.
- [116] Qiang B, Greenleaf JF, Oyen ML, Zhang X. Estimating material elasticity by spherical indentation load relaxation test on viscoelastic sample of finite thickness. *IEEE Trans Ultrason Ferroelectr Freq Control*. 2011 Jul;58(7):1418-29.

- [117] Oyen ML. Nanoindentation of biological and biomimetic materials. *Experimental Techniques*. 2011; 37:73–87.
- [118] Dimitriadis EK, Horkay F, Maresca J, Kachar B, Chadwick RS. Determination of elastic moduli of thin layers of soft materials using atomic force microscope. *Biophys J*. 2002; 82:2798-2810.
- [119] Orescanin M, Muqem AQ, Kathleen ST, Insana MF. Dispersion and Shear Modulus Measurements of Porcine Liver. *Ultrason Imaging*. 2010 Oct;32(4):255-66.
- [120] Manduca A, Lake DS, Kruse SA, Ehman RL. Spatio-temporal directional filtering for improved inversion of MR elastography images. *Med Image Anal*. 2003; 7:465–473.
- [121] Nenadic IZ, Urban MW, Mitchell SA, Greenleaf JF. Lamb Wave Dispersion Ultrasound Vibrometry (LDUV) Method for Quantifying Mechanical Properties of Viscoelastic Solids. *Phys Med Biol*. 2011 Apr 7;56(7):2245-64.
- [122] Bernal M, Gennisson JL, Flaud P, Tanter M. Correlation between Classical Rheometry and Supersonic Shear Wave Imaging in Blood Clots. *Ultrasound Med Biol*. 2013 Nov;39(11):2123-36.
- [123] Friedrich Ch, Sehiessel H, Blumen A. Constitutive behavior modeling and fractional derivatives. *Rheology Series*. 1999:429-466.
- [124] Koeller, R. C. Applications of fractional calculus to the theory of viscoelasticity. *J. Appl. Mech*. 1984;51(2):299-307.
- [125] Papoulia KD, Panoskaltsis VP, Kurup NV, Korovajchuk I. Rheological representation of fractional order viscoelastic material models. *Rheologica Acta*. 2010;49(4):381-400.
- [126] Sasso M, Palmieri G, Amodio D. Application of fractional derivative models in linear viscoelastic problems. *Mechanics of Time-Dependent Materials*. 2011 Sep;15(4):367-387.
- [127] Taylor LS, Lerner AL, Rubens DJ, Parker KJ. A Kelvin-Voigt fractional derivative model for viscoelastic characterization of liver tissue. 2002 Jan; ASME International Mechanical Engineering Congress and Exposition, 447-448.
- [128] Zhuravkov MA, Romanova NS. Review of methods and approaches for mechanical problem solutions based on fractional calculus. *Math Mech Solids*, 2014 May.
- [129] Di Paola M, Pirrotta A, Valenza A. Visco-elastic behavior through fractional calculus: an easier method for best fitting experimental results. *Mech Mater*. 2011 Dec;43(12):799-806.
- [130] Meral FC, Royston TJ, Magin R. Fractional calculus in viscoelasticity: an experimental study. *Commun Nonlinear Sci Numer Simul*. 2010 Apr;15(4):939-945.
- [131] Magin RL. Fractional calculus in bioengineering: A tool to model complex dynamics. In *Carpathian Control Conference (ICCC), 2012 13th International* (pp. 464-469). IEEE.
- [132] wJ Welch S, Rorrer RA, Duren Jr RG. Application of time-based fractional calculus methods to viscoelastic creep and stress relaxation of materials. *Mech. Time-Depend. Mater*. 1999;3(3): 279-303.
- [133] Podlubny I. *Fractional Differential Equations: An introduction to fractional derivatives, fractional differential equations, to methods of their solution and some of their applications* (Vol. 198). Academic Press. 1998

- [134] Zhang H, Wang Y, Insana MF. Ramp-hold relaxation solutions for the KVFD model applied to soft viscoelastic media. *Meas Sci Technol*. 2016 Jan;27:025702.
- [135] Cai S, Hu Y, Zhao X, Suo Z. Poroelasticity of a covalently crosslinked alginate hydrogel under compression. *J. Appl. Phys.* 2010 Dec;108(11):113514.
- [136] Oyen ML. Spherical indentation creep following ramp loading. *J. Mater. Res.* 2005 Aug; 20(08): 2094-2100.
- [137] Zhang HM, Wang Y, Fatemi M, Insana M. Assessing composition and structure of soft biphasic media from Kelvin-Voigt fractional derivative model parameters. *Soft Matter*. (In preparation)
- [138] Kalyanam S, Yapp RD, Insana MF. Poro-viscoelastic behavior of gelatin hydrogels under compression-implications for bioelasticity imaging. *J Biomech Eng.* 2009 Aug;131(8):081005.
- [139] Chatterjee A. Statistical origins of fractional derivatives in viscoelasticity. *J. Sound Vibrat.* 2005 Jun; 284(3):1239–1245.
- [140] Pfitzenreiter T. A physical basis for fractional derivatives in constitutive equations. *Z. Angew. Math. Mech.* 2004 Feb; 84(4):284–287.
- [141] Coussot C, Kalyanam S, Yapp RD, Insana MF. Fractional derivative models for ultrasonic characterization of polymer and breast tissue viscoelasticity. *IEEE Trans Ultrason Ferroelectr Freq Control.* 2009 Apr;56(4):715-26.
- [142] Torvik PJ, Bagley RL, On the appearance of the fractional derivative in the behavior of real materials. *J. Appl. Mech.* 1984 Jun; 51(2):294-298.
- [143] Sack I, Jöhrens K, Würfel J, Braun J. Structure-sensitive elastography: on the viscoelastic powerlaw behavior of in vivo human tissue in health and disease. *Soft Matter*, 2013 May;9(24):5672-5680.
- [144] Varghese T, Techavipoo U, Liu W, Zagzebski JA, Chen Q, Frank G, Lee Jr FT. Elastographic measurement of the area and volume of thermal lesions resulting from radiofrequency ablation: pathologic correlation. *AJR Am J Roentgenol.* 2003 Sep;181(3):701-7.
- [145] Orescanin M, Muqem AQ, Kathleen ST, Insana MF. Dispersion and Shear Modulus Measurements of Porcine Liver. *Ultrason Imaging.* 2010 Oct;32(4):255-66.
- [146] Sapin-de Brosses E, Gennisson JL, Pernot M, Fink M, Tanter M. Temperature dependence of the shear modulus of soft tissues assessed by ultrasound. *Phys Med Biol.* 2010 Mar 21;55(6):1701-18.
- [147] Benech N, Negreira CA. Monitoring heat-induced changes in soft tissues with 1-D transient elastography. *Phys Med Biol.* 2010 Mar 21;55(6):1753-65.
- [148] Gross J. Organization and disorganization of collagen. *Biophys. J.* 1964;4:Suppl 83-77.
- [149] Kang TW, Rhim H. Recent advances in tumor ablation for hepatocellular carcinoma. *Liver Cancer.* 2015 Sep;4(3):176-87.
- [150] Chu KF, Dupuy DE. Thermal ablation of tumours: biological mechanisms and advances in therapy. *Nat Rev Cancer.* 2014 Mar;14(3):199-208.
- [151] Rossikhin YA, Shitikova MV. A new method for solving dynamic problems of fractional derivative viscoelasticity. *INT J ENG SCI.* 2001 Jan;39(2):149–176.

[152] Hoyt K, Castaneda B, Zhang M, Nigwekar P, di Sant'agnese PA, Joseph JV, Strang J, Rubens DJ, Parker KJ. Tissue elasticity properties as biomarkers for prostate cancer. *Cancer Biomark*. 2008;4(4-5):213-25.

[153] Zhang M, Nigwekar P, Castaneda B, Hoyt K, Joseph JV, di Sant'Agnese A, Messing EM, Strang JG, Rubens DJ, Parker KJ. Quantitative characterization of viscoelastic properties of human prostate correlated with histology. *Ultrasound Med Biol*. 2008 Jul;34(7):1033-42.